8-2016

Efficient modeling of sound source radiation in free-space and room environments

Yangfan Liu
Purdue University

Graduate School Form
30 Updated 12/26/2015

PURDUE UNIVERSITY
GRADUATE SCHOOL
Thesis/Dissertation Acceptance

This is to certify that the thesis/dissertation prepared

By Yangfan Liu

Entitled
Efficeint Modeling of Sound Source Radiation in Free-Space and Room Environments

For the degree of Doctor of Philosophy

Is approved by the final examining committee:

J. Stuart Bolton
Co-chair

Patricia Davies
Co-chair

Kai Ming Li

Mark R. Bell

To the best of my knowledge and as understood by the student in the Thesis/Dissertation Agreement, Publication Delay, and Certification Disclaimer (Graduate School Form 32), this thesis/dissertation adheres to the provisions of Purdue University's "Policy of Integrity in Research" and the use of copyright material.

Approved by Major Professor(s): J. Stuart Bolton

Approved by: Jay P. Gore 7/22/2016

Head of the Departmental Graduate Program Date

EFFICIENT MODELING OF SOUND SOURCE RADIATION IN FREE-SPACE AND ROOM ENVIRONMENTS

A Dissertation

Submitted to the Faculty

of

Purdue University

by

Yangfan Liu

In Partial Fulfillment of the

Requirements for the Degree

of

Doctor of Philosophy

August 2016

Purdue University

West Lafayette, Indiana

TABLE OF CONTENTS

Page

Page

LIST OF TABLES

LIST OF FIGURES

Figure Page

Figure Page

Figure Page

Figure Page

ABSTRACT

Liu, Yangfan. Ph.D., Purdue University, August 2016. Efficient Modeling of Sound Source Radiation in Free-Space and Room Environments. Major Professor: J. Stuart Bolton, School of Mechanical Engineering.

Motivated by the need to develop efficient acoustics simulations for sources in different room environments, a modeling procedure has been proposed that consists of two steps in general: (1) the modeling of the free-space radiation of the source based on measurements in a anechoic environment, and (2) the prediction of the sound field in a room environment based on that free-space information.

To achieve a high modeling efficiency, i.e., to reduce the number of modeling parameters while still maintaining acceptable accuracy, a Multipole Equivalent Source Model (ESM) with undetermined source locations has been developed for the free-space sound field prediction. In contrast with traditional ESM's, or acoustical holography methods in general, the model developed in the present work possesses two efficiency improvements: (1) the use of the series of monopoles, dipoles, quadrupoles, etc. as equivalents sources (since in predicting the sound field, the multipole series can be simply represented as closely located monopoles) and (2) the flexibility of using spatially separated sources with undetermined locations. In the inverse parameter estimation process of this method, the calculation of the source strengths is linear while the source locations are determined

by a nonlinear optimization procedure. It is shown, by an experimental validation, that the prediction using this method can be accurate for almost the whole audio frequency range

To model the sound field at high frequencies specifically, different types of methods using local-basis functions were developed. At high frequencies, the spatial variation of the sound field is usually large and thus the number of measurements points in space is likely not to be enough to model a relatively complicated source if a traditional equivalent source model is used, and the under-sampling errors from all regions will accumulate to affect the predictions in any particular region. However, if localized basis functions are used to represent the sound field, the under-sampling errors from different regions do not affect each other. Two types of local-basis method are developed in this work: one based on piece-wise polynomial interpolation (which is limited to having only a single source) and the other based on least squares (which can be applied to multiple sources and even to interior problems). Simulation results have shown that these local-basis methods, at very high frequencies, can achieve good overall prediction accuracy with only a loss of some details in the spatial variation of the sound field.

In the room acoustics modeling section, the Equivalent Source Method is modified and implemented which, compared with the geometric acoustics models, gives a prediction based on a more rigorous mathematical foundation and, compared with Boundary Element methods, reduces the computational intensity. In this proposed room acoustics ESM, the free-space source radiation is assumed known, and the room component sound field is determined by an ESM. Differing from the free-space ESMs, this room acoustics ESM (1)

contains additional equivalent sources representing the incoming waves, and (2) uses impedance boundary conditions on the surfaces instead of the measured sound field, to estimate the source strengths. It is validated by simulations (in both 2D and 3D spaces) and then by experiments that the proposed room acoustics ESM can be used as a reduced order modeling technique in simulating the sound field in a room. It is also shown that the prediction accuracy and the computational load can be flexibly balanced, if Multipole ESMs are used, by selecting an appropriate maximum source order.

CHAPTER 1. INTRODUCTION

1.1 Motivation and Objective

Efficient simulations of sound field in different environment are of great application potential and research interests. The prediction of free-space sound fields, for example, can be a useful tool to characterize and visualize the acoustic radiation of certain machines or audio devices; it is also helpful from a noise control point-of-view, to identify the locations and the strengths of noise sources from each component of a machine. Sound field simulations in room acoustics, i.e., predicting the sound field in a room, are widely applied in the design of concert halls, and in-car audio systems, etc. Although each application and technique can give its own practical value and research interest, the primary motivation behind the work presented here is the desire of having a fast simulation technique to accurately predict the sound radiations of sources, such as loudspeakers, televisions or other audio systems, in free space and in different room environments, so that the design of the audio products and the listening environments can be easily and effectively evaluated.

The problem addressed in this work can be described as: to predict the sound field everywhere in free space and inside a certain room based on: (1) the measurements of the free-space sound pressure at a number of locations (or the distribution of the normal

velocities on the source surface) and (2) the boundary conditions on all the source and room surfaces, usually the distribution of the normal impedances. Computationally intensive techniques such as the Finite Element Models and Boundary Element Models are not convenient to use, especially when the frequency is high and the room is large, because a large number of elements are required in these numerical techniques, resulting in a very intensive computation load. Therefore the modeling approaches proposed in the work reported here are mainly extensions and improvements of techniques in the category of acoustic holography which, traditionally, aim at sound field reconstruction from sound pressure measurements in an anechoic environment (usually only accurate at low frequencies). Specifically, the current work is an attempt to improve the traditional holography techniques in the aspects of reducing the modeling order, extending the feasible frequency range and generalizing their applications to deal with room acoustics simulations. It is also pointed out here that since there is no solution, strictly speaking, to achieving high speed and accuracy at the same time, the claim of fast and accurate simulation here essentially means finding an appropriate balance between prediction accuracy and the computational intensity.

1.2 The General Modeling Procedure

Based on the above mentioned application that required efficient and accurate predictions of the sound field generated by certain sources in free space and in different room environments, a modeling procedure was proposed (illustrated in Figure 1.1) which, in general, contains two steps: (1) the reconstruction of the sound field in free space from the measured sound field at a number of locations (the same as in traditional acoustic

holography techniques) and (2) the prediction of the sound field in different rooms with the input of the free-space sound field and the surface impedances of the rooms. The main reasons for using two separate steps are firstly, that when the sound field of the same source in several room environments is to be simulated, it is not necessary to perform measurements in each room; and, secondly, that the free space sound radiation from the source itself is of interest, from the design of audio products point-of-view, because it can provide information about how certain features in the design affect the acoustic radiation pattern. Also, the modeling procedure is more efficient than a single-step room acoustics simulation procedure, i.e., requires fewer model parameters to describe the target sound field, if the modeling orders are reduced for both the free-space and room acoustics simulations, because the room acoustics simulation requires the calculation of the free-space sound field from the source as an input.

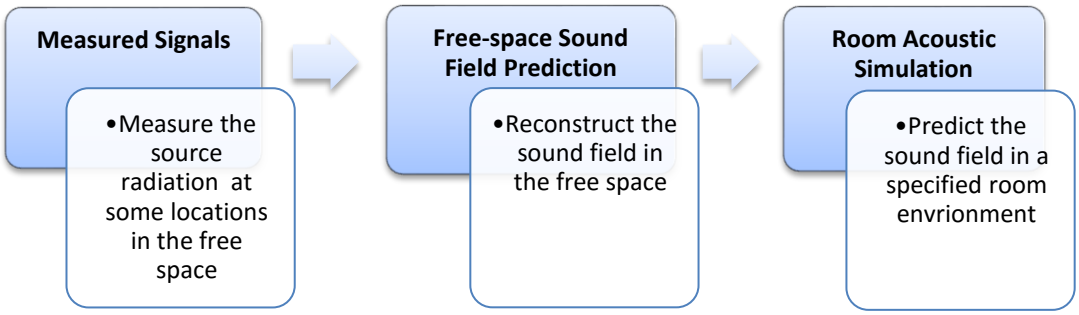

Figure 1.1. Illustration of the proposed two-step simulation approach.

1.3 Outline of this Document

It has already been mentioned that the current work focuses on improving the techniques used in acoustic holography to achieve lower model orders and improved accuracy for

higher frequencies and extending their use to room acoustics simulations. In Chapter 2, the background and techniques that are commonly used in free-space and room acoustics sound field simulations are summarized. Limitations of these techniques will be mentioned and the reasons why they are not desirable, when used directly, in the application of the present work, will be briefly explained. Among the techniques reviewed in that chapter, the Equivalent Source Model (ESM) has the strongest connection to this work; in that method it is assumed that the sound field to be reconstructed can be described as a combination of contributions from a number of sources of certain types (equivalent sources) and then the strength of each source is estimated by matching the model predictions with the measurements. With the calculated source strength, the sound field can be calculated everywhere. All the techniques developed in this work are, to some extent, improvements and modifications of the traditional Equivalent Source Method.

In Chapter 3, a free-space sound field prediction method, proposed in this work and referred to as the Equivalent Source Method with un-fixed source locations, will be explained in detail. This method has been shown to provide accurate predictions over a larger frequency range than traditional techniques. In this approach, differing from traditional ESMs, the series of monopoles, dipoles, quadrupoles, etc. are used as the equivalent sources and the locations of the sources, in addition to the source strengths, are assumed unknown and are estimated based on the measurements. It is this additional flexibility of undetermined source locations that gives a higher frequency limit and reduces the number of model parameters needed for accurate sound field predictions. It is also mentioned that by using this method, it is more convenient for the construction of the room

acoustics models, since each equivalent source can be represented as a number of closely located monopoles, it is possible to only consider monopole inputs in the room acoustics models if it can be assumed that the scattered sound field from the source geometry is small compared with that reflected from the room.

In Chapter 4, it is explained how the use of Equivalent Source Methods can be extended in the room acoustics applications. This extension is desirable because it can provide an alternative that is faster compared with the Boundary Element Models and has a more rigorous mathematical foundation compared with the geometric acoustics models. Compared with the usual Equivalent Source Models, the room acoustics ESM contains additional sources representing the incoming wave contributed by the room surfaces. To avoid the need of making measurements in the room, the impedance boundary conditions on all the surfaces (rather than measured sound pressure as in traditional ESMs) are used to estimate the parameters. It is also demonstrated that this proposed approach, when multipoles are chosen as equivalent sources, can offer a flexible balance between the model's prediction accuracy and its computational intensity.

The method developed in Chapter 3 can give accurate performance at higher frequencies than traditional acoustic holography methods; however, it is not designed for very high frequencies for relatively complicated sources, since the sound field can be very complicated at high frequencies and the number of measurements is usually less than what is required to describe all the details in the spatial variations of the sound field. A treatment, referred to as the local basis Method, is described in Chapter 5 to deal with this situation,

which can be used to predict the general pattern of the sound field, with the loss of some details in spatial variations. This result has an advantage compared with traditional sound reconstruction methods in which largely meaningless results will be obtained at very high frequencies. The main reason for this improvement is that the function basis, can also be interpreted as equivalent sources, that are used to describe to sound field and which only contribute to a particular region in space so that the spatial under-sampling errors from other regions will not affect the estimation of the model parameters. In this way, the accumulation of errors from the whole space (as in the cases of using traditional approaches) is avoided. An additional advantage can be brought out by the local basis method: when measurement information is given only in certain solid angle region rather than covering the whole source, good predictions can still be achieved in that region and are not affected by the missing information in other regions.

In Chapter 6, the work presented in this document is summarized, the main results and conclusions are stated and the associated improvements as well as the limits are commented upon. The possible future works are also discussed in that chapter.

CHAPTER 2. A REVIEW OF SOUND FIELD PREDICTION TECHNIQUES FOR DIFFERENT ENVIRONMENTS

2.1 Introduction

The two general steps included in the whole modeling process, as introduced in the previous chapter, are: (1) the prediction of the free-space sound field radiation from a source based on sound field measurements (typically sound pressure measurements) at a number of locations in an anechoic environment; and (2) the simulation of the sound field in a room with given free-space information, room geometry and normal impedance distributions on all the surfaces. It is noted that the results from the first step are taken as the input of the second step. In order to present more clearly the methods developed in the current work (to be discussed in detail in later chapters) dealing with problems in both steps, the commonly used simulation techniques for both the free-space and the room environments are briefly reviewed and explained here in this chapter. The limitations associated with each of these techniques will be commented upon, which can then explain why it is not desirable to use them directly in the application of this work and can also illustrate the aspects on which improvements are necessary.

2.2 A Review of Free-space Sound Field Prediction Techniques

It has been explained in the previous chapter that for the purpose of reducing the computational intensity, the free-space simulation methods used in the current work are

developed based on some improvements and modifications of techniques in the area of acoustical holography. Thus the techniques in acoustical holography are focused on in this section. In general, the goal of acoustical holography is to predict or reconstruct the total sound field in free space based on sound field measurements at a number of locations in a sub-region of the whole space (usually samples of boundary conditions from a mathematical point of view).

Strictly speaking, there is no widely accepted way to categorize the techniques in the acoustical holography area, and terminologies are frequently used in both strict and loose senses when referring to which category a specific technique belongs. In this document, the review of the techniques will be organized according to the categorization that divides all the methods into two types: (1) the non-parametric (Fourier-based) methods and (2) the parametric methods. Although there is no clear cut distinction, the main difference between these two categories is that the non-parametric methods decompose the total sound field into orthogonal basis functions (i.e., Fourier basis under different coordinate systems) and estimate the coefficients of the each basis function by performing an inverse Fourier transform on the measurement surface meaning that the measurement are required to be performed on a plane, a cylindrical surface or a sphere, etc., depending on the choice of coordinate system. The parametric methods, on the other hand, do not have strict requirements on the measurement locations (because no spatial Fourier transforms need to be performed), and describe the sound field by a model containing a number of parameters which can be estimated from the measurements using optimization techniques. Another reason for using this categorization is that the prediction error in non-parametric methods

are usually analyzed from the spatial windowing and aliasing point-of-view, but for parametric methods, error analysis is often done by treating the process as an inverse parameter estimation problem.

In this section, the Fourier-based methods are reviewed first, and several methods in the category of parametric methods are presented, including the Inverse Boundary Element Method, the Equivalent Source Method and the Statistically Optimized Near-field Acoustical Holography (SONAH). Finally, related treatments of the ill-posed nature of inverse problems are introduced, since they play very important roles in the parametric techniques.

2.2.1 The Fourier-Based Methods

Each technique in the category of Fourier-based methods requires a known sound pressure or normal particle velocity distribution on a certain type of surface: an infinite plane for Cartesian coordinates, a cylinder and a sphere for cylindrical and spherical coordinates respectively. By using the Fourier Transform for the targeted coordinate system, the data on the given surface can be used calculate the sound field on any surface in the space that is conformal to the measurement surface, and thus the sound field in the whole space can be calculated.

Although the connections of the sound field on the given surface to that on a conformal surface were originally derived differently for different coordinates (Williams and Maynard, 1982) (Maynard and Williams, 1985), they can all be derived through the general

solutions of the Helmholtz equation and result in final formulae of the same form (Williams, 1999) (Wu, 2008). The sound field at a fixed frequency in a source free region is governed by the Helmholtz equation:

$$\nabla^2 P(\overrightarrow{X},\omega) + k^2 P(\overrightarrow{X},\omega) = 0, \tag{2.1}$$

where $P(\vec{X},\omega)$ is the sound pressure at a single angular, temporal frequency, ω, and $k = \omega/c$ is the wavenumber. The general solutions for this equation can be generated by separation of variables in different coordinate systems (Williams, 1999). When the Sommerfeld radiation boundary condition is satisfied and the time dependence is assumed to be $e^{-j\omega t}$, the general solution in the Cartesian coordinate system can be described by the family of plane waves and can be written as:

$$P(x,y,z) = \frac{1}{4\pi^2}\int_{-\infty}^{+\infty}\int_{-\infty}^{+\infty} P(k_x,k_y)e^{j(k_x x + k_y y + k_z z)}dk_x dk_y, \tag{2.2}$$

with the familiar relation: $k^2 = k_x^2 + k_y^2 + k_z^2$. Likewise, the general solution in cylindrical coordinates can be expressed as cylindrical waves:

$$P(x,y,z) = \sum_{n=-\infty}^{\infty} e^{jn\phi}\frac{1}{2\pi}\int_{-\infty}^{+\infty} A_n(k_z)e^{jk_z z}H_n^{(1)}(k_r r)dk_z \tag{2.3}$$

where $H_n^{(1)}$ is the Hankel function of the first kind, and $k^2 = k_r^2 + k_z^2$. Finally, in spherical coordinate, the general solution can be written as a series of spherical waves:

$$P(r,\theta,\phi)=\sum_{n=0}^{\infty}\sum_{m=-n}^{n}C_{mn}h_n^{(1)}(kr)Y_n^m(\theta,\phi), \tag{2.4}$$

where $h_n^{(1)}$ is the spherical Hankel function of the first kind. It is observed that all these expressions of the general solutions are in the form of inverse Fourier transforms with respect to different coordinate systems: i.e., the Cartesian, polar and spherical Fourier transforms, respectively. Therefore, if the sound pressure on a plane (for Cartesian coordinates), on a cylinder (for cylindrical coordinates) or on a sphere (for spherical coordinates) is given, the coefficients in equations (2.2) to (2.4) can be determined by calculating two-dimensional Fourier transforms associated to the coordinate system. Thus the sound field reconstruction formula for all three types of Fourier-based methods can be expressed as:

$$P(\overrightarrow{X})=\mathcal{F}^{-1}\{\mathcal{F}\{P(\overrightarrow{X}_H)\}G(\overrightarrow{X}_H,\overrightarrow{X})\}, \tag{2.5}$$

where $\vec{X}_H$ denotes locations on the surface with given measurement data, and the propagator has the following expressions for different coordinate systems: $G(\vec{X}_H,\vec{X})=e^{jk_z(z-z_H)}$ for Cartesian coordinates, $G(\vec{X}_H,\vec{X})=H_n^{(1)}(k_r r)/H_n^{(1)}(k_r r_H)$ for cylindrical coordinates and $G(\vec{X}_H,\vec{X})=h_n^{(1)}(kr)/h_n^{(1)}(kr_H)$ for spherical coordinates.

In practice, however, the sampling and windowing errors brought about by finite discrete measurements have to be dealt with (Kwon and Kim, 1995) (Rowell and Oldham, 1995) as well as the error in measurement locations (Bai, 1995). Based on the above mentioned

idea of acoustical holography, many holography methods and improvements have been proposed in the literature with respect to specific issues. For example, Sarkissian (1991) has used a non-Fourier basis for the prediction of radiation power; Loyau et al. (1988) reconstructed sound fields from intensity measurements, Williams et al. (1989), have extended the normal NAH to the application of broadband excitation, etc. Back-propagation, formulated as an inverse problem, and regularization tools have also been well studied (Nelson and Yoon, 2000) (Yoon and Nelson, 2000) (Williams, 2001). Patch holography, dealing with the practical requirements of a large number of simultaneous measurements, has also been proposed and implemented (Lee and Bolton, 2005) (Lee and Bolton, 2006) (Williams, et al., 2003) (Sarkissian, 2005).

2.2.2 The Inverse Boundary Element Method

One disadvantage of the Fourier based method, from the application point of view, is that it requires the measurements to be performed on a surface of a certain geometry. The use of other techniques, such as the Inverse Boundary Element Method (IBEM), can overcome this issue. The usually preferred IBEM, the direct IBEM (Veronesi and Maynard, 1989), developed based on the Helmholtz integral equation (also referred to as Green's formula) (Williams, 1999) is expressed as:

$$cP(\vec{X},\omega)=\int_{\Gamma}(j\omega\rho_0 v_n(\vec{X}_s,\omega)G(\vec{X}_s\mid\vec{X})-P(\vec{X}_s,\omega)\frac{\partial G(\vec{X}_s\mid\vec{X})}{\partial\vec{n}_s})d\vec{X}_s, \tag{2.6}$$

where P is the sound pressure at location $\vec{X}$, G is the free space Green's function, $\vec{X}_s$ denotes a point on the enclosed boundary Γ, and $\vec{n}_s$ is the normal vector of the boundary

surface pointing to the sound field region. The coefficient c is 1 when $\vec{X}$ is in the sound field region, 0 when $\vec{X}$ is outside and equals the solid angle of the boundary when it is on the boundary.

In the above integral, the right hand side of Eq. (2.6), can be numerically evaluated by using a mesh discretization on the boundary surface where the pressure and the normal velocity distribution on the boundary are interpolated by using surface shape functions. Thus the value of the integral evaluated at an arbitrary location, $\vec{X}$, can be expressed as a linear combination of pressure and normal velocities on nodes of the boundary elements in the mesh. When Eq. (2.6) is evaluated at the locations of the nodes, a linear relation between the nodal values of pressure and that of normal velocities can be established as:

$$C\vec{P}_s = A_s\vec{P}_s + B_s\vec{v}_s, \tag{2.7}$$

in which $\vec{P}_s$ and $\vec{v}_s$ are vectors containing the pressure and normal velocity values on the surface nodes; C is a diagonal matrix with the coefficients of the nodal locations. The matrices A_s and B_s are results from discretizing the two parts of the integral in Eq. (2.6) with $\vec{X}$ evaluated at the nodal locations. It is shown, by Eq. (2.7), that the pressure and the normal velocity on the boundary determine each other, so either one determines the sound field in the whole space.

In order to reconstruct the sound field in the whole sound field region, the nodal pressure and normal velocity values need to be calculated from the measured sound pressure at a number of

locations in the space (with no restrictions on where the measurement should be performed in principle). This is done by solving the linear system generated by evaluating Eq. (2.6) at the measurement locations: i.e.,

$$\vec{P}_m = A_m \vec{P}_s + B_m \vec{v}_s, \tag{2.8}$$

where the subscript m here denotes the measurement locations. Since the measurements are performed inside the sound field region, there is no coefficient matrix involved in Eq. (2.8). Given the measured sound pressure, $\vec{P}_m$, the nodal pressure and normal velocities can be solved by combining Eqs. (2.7) and (2.8). In the matrix inversion process, Singular Value Decomposition is usually applied in consideration of its ill-posed nature (Borgiotti, et al., 1990) (Varah, 1973). The singularity of the matrix relating nodal values to measurements can be improved if the locations of measurements are chosen by using the Effective Independence Method (Kim and Ih, 1996). At some of the eigen frequencies for the associated homogeneous Dirichlet problem inside the boundary surface, it has been shown (Copley, 1968) that the solution to Eq. (2.6) is not unique. One popular treatment with regard to this non-uniqueness issue was the Combined Helmholtz Integral Equation Formulation (CHIEF) developed by Schenck, 1968, which involves modifying Eq. (2.7) to not only contain the nodal locations on the mesh but also several points inside the boundary.

For the sound field generated by a thin vibrating structure that does not form a closed surface, the formulation of the Indirect Boundary Element Method (Raveendra, 1998) can be used as an alternative to the usual direct BEM formulation, which replaces the pressure and normal velocity in Eq. (2.6) by the jump of the pressure and normal velocity cross the

vibrating surface. With further boundary conditions of a specified pressure or velocity on the surface the formula becomes the form of a single or a double layer of potential (Filippi, 1977), which can be expressed as:

$$P(\vec{X},\omega) = \int_{\Gamma} \alpha(\vec{Y},\omega) G(\vec{Y} \mid \vec{X}) d\vec{Y} \tag{2.9}$$

and

$$P(\vec{X},\omega) = \int_{\Gamma} \beta(\vec{Y},\omega) \frac{\partial G(\vec{Y} \mid \vec{X})}{\partial \vec{n}} d\vec{Y} \tag{2.10}$$

respectively, where α and β are the potential density (or strength) functions. With measurements of sound pressure at a number of locations, the potential densities can be estimated by inverting the associated formulation in a similar way as in the direct Inverse BEM (Eq. (2.8)). Although the layers of potential formulation can be derived from the indirect BEM formulation for a thin structure, either the single or double layer potential has a completeness property (Filippi, 1977) (Doicu and et al. 2000) which allows either potential to be used to describe any sound field radiated from a closed surface as well (Chen and Schweikert, 1963). In the work of Valdivia and Williams (2004), the performance of different formulations in the application of acoustical holography were compared and the use of different shape functions was investigated along with the treatments of the ill-posedness in the inversion of the formulation. Both the single and the double layer of potential formulations, however, were shown to have a non-existence issue at the same eigen-frequencies as the direct Helmholtz integral formulation (Copley, 1968), but for different reasons. To overcome this, a mixed single and double layer formulation was developed by Sayhi, et al. (1981). It is noted here that the

integration surface of the layers of potential formulations here are the actual surface of the sound radiation structure; however, their completeness, the ability to represent any possible sound field, still remains when the integration surface is chosen to be any closed surface inside the actual source boundary. These types of formulations will be reviewed as specific types of Equivalent Source Methods in a later section in this chapter.

2.2.3 The Equivalent Source Methods

Although the Inverse Boundary Element Method has the flexibility that does not require the sound field measurements to be performed on a particular surface geometry or at equal spatial intervals, it is a computationally intensive method since numerical integrations are necessary and usually a very fine mesh is required for high frequency simulations. The Equivalent Source Methods, reviewed in this section, have the further advantages of high modeling efficiency and simplicity in the mathematical formulation. The idea of the Equivalent Source Method (ESM) is to assume that the sound field in the space is the same as that which is generated by some sources (a continuous source distribution or a number of discrete sources) referred to as the equivalent sources. The types of the equivalent sources are specified a priori, and the source strengths (or source locations as well, if not specified a priori) are estimated by minimizing the error between the model-predicted sound field and the measurements. Compared with Finite Element Methods where basis functions (the shape function) are chosen so that the boundary conditions are satisfied and the parameters (the nodal values) are then determined by minimizing the error in the satisfaction of the governing equation, the Equivalent Source Method can be interpreted as: choosing the basis functions (the equivalent sources) to satisfy the governing equation and

then determine the parameters (source strengths, or source locations as well) by minimizing the error in the satisfaction of the boundary conditions. It is also noted that in order to make the construction of the ESM mathematically rigorous, the collection of the equivalent sources assumed in the model should be a complete basis in a sense that any possible solution to the governing equation should be represented by the sound field generated by the equivalent sources with some associated source parameters. Examples of different choices of equivalent sources include: a continuous layer of monopoles (i.e., single layer potential) (Koopmann, et al., 1989) (Fahnline and Koopmann, 1991); a double layer of monopoles and dipoles (i.e., a mix of single and double layer potentials) (Jeans and Mathews, 1992); spherical waves of different orders located at a single point (Ochmann 1995) (Wang and Wu, 1997) and spherical waves at undetermined source locations (Ochmann, 1992). Compared with the single and double layer potential formulations in the Inverse BEM's, the potentials (or distributions of monopoles or dipoles) in ESM's are usually not placed on the actual physical source boundary but, instead, inside the source boundary, and the strength functions (or source strengths) in the ESM's have no direct connection to the sound pressure or normal velocity on the source boundary.

The general formulation for the ESM can be derived by first expressing the actual sound field to be generated by assumed equivalent sources as (von Estorff, 2000) (Ochmann, 1995):

$$p(x) = \iiint_{Q} c(y)q(x,y)dy, \tag{2.11}$$

where Q denotes for the region in which the assumed equivalent sources are distributed, $q(x, y)$ is the sound field expression (evaluated at x) from each source (located at y and with a unit source strength), and $c(y)$ is the source strength at y. Although Eq. (2.11) is written in the form of a volume integral, it could be a surface or line integral if the sources are assumed to be placed on a surface or curve, or it could even be a series summation if discrete equivalent sources are assumed rather than a continuous distribution of sources.

The boundary error can then be calculated as the difference between the measured sound field and the prediction by Eq. (2.11) on the measurement surface (i.e. the boundary):

$$\varepsilon(x) = p_m(x) - \iiint_Q c(y)q(x, y)dy, \tag{2.12}$$

where $p_m(x)$ denotes the measured sound pressure. It is usually a vector of measurements at a number of discrete locations, although it is written as a continuous function, since the vector form can be interpreted as a sequence of direct delta functions with different strengths.

After the boundary error is expressed, as in Eq. (2.12), the source strength, $c(y)$, can be estimated by minimizing the error. Different techniques in the Equivalent Source Methods use different ways to minimize the error; these ways, however, can all be derived from the weighted residue method. Here only the formulation for the case of given measured sound pressure, i.e., the Dirichlet boundary condition, is introduced, and it can be easily extended to other types of boundary value problems (von Estorff, 2000). According to the weighted

residue method, the coefficients for the assumed sources are determined so that the boundary error is orthogonal to the space spanned by a set of chosen weighting functions, $\{w_i(x)\}$, which gives the following equation for all i's:

$$\int_S \varepsilon(x) w_i(x) ds = \int_S \{p_m(x) - \iiint_Q c(y) q(x,y) dy\} w_i(x) ds = 0, \tag{2.13}$$

where S is the measurement surface. Under the constraint that the measured sound pressure, $p_m(x)$, is only available at a number of discrete locations on the surface, the usual treatments for evaluating this surface integral are: (1) sampling the error function and the weighting functions at each of the measurement locations which then turns the integrals into inner products of finite-dimensional vectors; or (2) interpolating the error function based on values at the measurement locations and then evaluating the integral of continuous functions.

It can be shown that the above general equation, Eq. (2.13), can lead to the formulations of different techniques, by substituting different choices of equivalent sources, $q(x,y)$, and different weighting functions, $w_i(x)$. For example: (1) the choice of a collection of discrete simple sources together with weighting functions that are delta functions leads to a collocation method (or matrix inversion solution) (Koopmann, et al., 1989) (Jeans and Mathews, 1992); (2) choosing weighting functions to be the conjugate of each source sound field function leads to the least square solution (or solution from SVD) (Wang and Wu, 1997); (3) if spherical waves are chosen as equivalent sources and weighting functions are the surface normal derivatives of the source function, the formulation is identical to the

Null-field equations (Ochmann, 1995); (4) the two kinds of full-field equations can be derived by replacing the weighting function for the null-field equations with the real part of the source function (first kind) and the conjugate of the source functions (second kind) (Ochmann, 1999).

2.2.4 The Statistically Optimized Near-Field Acoustical Holography

In the Equivalent Sources Method reviewed above, the chosen equivalent sources are usually a finite subset of a complete basis, which means that the sound field prediction from the ESM's gives, if least square method is used in parameter estimations, the projection of the actual sound field to the chosen finite subset of the complete basis, and the components of the basis that are not included in the chosen subset are completely discarded. In another way, the ESM predictions are the optimums only in the space of chosen equivalent sources, while containing no information outside of this space. Statistically Optimized Near-field Acoustical Holography (SONAH) was developed to overcome this limitation: i.e., to find an optimized prediction in a larger space, or even the whole space spanned by the complete basis. In principle, the representation of the sound field by any basis that are complete can be used to formulate a SONAH method, it is, however, more convenient to use plane waves than to use other basis. Compared with the Fourier based methods, in which a plane wave representation is also used, the SONAH method has a smaller error and is easier to handle from a computational point of view (Hald, 2003) (Hald and Gomes, 2006). The idea of SONAH can be extended for other source types (Cho, et al., 2005) but will not usually lead to a formulation that has the same level of simplicity as for plane waves.

To derive the formulation of the SONAH method (Hald, 2005) (Hald, 2009), the prediction of the sound pressure at an arbitrary location in the space is first written as a linear combination of the measured sound pressures:

$$p(x) = \sum_{n=1}^{N} c_n(x)\, p_m(x_n), \tag{2.14}$$

where $p(x)$ is the predicted sound pressure at an arbitrary location, x; $P_m(x_n)$ denotes the measured sound pressure at the nth measurement location x_n, and $c_n(x)$ is the coefficient for the nth measurement which is a function of x. The goal for SONAH is to find the expression for $c_n(x)$ such that the prediction $p(x)$ is an optimum prediction in the space spanned by a complete basis, and, here, the basis of all plane waves is considered. Let $\{\varphi_i\}$ be the complete basis which include infinitely many basis functions. In order to find an optimum prediction in the space spanned by all φ_i's, it is first necessary to derive a finite subset solution of the $c_n(x)$'s that is optimum in sapn$\{\varphi_i\}$ with $i = 1, 2, \ldots M$, and then take the limit as M approaches infinity. This finite subset solution of $c_n(x)$ can be derived by a least square fit to the following set of linear equations:

$$\varphi_i(x) = \sum_{n=1}^{N} c_n(x)\varphi_i(x_n), \quad i = 1, 2, \ldots M\,. \tag{2.15}$$

After defining the matrix and vector notations:

$$A=\begin{bmatrix} \varphi_1(x_1) & \varphi_1(x_2) & \dots \\ \varphi_2(x_1) & \dots & \dots \\ \dots & \dots & \varphi_M(x_N) \end{bmatrix}, \quad \vec{\alpha}(x)=\begin{bmatrix} \varphi_1(x) \\ \dots \\ \varphi_M(x) \end{bmatrix}, \quad \vec{c}(x)=\begin{bmatrix} c_1(x) \\ \dots \\ c_N(x) \end{bmatrix}, \tag{2.16}$$

the least square solution with Tikhonov regularization (Tikhonov, 1963) to Eq. (2.15) is:

$$\vec{c}(x)=(A^H A+\lambda^2 I)^{-1} A^H \vec{\alpha}(x), \tag{2.17}$$

where λ is the regularization parameter, and H denotes the Hermitian of a matrix. When the limit is taken as M approaches infinity, the solution in Eq. (2.17) is then the optimized solution in the space spanned by the complete basis. This leads to the following expressions:

$$[A^H A]_{n,n'} = \lim_{M\to\infty} \sum_{i=1}^{M} \varphi_i^*(x_n)\varphi_i(x_{n'}), \tag{2.18}$$

$$[A^H \vec{\alpha}]_n = \lim_{M\to\infty} \sum_{i=1}^{M} \varphi_i^*(x_n)\varphi_i(x). \tag{2.19}$$

If the sources for the basis, $\{\varphi_i\}$, are chosen to be plane waves, the infinite sum in eqs. (2.18) and (2.19) become integrations in the two-dimensional wavenumber domain, $\vec{k} = (k_x, k_y)$. When using the polar coordinates and the properties of the Bessel functions, these integrals can be reduced analytically to a simple form that is very suitable for numerical integrations. This is the reason why only the plane wave representation SONAH is usually used and SONAH based on other types of basis functions usually results in a more complicated formulation. The specific expressions for the reduced forms of eqs. (2.18) and (2.19) are not reviewed here and can be found in (Hald, 2005) and (Hald, 2009). Different

methods to choose the regularization parameter in Eq. (2.17) were proposed by Gomes and Hansen (2008).

2.2.5 The Treatments of Ill-Posedness

In almost all the sound field reconstruction techniques, the parameter estimation process is an ill-posed inverse problem; one reason is that the sound field always has evanescent components which decays rapidly as the receivers move away from the source and usually have amplitudes less than the noise level at some measurement locations (William, 1999). When the system is inverted, i.e., to calculate the source strength from measurement, the measurement noise, even though small, will be amplified and results in large errors in the calculated parameters. Another cause of the ill-posedness is the under-determined nature of the model that is used to describe the relation between the model parameters and the measured quantities: i.e., a system that has more unknowns than the number of equations. This is usually the case for the Inverse BEM and the Equivalent Sources Method when a large number of lower order sources are used as the equivalent sources. Mathematically, this ill-posedness can be explained by the singular value decomposition (SVD) of the system matrix relating the measurements to the parameters (usually source strengths) (Hansen, 1998). This measurements-parameter relation can, in most sound field reconstruction techniques, be expressed in a discrete linear form (matrix vector form): i.e.,

$$\vec{P}_m = A\vec{c}, \quad A = U\Sigma V^H, \tag{2.20}$$

where $\vec{P}_m$ is the measurements, $\vec{c}$ denotes the parameters (usually the source strengths), A is the system matrix and $A = U\Sigma V^H$ represents the SVD of the system matrix. The inversion of the above system gives the solution (Hansen, 1998):

$$\vec{c} = \sum_{i=1}^{N} \frac{\vec{u}_i^H \vec{P}_m}{\sigma_i} \vec{v}_i, \tag{2.21}$$

where σ_i is the ith singular value (i.e., the ith diagonal element in Σ), usually ordered as $\sigma_1 \geq \sigma_2 \geq \cdots \geq \sigma_N$. When evanescent wave components exist, some of the singular values are close to zero; on the other hand, when model under-determinacy exists, some singular values are exactly zero. In all these cases, the errors in $\vec{P}_m$ are amplified, as seen from Eq. (2.21),which then introduces large error in the calculated parameters.

To deal with this error amplification problem, usually a filter is applied to the singular values, which keeps the large singular values and eliminates or compensates the small singular values. With the filter applied, Eq. (2.21) becomes:

$$\vec{c} = \sum_{i=1}^{N} f_i \frac{\vec{u}_i^H \vec{P}_m}{\sigma_i} \vec{v}_i. \tag{2.22}$$

The commonly used techniques to choose the filter coefficients (f_i), referred to as regularization techniques, are Truncated Singular Value Decomposition (TSVD) (Hanson, 1971) (Varah, 1973) and Tikhonov regularization (Tikhonov, 1963) (Phillips, 1962). For TSVD, the f_i's are chosen to be one for the first *I* singular values and zero for the rest, whereas the Tikhonov regularization uses a smoother filter which has the expression $f_i =$

$\sigma_i^2/(\sigma_i^2+\lambda^2)$ for some parameter λ. The expression for the Tikhonov regularization comes from the idea of balancing the least square solution and the least norm solution to Eq.(2.20) by solving the following minimization problem:

$$\min(\left\|\vec{P}_m - A\vec{c}\right\|^2 + \lambda^2 \left\|\vec{c}\right\|^2). \tag{2.23}$$

The performance of each regularization technique depends on the choice of their regularization parameters: I for TSVD and λ for the Tikhonov regularization. Different parameter choice techniques have been developed based on different criteria. Since the performance of each technique depends largely on the specific problem, no single technique is preferred for all applications. Widely applied techniques include: (1) Generalized Cross Validation (GCV) (Golub, et al., 1979) (Wahba, 1977) in which one element of the measurement data is first removed and then the error at this measurement location is calculated as the difference between this measured data and that predicted based on the remaining data, the regularization parameter is finally chosen to minimize the average of such errors calculated at all the measurement locations; (2) the L-Curve (Hansen, 1992) (Hansen and O'Leary 1993) method, where the norms of the residuals and the norms of the solution vectors are calculated for different parameter choices; when the logarithm of these two norms are plotted against each other on a 2D plane (different points corresponding to different choices of the regularization parameter), the curve of the plot usually forms a L-shape, then the final parameter choice is the one corresponding to the corner point on the L-curve which is regarded as the best balance between the least square and the least norm solution; (3) Normalized Cumulative Periodogram (NCP) (Hansen, et

al., 2006), the idea of which is that the best parameter choice is the one that makes the residual vector closest to white noise, i.e. the Normalized Cumulative Periodogram is closest a straight line; (4) Morozov's Discrepancy Principle (MDP) (Williams, 2001), which gives the parameter choice that makes the norm of the residual is closest to the pre-measured or guessed noise level.

The regularization techniques mentioned above, i.e., the TSVD and the Tikhonov method, are analytical regularizations, meaning that the final regularized solution has an analytical expression, once the regularization parameter is determined. The basic idea behind this type of regularizations is to balance the least square solution and the least norm solution of the original equation. Usually this type of technique can give satisfactory results when the system is not very rank deficient, which means that the rank of the system matrix is not too small compared with the total number of unknown variables. For strongly rank deficient systems, an iterative regularization may give more reasonable solutions, in which iterations are usually performed in a similar way as in the normal gradient-based optimization algorithms, but, after each iteration, some constraints are enforced to ensure the sparsity of the solution, meaning that most elements in the solution vector are zero, or ensure the solution's physical meaning: e.g., some elements in the solution need to be positive. In a recently proposed sound field reconstruction technique, the Wideband Acoustical Holography (Hald, 2014), an iterative regularization is used to ensure sparsity. In some recent work on beamforming, which is not the focus in the review here, since it is a source localization technique rather than a sound field reconstruction techniques, iterative

regularizations to ensure positivity have been widely applied (Brooks and Humpherys, 2006) (Lylloff, et al., 2015).

2.3 A Review of Room Acoustics Sound Field Prediction Techniques

The second (and also the last) step in the modeling process, after the reconstruction of the sound field in free space, is to model the room effect: i.e., the change of the free space sound field because of the existence of the room. The room acoustics simulation techniques can be divided into two categories in general: the wave acoustics methods and the geometrical acoustics methods. In the category of the wave acoustics methods, the prediction of the sound field in a room is treated as finding or approximating the solution to a suitable boundary value problem either analytically or numerically. Analytical approaches can only be applied to problems with simple room geometry and simple boundary conditions (Kuttruff, 2000), thus are not suitable for most realistic room acoustics practices. The numerical solutions, on the other hand, can deal with more complex and realistic problems but are usually computationally intensive, the most widely implemented methods of which are the Finite Element Method (FEM) and the Boundary Element Method (BEM). For the category of the geometrical acoustics methods, sound propagation is modeled as rays, instead of solutions of the wave equations. In room acoustics simulations, methods based on geometrical acoustics are more popular than the methods based on wave acoustics, largely due to its flexibility in dealing with arbitrary room geometries and the simplicity in numerical calculations. The commonly used geometric acoustics models include: the Ray Tracing model, the Beam Tracing model, the Image

Source Model and the Hybrid Models. In this Section the above mentioned room acoustics techniques are generally reviewed.

2.3.1 Methods Based on Geometrical Acoustics

The methods based on geometrical acoustics do not try to solve the governing equation in the room region, but instead combine together individual models describing the sound generation, propagation, reflection, diffraction and reception, respectively, to simulate the signals received at different receiver locations in a room. The geometrical acoustics treatments for these components, although, strictly speaking, they do not give a solution to the governing equations, can nonetheless produce reasonably accurate results for relatively high frequencies. Different modeling techniques for each of these acoustical phenomena in a room environment are reviewed: the fundamental geometrical acoustics models for each individual phenomenon are presented first and it is then described how these fundamental models can be used to construct different room acoustics simulation techniques.

2.3.1.1 Fundamental Models Used in Geometrical Room Acoustics

2.3.1.1.1 Sound Propagation, Sources and Receivers in Geometrical Acoustics

In geometrical acoustics, energy density is usually used to describe the sound field and the sound propagation is usually modeled as rays. Also in the usual practices of geometrical acoustics, only point sources are dealt with. When a wave front is generated by and propagated away from a source in a media without motion, the surface area of the wave

front increases at a factor of the square of the distance, so the energy density decreases at a rate of distance squared. This gives a simple expression for the energy density propagation along a ray of sound:

$$p^2 \sim \frac{1}{r^2}, \tag{2.24}$$

where r denotes the propagation distance from the source. An equivalent interpretation of this expression in geometrical acoustics is that the total energy generated from the source is distributed among a large but fixed number of rays, and the energy carried by each ray stays constant when propagation is in the air, but the number of rays that fall into a unit area on the wave front surface decreases at the rate of the squared distance. Based on this energy relation, a complex sound pressure can be constructed and expressed as:

$$p \sim \frac{e^{-jkr}}{r}, \tag{2.25}$$

where k is the wavenumber. It is noted here that although the propagation expression is the same as a monopole, it is purely based on the assumption of energy distribution on the wave front rather than solving the wave equation.

The above expressions only describe the change of energy density or sound pressure amplitude at a particular point moving with the wave front, but due to the directivity of the source, the energy densities at different locations on the wave front can be different. In geometrical room acoustics, the expression for the energy density for the whole space is simply a multiplication of Eq. (2.24) by the directivity factor (DF): i.e.,

$$p^2 = DF(\theta,\phi)\frac{1}{r^2}, \tag{2.26}$$

which, strictly speaking, does not satisfy the wave equation and can only be understood from the energy assumption mentioned earlier. Receivers are treated in the same way as the sources, i.e., the energy density times the directivity factor of the receiver, and sometimes a visibility factor is also included which is 1 if the source-to-receiver path is not blocked by any obstacles and 0 otherwise.

2.3.1.1.2 Reflection Models

In most geometrical room acoustics practices, the reflection of sound is calculated under the assumption that the room surfaces are locally reacting: i.e., it is assumed that the normal specific acoustic impedance at a point on the surface is independent of the motion at other locations on the surface and thus is not a function of the incidence angle of the incidence wave. This local reaction model is even applied to materials that are known to be non-locally reacting such as porous materials, and still gives reasonable results (Kuttruff, 2000).

To calculate the reflection from an infinite, flat, locally reacting surface from a certain incidence angle, the plane wave reflection coefficient is usually used in geometrical room acoustics even if the source has the sound field expression of a monopole rather than a plane wave. This treatment, although it is wrong in the strict sense, can be shown, by the expansion of saddle point integration, to be an asymptotic expression of the exact solution of the point source reflection when the source is several wavelength above the plane.

(Mechel, 2002) Curved surfaces, whose spatial variations are at lower orders compared with the wave lengths, are usually approximated by small flat polygons in room acoustics, so no special care is taken for dealing with such curved surfaces. (Vorländer, 2008)

However, when non-smooth surfaces are considered (i.e., the spatial variations are at the same order or even higher orders than the wave length), modelling of sound scattering needs to be involved. Similarly, sound scattering cannot be neglected for surfaces with geometric irregularities. Most often, only the hard surface boundary conditions are considered for analytic solutions to non-smooth and irregular surface scattering problems, the most classic results for scattering by non-smooth (corrugated) walls are from Rayleigh (1945); and for scattering by irregularities are from Twersky (1957) and Biot (1968). Although it is possible to include these exact models for scattering in room acoustics simulations, in most practices a simpler approach is preferred: the approach of scattering and diffusion coefficients. In the presence of a rough surface, both specular reflection and non-specular (or diffuse) reflection exist: in specular reflection, the reflected wave generated by a incidence plane wave propagates in a single direction (this is the only type of reflection for flat, homogeneous surfaces); whereas in diffuse reflection, a incident plane wave can produce reflected waves in all directions. The scattering coefficient is the ratio of the energy in non-specular reflection to the energy of the total reflection, which can be measured but includes no information of how the non-specular reflection energy is distributed between different propagation angles. In room acoustics simulations, the random-incidence scattering coefficient is usually obtained from measurements (Vorlander and Mommertz, 2000) and the angular distribution of the diffuse reflection energy is

assumed to follow the Lambert reflection law which assumes a uniform energy density distribution of the diffuse reflection. The diffuse coefficient (Cox, et al., 2006), a measure of how uniform the diffusely reflected energy is distributed in different spatial angles, is not directly applied in room acoustics simulations. Instead, a more general description of the energy distribution pattern, the Bidirectional Reflectance Distribution Function (BRDF), is used when the description in terms of the scattering coefficient and the Lambert law is not satisfactory. (Siltanen, et al. 2007) The BRDF is a function of two directions (four angles in 3D) at each frequency, one for an incidence (incoming) direction and the other for the reflection (outgoing) direction; it describes the portions of the energy carried by an incoming wave from an arbitrary direction that is reflected to any given outgoing directions. (Nicodemus, 1965)

It is noted that the above mentioned reflection models are all for infinite surfaces only. In the case of a finite surface, such as a free-hanging reflector, it is known to add a high-pass filtering effect to the result of infinite surface reflection. One way to model this effect is to construct a high-pass filter and apply it to the reflection coefficients obtained under the assumption of infinite surfaces (Rindel, 1986); or, as a more general alternative, include a diffraction model in the simulation which can also be capable of dealing with surfaces that are connected by certain angles.

2.3.1.1.3 Diffraction Models

Sound diffraction describes the edge-generated sound field (in addition to the reflected sound field) when an incident sound wave propagates to two or more surfaces that are connected together by edges. Since edges are very common features for room geometries, it is important to include the modeling of sound diffraction in room acoustics simulations. The canonical case of sound diffraction in acoustics is the infinite rigid wedge problem, i.e., a plane wave diffracted by two rigid planes connected together by straight edge with a certain angle. Typical treatments for this problem include: (1) Biot and Tolstoy's work which is based on a formulation of wave propagation by Lagrange's equations and using normal modes as generalized coordinates (Biot and Tolstoy, 1957) (Tolstoy, 1975); (2) Morse and Ingard's work which uses the cylindrical wave expansion of the incident wave at the edge (Morse and Ingard, 1968); and (3) Pierce's work where a contour integration in the complex plane is used to describe the diffracted sound field (Pierce, 1981). In room acoustics simulations, one way to include diffraction modeling is the secondary edge source approach, a further development of Biot and Tolstoy's work, which expresses the diffraction sound field from a polygon surface as an integral along the edges of the polygon (Torres, et al. 2001). Another type of secondary edge source model for diffraction, a class of modeling separate from Torres, et al.'s work, can be derived using the Fresnel-Kirchhoff approximation and the Maggi-Rubinowicz transformation (Tsingos and Gascuel, 1998) (Sakurai and Nagata, 1981). One modeling method that is particularly suited for sound diffraction from a thick noise barrier (Pierce, 1974) was developed by using the asymptotic expression of the Pierce's treatment mentioned earlier. As another modeling class for sound

diffraction, there are methods based on geometrical optics such as the Geometrical Theory of Diffraction (Keller, 1962) and the Uniform Theory of Diffraction (Kouyoumjian and Pathak, 1974). In Section 2.3.1.2, it is further commented how these fundamental diffraction models can be included in a practical geometrical room acoustics simulation model.

2.3.1.1.4 The Room Acoustic Rendering Equation

Almost all commonly-used geometrical room acoustics models can be described using a general equation, i.e., the room acoustics rendering equation. Different modeling procedures can be viewed as a different way to solve this equation. The sound energy at a particular point in the room includes the contribution of emitted energy from the whole room surface patches (it is assumed that the geometry of the room surface is represented by surface patches), however, the energy emitted from a single surface patch depends on the energy that is reflected from all the other surface patches to that single patch. The room acoustic rendering equation is used to describe this recursive relation. It is noted that this equation only describes the sound reflections in a room and sound diffraction is not included. Such a formulation is sometimes referred to as the Kuttruff's integral equation (Kuttruff, 1995) (Kuttruff, 2000). This room acoustics rendering equation can be expressed in a form that is directly related to the geometrical acoustics simulations as (Siltanen, et al., 2009):

$$l(x',\Omega) = l_0(x',\Omega) + \int_G R(x,x',\Omega) l(x,\Gamma) dx, \tag{2.27}$$

where $l(x',\Omega)$ is the energy emitted from a single surface patch located at x' to a field point in the room (Ω is the angle between the surface normal vector and the ray connecting this surface patch and the field point); $l_0(x',\Omega)$ is the reflection from the source to the field point or the direction emission if the surface patch at x' is an active source; $I(x,\Gamma)$ is the energy emitted from x to x' (Γ is the outgoing angle). The integral is the contribution from the reflection from all the other surface patches and the reflection kernel, $R(x',x,\Omega)$, is expressed as:

$$R(x,x',\Omega) = V(x,x')\rho(x',\Theta,\Omega)g(x,x'), \tag{2.28}$$

where $V(x,x')$ is the visibility factor as described at the end of Section 2.3.1.1.1; $\rho(x',\Theta,\Omega)$ is the Bidirectional Reflectance Distribution Function (BRDF) of the surface patch at x' (described in Section 2.3.1.1.2) with Θ being the incidence angle from the surface patch at x (the angle between the straight line from x to x' and the normal vector of the surface patch at x') and $g(x,x')$ describes the propagation of a sound ray from x to x' including the factors of time delay, atmospheric attenuation, etc.

The differences among various geometrical room acoustics models mainly revolve around include how the room acoustic rendering equation is sampled and numerically evaluated; what type of BRDF is used and whether additional diffraction models are included or not. It is noted that there are other types of rendering equations (Alarcão, 2005) (Navarro, 2010) which can be derived based on the energy transportation in the room space instead of the boundary based equation, as for Eq. (2.27). These volumetric approaches, however, are not

directly related to geometrical acoustics modeling and are not widely used in room acoustics simulations.

2.3.1.2 Commonly-Used Geometrical Room Acoustics Modeling Techniques

After the introduction of the fundamental models in geometrical acoustics, the commonly-used modeling techniques in geometrical room acoustics are reviewed in this section which use different ways to combine the fundamental models together to simulate the impulse responses at the locations of interest in the room. There are two main modeling categories in general: techniques based on reflection path and techniques based on boundary surfaces. The reflection-path-based techniques primarily focus on describing the propagation path of a sound ray from the source to the receiver at the end and the reflections (and sometimes also diffractions) along the path. The boundary-surface-based techniques, on the other hand, first calculate the time history of the energy distribution on the room boundary surfaces, and then, in a second step, propagate the energy on the boundary to the receiver locations. These two technique categories are not fundamentally different, but the surface-based techniques are more convenient for interactive simulations or when a moving receiver is involved, since the first step can be pre-computed.

2.3.1.2.1 Image-Source Method

The image-source method is a convenient way to describe the specular reflections on the surfaces, but it is not easy to include diffuse reflections and diffraction. The main principle of the image-source method is that the reflected sound field of a source (usually a monopole)

from a flat plane can be represented by another source (i.e., the image source) located at the mirror location of the original source across the plane with its source strength being the strength of the original source times the reflection coefficient of the plane. The angle-dependent plane wave reflection coefficient can be used as explained in Section 2.3.1.1.2. The early image-source model was proposed by Carslaw (1899). This model was later used to calculate the sound field in a rectangular shaped room (Mintzer, 1950) where higher order image sources (images of the image sources) are involved. Computer simulation programs were then developed to calculate the sound field in rectangular rooms (Gibbs and Jones, 1972) (Allen and Berkley, 1979). In order to increase the computational speed of the image-source model, McGovern (2009) proposed a technique to get rid of unnecessary computations by using sorted look-up tables. Further extensions of this image-source method for rectangular spaces include: the use of multipoles to efficiently simulate sound field for a moving receiver or for several receivers at the same time (Duraiswami, et al., 2007); synthesizing the diffuse reverberation based on the energy decay curve obtained from the image-source model (Lehmann and Johnansson, 2008), etc.

While it is possible to calculate the locations of the image sources by specific formulas for rectangular shaped rooms, the higher order image source locations in an arbitrary polygonal room geometry need to be determined by recursively mirroring the lower order sources with respect to each surface in the room. Furthermore, some additional checks need to be performed (Borish, 1984): first, for a particular surface, the image sources behind that surface should not be used to construct new higher order image sources; also, for a particular source, the surfaces that are completely behind other surfaces should not be used

to create new images; moreover, after all valid image sources are constructed, in order for a image source to contribute to energy received at a certain location, a visibility test needs to be performed for each pair of image source and receiver location, which means the reflection path connecting the original source to the receiver needs to hit all its reflecting surfaces at the inside of their boundaries when following the sequence of the surfaces that create that particular image source. The image source method can only be used to calculate the early reflections efficiently, as the number of image sources grows exponentially to an impractically large number at higher reflection orders.

2.3.1.2.2 Stochastic Ray-Tracing Method

In contrast with the image-source method where the reflection paths are found analytically, the ray-tracing methods find the reflection paths and calculate the room impulse responses in a stochastic, Monte-Carlo-like procedure. The very early work on ray tracing was proposed by Allred and Newhouse (1958), and it was then implemented in room acoustics simulations in the late 1960's (Krostad, et al., 1968) (Schroeder, 1970). The general steps for implementing ray-tracing simulations (Vorländer, 2008) include: first emit a large number of sound, plane-wave-like rays from the source in all directions; then track each of the ray paths and modify the path and the amount of energy carried by the ray when hitting each reflecting surface; finally record the sound energy propagating through the neighborhood of the receiver location over time to generate the room impulse response. In the source emission process, the rays can be emitted in either pre-defined directions or in random directions, and if the source has certain directivity patterns, the directivity is used

to weight the strength of the rays that are uniformly distributed in all directions or to weight the directional distribution density of the emitted rays with equal strength. Similarly, in the process of modifying the energy carried by the ray when reflection occurs, one can either modify the energy strength of the ray according to the reflection coefficient of the surface or assign a probability for a ray to be eliminated from all the rays hitting this surface according to surface's absorption coefficient. In the energy recording process at the receiver's locations, the receiver, instead of being a point, needs to have some volume, since the probability for a ray hitting a volume-less point is infinitely small. This volumetric receiver, however, may cause the problem of registering false rays (Lehnert, 1993) as well as the problem of recording the same reflection path multiple times.

One advantage of the ray-tracing method over the image-source method is that it is convenient to include diffuse reflections in ray tracing. There is more than one way to realize the diffuse reflections as well (Vorländer, 2008): the most accurate way is to generate, when a single ray hits surface, one specularly reflected ray and a number of diffusely reflected rays uniformly distributed in all directions in the half space, where the total energy assigned to the diffuse reflections is determined by the scattering coefficient and the Lambert law, or, secondly, the BRDF can be used to determine the strength of each diffuse ray in its particular direction. A computationally more efficient way is to generate only one single ray when a ray hits a surface, but give the generated ray a certain probability (depending on the scattering coefficient) to become a specular reflection or a diffuse reflection, and the probability of the direction of the diffuse reflection is similarly assigned by the Lambert law or the BRDF. Another way, the vector mixing model, linearly combines

the specular and diffuse ray together to form a single ray. Edge diffraction can also be added to ray-tracing methods by modifying rays close to edges (Mehta and Mulholland, 1976) (Christensen and Rindel, 2005). The relation between the number of rays and the accuracy has been studied by Vorländer (2008).

2.3.1.2.3 Beam-Tracing Method

Instead of using a straight lines to represent the propagation path and using a volumetric receiver in ray-tracing methods, the beam-tracing technique uses volumetric beams to represent the path and a point receiver. The term, beam tracing, however, can be referred to two different techniques in room acoustics: one is an extension of the stochastic ray-tracing method, the other, sometimes referred to as deterministic beam tracing, is used as the first step in image-source method to efficiently calculate the image source locations in a complicated room geometry.

The very early work, still a currently widely-used version, of the stochastic beam-tracing technique (Haviland and Thanedar, 1973) (Walsh, 1980) uses pyramid-shaped beams by dividing the sphere around the source into triangles. When a pyramidal beam hits the intersections of more than one surface, the beam is split into several beams whose beam cross-section change from triangles to polygons, the exact shapes of which depends on the geometry of the surface intersections. As an alternative to the pyramidal beam shape, the geometry of a circular-cone shaped beam can also be used (van Maercke, 1986), one problem brought by which is that there will be overlaps among the beams if circular disks

are used to cover a sphere. This problem can be handled by weighting the energy contribution inside a beam such that the energy is closer to zero when a receiver is located closer to the boundary. Another way to implement beam tracing is to still use volume-less rays but to allow the volume of the receivers to increase along with the rays' propagation distance (Vorländer, 1989). It is noted here that most beam-tracing methods, except for pyramidal beam-tracing, can conveniently handle the issue of beam splitting when hitting multiple surfaces. As with ray-tracing methods, it is also possible to include diffuse reflection (Dalenbäck, 1996) and diffractions (Chandak, et al., 2008) in beam tracing.

The second type of beam-tracing, deterministic beam tracing, is used as a more efficient alternative to finding the valid image sources (described in the image-source method section). In traditional image-source methods, the image sources are found by mirroring all lower order sources with respect to all surfaces and then removing the invalid image sources. In this family of beam tracing, the first order image sources are found in the same way, and then beams are formed by connecting each first order image source to the edges of the surface that were used to create this first order source (one single beam for one first order source). These beams are then traced and reflected on each encountered surface, and each reflection creates a new image source. In this process, all the created image sources are valid, thus there is no need to check and remove the invalid sources (Stephenson, 1996) (Funkhouser, et al., 2004). Another advantage of this type of beam tracing over the traditional image-source methods is the possibility to include diffractions (Tsingos, et al., 2001).

2.3.1.2.4 Radiosity Method

In contrast with the three previously introduced path-based methods, the radiosity method is a surface-based method, which, as mentioned before, first involves calculating the energy distributed on the room surfaces and then propagating the energy from the surfaces to the receivers. The basic radiosity method directly applies the room acoustics rendering equation, Eq. (2.27), and assumes ideally diffuse reflection: i.e., the BRDF is assumed to be constant. This method can be used to calculate the reverberation time (Gilbert, 1981) (Kuttruff, 1997), the room response (Moore, 1984) or the late reverberation part of the room response (Lewers, 1993). The details of how to implement this method to simulate the sound field in a diffusely reflecting room with arbitrary shape was presented by Nosal et al. (2004). The theoretical equivalence of this method to the stochastic ray-tracing method was demonstrated by Le Bot and Bocquillet (2000).

One extension of the basic radiosity method is to use a non-constant BRDF to account for more general surface reflection properties, which is sometimes referred to as the method of acoustic radiance transfer (Siltanen et al., 2007). In this case, the surface needs to be discretized into patches to use the angle-dependent reflection properties. It is also noted here that it is usually more efficient to implement this type of radiosity method in the frequency domain rather than the time domain (Siltanen et al., 2009).

2.3.1.2.5 Hybrid Methods

In geometrical room acoustics, hybrid methods are used to compute the room responses by combining several different methods mentioned above, which typically use the path-based methods for the early reflections (dominated by specular reflections) and the surface-based methods for the later reverberations where diffuse reflections are more important (Lewers, 1993) (Tenenbaum, et al., 2007). Recently, Koutsouris et al. (2013) proposed a data-driven method to switch from specular reflection mode to the diffuse reflection mode. Another type of hybrid method, developed by Aretz (2012), involves using finite element simulation for the low frequency components and the geometrical acoustics simulations for high frequencies.

2.3.2 Methods Based on Wave Acoustics

Simulations based on the Boundary Element Method (BEM) and Finite Element Method (FEM) are two types of widely-used wave-based techniques in room acoustics. Solutions to the Helmholtz equation in terms of acoustic modes in the room is also an important category in wave-based method for room acoustics; this modal method, however, is not commonly used in room acoustics simulations, since it cannot be easily applied to arbitrary room geometries or be used to deal with general impedance boundary conditions. The BEM for room acoustics is no different to the BEM described in Section 2.2.2 for modeling the free-space sound field, thus only the FEM in room acoustics is briefly introduced here (Aretz, 2012) (Van Hal, et al., 2003) (Van Genechten, et al., 2009).

The finite element formulation, a weak form formulation of an acoustics problem, can be derived either by using the weighted residue method (Fish and Belytschko, 2007) or based on the fundamental theorem of calculus of variation (Shames and Dym, 1995). Firstly, the Helmholtz equation is multiplied by an arbitrary weighting function, $w(x)$, and integrated over the room region, which gives:

$$\int_{\Omega} w(\nabla^2 p + k^2 p + j\omega\rho_0 q)d\Omega = 0, \tag{2.29}$$

where k denotes the wavenumber; q denotes the strength of volume source distribution in space. Then, Green's first identity is applied to this volume integral, which results in:

$$\int_{\Omega} (-\nabla w \nabla p + wk^2 p + wj\omega\rho_0 q)d\Omega + \int_{\Gamma_p \cup \Gamma_v \cup \Gamma_z} w\frac{\partial p}{\partial n} d\Gamma = 0, \tag{2.30}$$

where the second term is the surface integral over the boundary of the room region. The boundary is composed of the surfaces with one of the three types of boundary conditions: surface with pressure boundary condition, Γ_p; surface with normal velocity boundary condition, Γ_v, and surface with impedance boundary condition, Γ_z. It is noted that the weighting functions are chosen arbitrarily, but with one constraint: it is zero on Γ_p. Thus the weak form for the finite element formulation is derived after applying the boundary conditions:

$$\int_{\Omega} (-\nabla w \nabla p + wk^2 p + wj\omega\rho_0 q)d\Omega + \int_{\Gamma_v} w(-j\omega\rho_0 v_n)d\Gamma + \int_{\Gamma z} w(\frac{-j\omega\rho_0}{Z_s} p)d\Gamma = 0, \tag{2.31}$$

where v_n is the specified normal velocity boundary condition and Z_s is the impedance boundary condition. In most FEM applications, both the weighting function, w, and the sound field, p, are discretized and approximated by the same shape functions on a mesh of the room region: i.e., the Galerkin method is used. After this discretization, the above equation, Eq. (2.31), can be written as a matrix system with the nodal values of the sound pressure on the mesh being the unknowns:

$$(K + j\omega A - \omega^2 M)\vec{p} = j\omega\vec{f}, \tag{2.32}$$

in which $\vec{p}$ is the vector containing the nodal values of the sound pressure; *K* and *M* are the compressibility matrix and the mass matrix resulting from the volume integral of the terms $-\nabla w \nabla p$ and $k^2 p$, respectively; the damping matrix, *A*, is obtained from the surface integral on Γ_z; and the excitation vector, $\vec{f}$, resulting from the combination of the velocity boundary condition term and the volume source term. The solution of this problem can be found by solving the above linear system for the nodal sound pressure values.

CHAPTER 3. FREE-SPACE SOUND FIELD PREDICTION USING MULTIPOLE EQUIVALENT SOURCE MODEL WITH UN-FIXED SOURCE LOCATIONS

3.1 Introduction

As mentioned in the Introduction (Chapter 1), the first step of the simulation is to predict the free-space radiation of the source. It is recalled here that the problem of this step is to predict the sound field everywhere in an anechoic environment based on the sound field measurements at a finite number of locations. The efficiency of the modeling (specifically, the number of model parameters required to achieve enough prediction accuracy) for this step is important since it affects not only the computational intensity of simulating the free-space sound field itself, but also that of the room acoustics simulation, since the result of this step will be taken as an input to the next operation (room acoustics prediction). From this concern, it is generally undesirable to implement the computationally intensive models such as Finite Element Models (FEM) or Boundary Element Models (BEMs), and thus the idea of using techniques in the area of acoustic holography (or improved methods based on them) is a natural alternative. In some applications, the predictions are based on the given distribution of the normal velocities on the source surface; in this chapter, however, it is focused on the case of using measured sound pressure as input, since the method discussed here, as mentioned in Section 2, can easily be modified to treat the case of having normal velocity inputs.

From the review of the various free-space sound field reconstruction techniques in Chapter 2, it is seen that in the area of acoustical holography, the existing techniques can be broadly classified into parametric and non-parametric methods. In the non-parametric methods, often referred to as Fourier-based holography, the sound field is decomposed into a set of orthogonal basis functions using measurements in a geometry where orthogonality applies (Williams and Maynard, 1982) (Maynard, et al., 1985) (Williams, et al., 1987). In the category of the parametric methods, however, it is assumed that the actual sound field is equivalent to that generated by a combination of some wave or source components with undetermined parameters and those parameters are estimated using measured data. Techniques in the parametric category can, in general, be viewed as equivalent source methods. In classical Equivalent Source Methods (ESM), the sound field is approximated by a distribution of simple sources, say monopoles or dipoles, with fixed locations (Koopmann, et al., 1989) (Fahnline and Koopmann, 1991) (Jeans and Mathews, 1992). Inverse Boundary Element Methods (IBEM) (Veronesi and Maynard, 1989) (Kim and Lee, 1990) (Saijyou and Uchida, 2004), although derived from the Helmholtz equation, can also be interpreted as using a distribution of monopoles (pressure terms) and dipoles (normal velocity terms) on a closed boundary. In addition to methods in which a spatial distribution of simple, lower order sources is used, higher order sources with one fixed location can also be used as equivalent sources. Spherical harmonics were chosen in the initial proposal of the Helmholtz Equation Least Squares (HELS) method (Wang and Wu, 1997) (Wu and Yu, 1998) (Rayess and Wu, 2000) in which parameter estimation was performed through a least square method. The HELS method was extended to the use of any arbitrary set of higher order sources. The Statistically Optimized Near-field Acoustical Holography

(SONAH) method (Cho, et al., 2005) (Hald, 2009) can also be viewed as a member of the higher order, single location category, in which a wave expansion of various types can be used with the wave strengths calculated, however, implicitly, as opposed to the HELS method. In the techniques using higher order sources, additional flexibility can be achieved by adapting un-fixed sources: i.e., the locations of each of the component sources can be different and they need to be estimated as a subset of parameters together with the source strengths, Ochmann (1992) has implemented a model similar with spherical waves.

In the work described in this chapter, an ESM with higher order sources and un-fixed source locations is proposed which uses the multipole series of monopoles, dipoles, quadrupoles, octupoles and higher orders. With the additional flexibility of the undetermined source locations, it should, in principle, require fewer number of model parameters to reach the desired prediction accuracy. The use of the multipole sources instead of the usual spherical waves is more convenient than the usual techniques in this category, if the reconstructed free-space sound field will be inputted into another model for further processing: e.g., a room acoustic model to predict the sound field from the same source but in different rooms as in the work of this document. This follows because each multipole source, after its strength and location are calculated, can be treated as a combination of closely located monopoles and the models following this free-space sound field prediction only need to consider the simple case of having a monopole source. This is also much more convenient when the free-space sound field needs to be physically reconstructed (i.e., to generate the same sound field by using a number of loudspeakers), since multipoles can easily be physically realized using a number of small loudspeakers

(Beauvilain, et al., 2000). The parameter estimation, in this work, is divided into two parts: a linear optimization for source strengths and a non-linear optimization for source locations. The effects of different degrees of non-collocation and the effects of regularization methods were also investigated. The implementation of this method in the prediction of the sound field in both the near and far fields was validated through a measurement of a loudspeaker.

3.2 The Model of Multipole ESM with Un-Fixed Source Locations

The multipole model with un-fixed source locations, as compared with a model involving fixed, single location, higher order sources, allows more flexibility in model structure and thus, in principle, is more likely to approximate a sound field using a smaller number of sources. The source sequence consisting of monopoles, dipoles, quadrupoles and higher orders was chosen to be the equivalent sources used in this model; thus, the sound field expression of each individual source should be derived as the first step in constructing the model. Then an appropriate parameter estimation method needs to be proposed to determine the locations and strengths of the various source components. It is noted here that one necessary requirement for a series of sources being used as equivalent sources to represent a sound field is that the chosen source series needs to be complete, i.e., the series can, with appropriate source strengths and source locations, converge to any possible free-space sound field, if the included source order approaches infinity. The proof of this completeness property for the multipoles are demonstrated in the Appendix along with discussions of the linear dependence relations among different source orders.

3.2.1 The Sound Fields of the Multipoles

The terminology used in this paper regarding the multipole sequence is as follows: the monopole is referred to as a source of order zero, the dipole as a first order source, etc. As in the convention in acoustics, a monopole with strength S_0 is defined to be a source that radiates the sound field

$$P_{S0}(\vec{X}\left|\vec{X}_0,\omega\right.) = S_0 P_0(\vec{X}\left|\vec{X}_0,\omega\right.) = S_0 \frac{e^{-jk\left\|\vec{X}-\vec{X}_0\right\|}}{4\pi\left\|\vec{X}-\vec{X}_0\right\|}, \tag{3.1}$$

where $\vec{X}_0$ is the source location, $\vec{X}$ is the receiver location and $k = \omega / c$ is the wavenumber. This is an outgoing monopole when time dependence is assumed to be $e^{j\omega t}$.

Based on this definition, a source of order n ($n > 0$) can be constructed as a combination of two closely placed $(n-1)$st order sources with the same strength but opposite sign, and aligned in the direction $\vec{u}_n$, where $\left\|\vec{u}_n\right\| = 1$. Thus the sound field of an n th order source can be written as:

$$P_{Sn}(\vec{X}\left|\vec{X}_0,\omega\right.) = d_n \nabla_{\vec{u}_n} P_{Sn-1}(\vec{X}\left|\vec{X}_0,\omega\right.) = S_{n-1} d_n \nabla(P_{n-1}) \bullet \vec{u}_n, \tag{3.2}$$

where d_n (a small number) is the distance between the two lower order sources, P_{n-1} denotes the sound field of the $(n-1)$st order source with unit strength, and ∇ is the del operator. It is also defined that the strength of the n th order source is $S_n = d_n S_{n-1}$.

From the iterative formula above, the explicit expression for a general n th order source can be written in tensor form as (Liu, 2011):

$$P_{Sn} = S_n P_n = S_n R_n(P_0) \bullet \vec{u}_1 \bullet \vec{u}_2 ... \bullet \vec{u}_n, \qquad R_n = \nabla^{\otimes n}, \tag{3.3}$$

where the strength $S_n = S_0 d_1 d_2 ... d_n$, $\otimes$ denotes the tensor outer product, $\nabla^{\otimes n}$ indicates performing the outer product on the del operator n times, and $(\bullet)$ denotes the tensor inner product. It can be seen that the tensor R_n has a rank of n and has 3^n components in total.

When it is noted that partial derivatives do not depend on the sequence of differentiation for smooth functions, it is seen that the tensor possesses a symmetric property meaning that not all components in the tensor are independent. This leads to the fact that the sound field of an arbitrarily-oriented n th order source can be decomposed into a combination of multipoles with a standard configuration of that source order, each of which can be expressed as: $\frac{\partial^n}{\partial x^{i_1} y^{i_2} z^{i_3}} \left(\frac{e^{-jkr}}{4\pi r}\right)$, with $i_1 + i_2 + i_3 = n$ and r being the distance from source location to receiver location. The determination of the number of multipoles in each order is a standard combination-with-repetition problem: i.e., the function $\frac{e^{-jkr}}{4\pi r}$ is differentiated n times, for each time, one direction is chosen from three different directions (i.e., the x, y or z directions) and the order in which the differentiation is performed does not matter. Thus the number of multipoles in each order can be calculated as:

$$N(n)=\begin{cases}1\ , & n=0\\ C_{n+2}^{n}, & n>0\end{cases}, \tag{3.4}$$

where C_a^b denotes the combination number resulting from choosing b out of a, and where n is the source order. Specifically, the dipole has 3 standard configuration components, the quadrupole has 6 and the octupole has 10 and so on.

3.2.2 Model Construction

To construct the model, it is assumed that measurements of the sound field are obtained at different locations $\vec{\zeta}_1,\vec{\zeta}_2,...\vec{\zeta}_W$, and that the equivalent sources consist of M_0 monopoles, M_1 dipoles, etc., up to M_N sources of order N. By arranging the equivalent sources into a vector with a global index, instead of two indices, representing the number of sources for each order, the relationship between the measured sound pressures and the equivalent sources can be written as:

$$\begin{bmatrix}P_1(\vec{\zeta}_1,\omega)\\ P_2(\vec{\zeta}_2,\omega)\\ ...\\ P_M(\vec{\zeta}_M,\omega)\end{bmatrix}=\begin{bmatrix}g_1(\vec{\zeta}_1|\vec{X}_1,\omega) & g_2(\vec{\zeta}_1|\vec{X}_2,\omega) & ... & g_W(\vec{\zeta}_1|\vec{X}_W,\omega)\\ g_1(\vec{\zeta}_2|\vec{X}_1,\omega) & ... & ... & ...\\ ... & ... & ... & ...\\ g_1(\vec{\zeta}_M|\vec{X}_1,\omega) & ... & ... & g_W(\vec{\zeta}_M|\vec{X}_W,\omega)\end{bmatrix}\begin{bmatrix}Q_1(\omega)\\ Q_2(\omega)\\ ...\\ Q_W(\omega)\end{bmatrix}, \tag{3.5}$$

where P_i is the measured sound field at the ith location, g_j denotes the unit strength sound field of the j th source in terms of the global index, and Q_j is the strength of the jth source.

In the above equation, the source locations, $\vec{X}_j$,and the corresponding strengths, Q_j , are the parameters to be estimated, while the measurement locations, $\vec{\zeta}_i$, are known from the design of the measurement. The main difference between this model structure and that of a model using fixed source locations is that an additional set of parameters, $\vec{X}_j$, needs to be estimated. In the present work, two types of un-fixed source locations models are discussed: the collocated model and the non-collocated model. In the former category, all sources are located at the same undetermined location, whereas in the latter category, the sources in different orders can have different undetermined source locations but the sources of the same order have the same source location.

3.2.3 Parameter Estimation Process

Equation (3.5) is in the form of $\vec{P} = A(\vec{X})\vec{Q}$; thus the parameters, $\vec{X}$ and $\vec{Q}$, can be determined by solving the following optimization problem:

$$\min \left\| \vec{P} - A(\vec{X})\vec{Q} \right\|^2 . \tag{3.6}$$

This problem is essentially a non-linear optimization, since the matrix A is not constant but depends on $\vec{X}$. However, it is observed that if the source locations are known, the estimation of the source strength is a linear least squares problem. Based on this observation, the parameter estimation process used here is based on a non-linear optimization algorithm that updates the source locations only, and within each update, the strengths are determined by a linear process.

The linear part of the problem, i.e., the estimation of source strengths with given source locations, is accomplished by a standard least square solution in combination with a certain regularization method since the problem is often ill-posed (Nelson and Yoon, 2000) (Yoon and Nelson, 2000). Generally speaking, there are no regularization methods that can be declared better than the others before comparing the results. Therefore the effects of different regularization types are compared later in this chapter.

In the part of the non-linear optimization that updates source locations, the Trust Region Reflective Method (Coleman and Li, 1996) was chosen due to its quadratic convergence rate and the ability to handle relatively large number of parameters; moreover the requirement of the existence of the Hessian matrix of the cost function can be met in this problem. In principle, the source locations do not necessarily need to be allowed to move in all three degree of freedoms. For example, it can be assumed that some of the sources have the same location, or that they are only allowed to move along a line or on a plane, etc. Such constraints are sometimes helpful to reach a balance between flexibility of the model and the capability and speed of the optimization algorithm.

3.3 Implementation of the Multipole ESM's

The model implemented in this chapter includes all the standard configurations of multipoles (the independent components of the tensor in Eq. (3.3)) from monopole to octupole: i.e., one monopole, three dipoles, six quadrupoles and ten octupoles. In addition, the sources of the same order are constrained to have the same location and all source

locations should be within the volume of the physical, vibrating object (e.g., the loudspeaker in the experiment described below).

Since the calculation of the sound field involves evaluation of n th order derivatives of a monopole sound field, two possible approaches can be used: a) analytical evaluation as in Eq. (3.3); or a b) finite difference method. Here, the analytical process was implemented.

The particle velocities associated with a particular pressure field, necessary for the prediction of intensity, were evaluated analytically by using

$$\vec{V}_{sn} = -\frac{1}{j\omega\rho}\nabla(P_{sn}), \tag{3.7}$$

where ρ is the air density. In the actual implementation, it is most convenient to treat $\nabla(P_{sn})$ as the pressure expression of an $(n+1)$st order source.

In carrying out the Trust Region Reflective algorithm, the Jacobian of the cost function was calculated by forward finite difference, the maximum number of iterations and function evaluations were set to be 400 and 800, respectively, and the tolerance for determining a local minimum was 1×10^{-6}.

3.4 Experimental and Numerical Results

Experimental measurements were conducted to validate the proposed multipole Equivalent Sources Models, in which the sound field generated by a loudspeaker in an anechoic

environment was measured and compared with the prediction from the proposed models. The performances of the multipole ESM's with different flexibilities (i.e., different constraints on the undetermined source locations) were compared. Three types of models with different flexibilities were investigated: fixed-location model (all equivalent sources are fixed at a certain location); collocated model (all equivalent sources have the same but un-fixed source location); non-collocated model (equivalent sources of different orders have different un-fixed source locations, but sources of the same order have the same location). Also for the purpose of demonstrating the use of the proposed models in source visualizations, the sound pressure distribution over the loudspeaker surface was predicted using the collocated model which was then verified with a BEM prediction where the vibrating velocity measured by a laser vibrometer was used as the BEM boundary condition.

3.4.1 Description of the Experiment

The loudspeaker used in this experiment is an Infinity Primus P163 with a dimension of $0.265\ \text{m} \times 0.207\ \text{m} \times 0.37\text{m}$, the sound field of which was measured in an anechoic environment (shown in Figure 3.1). Sound pressure measurements were performed both in the near field and far field on six planes around the loudspeaker with each plane parallel with a corresponding face on the loudspeaker. The measurement locations are shown in Figure 3.2, where the distance between the near-field measurement plane and the corresponding face of the loudspeaker is around 0.3 m, and the distance for the far-field plane was 0.9 m. Note that the distances from the measurement planes to the loudspeaker faces are not exactly the same in either the near field or the far field measurement; however, the exact coordinates of each microphone was measured and was used in the model

constructions, since, from the model construction process described in Section 3.2, it is noticed that it is not necessary to guarantee all microphones having the same distance to the source as long as the coordinates of each microphone are known. There were 54 measurement points on each face (a total of 324 near-field measurement points and another 324 far-field measurement points) which were measured separately by using a 18-channel planar microphone array (Brüel & Kjær, sliced wheel array WA-1558-W; microphones: Brüel & Kjær, Type 4959). The sampling frequency in this experiment was 65.5 k Hz, and in the calculation of the frequency response of each microphone measurement to the input signal, the H1 estimator was used (8 Hz frequency interval up to 25.6 k Hz, 100 averages from 0.125s time segments with 50% overlap).

Figure 3.1. Photos of the experimental setup.

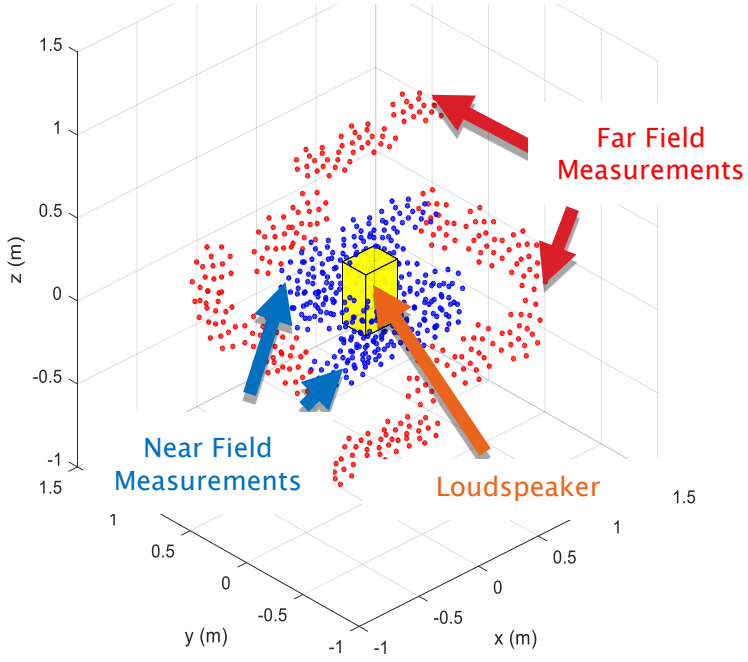

Figure 3.2. The spatial distribution of the measurement locations in the experiment.

The separate measurements were synchronized together to obtain the effectively simultaneously measured signals at all the receiver locations by using the transfer matrix method (Kim, et al., 2004) (Lee and Bolton, 2006) with one reference signal, the input signal to the loudspeaker. As required by the transfer matrix method, the number of reference signals used in the synchronization should be no less than the number of uncorrelated sources existing in the measurement. To verify the satisfaction of this requirement in this experiment, singular value decompositions were performed at each frequency on the cross power spectrum density matrix for a simultaneous 18-channel measurement in front of the loudspeaker. The first three largest singular values for each frequency were then plotted in Figure 3.3, from which it is observed that there is only one significant singular value for each frequency and all the other singular values are at least

30 dB lower than the first one. This indicates that there is only one main sound source and the other singular values represent the ambient noise. Thus only one reference signal is needed to synchronize all the separate measurements together.

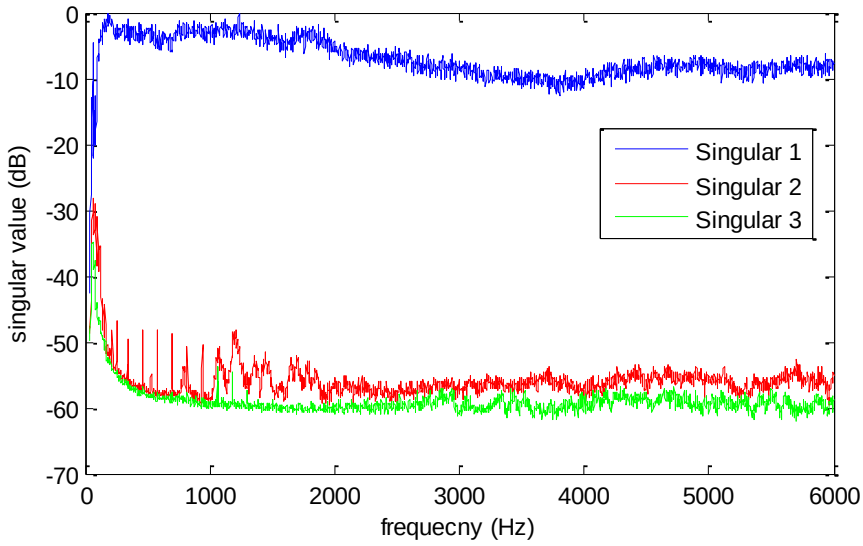

Figure 3.3. The first three singular values of the cross power spectrum density matrix for a simultaneous 18-channel measurement in front of the loudspeaker.

In the model construction process used in this experiment, all the multipole ESM's, regardless of what flexibility was chosen, contained a multipole series up to order 3 (i.e., up to octupole), and the 324 near-field measurement data were used to estimate the source strengths as well as the source locations in the model. With the calculated parameters, the sound pressures at the 324 far-field measurement locations were predicted by the ESM, and were then compared with the measured far-field sound pressure to investigate the performance of the models. From Eq. (3.4), it can be calculated that there are 20 multipoles in total if the series includes sources up to order 3 as in the current experiment which results in the system matrix in Eq. (3.5) being a 324 by 20 matrix for each frequency. Figure 3.4

shows a typical distribution of the 20 singular values of this matrix (the distribution does not change significantly with different frequencies or different source locations), in which there exists a very sharp transition at the 16th singular very and the singular values after the 16th are very close to zero. This feature can be explained by the linear dependence relations among different multipole order, which is discussed in detail in the Appendix. It is also concluded, in the Appendix, that the number of linearly independent multipoles is the same as the number of components included in the spherical wave series up to the same order, which, if the calculation is carried out, gives exactly 16 for multipoles up to order 3. Because of this linear dependence relation, a truncated singular value decomposition has been perform at the 16th singular value when finding the least-square solution to Eq. (3.5) to estimate the strengths of the equivalent sources.

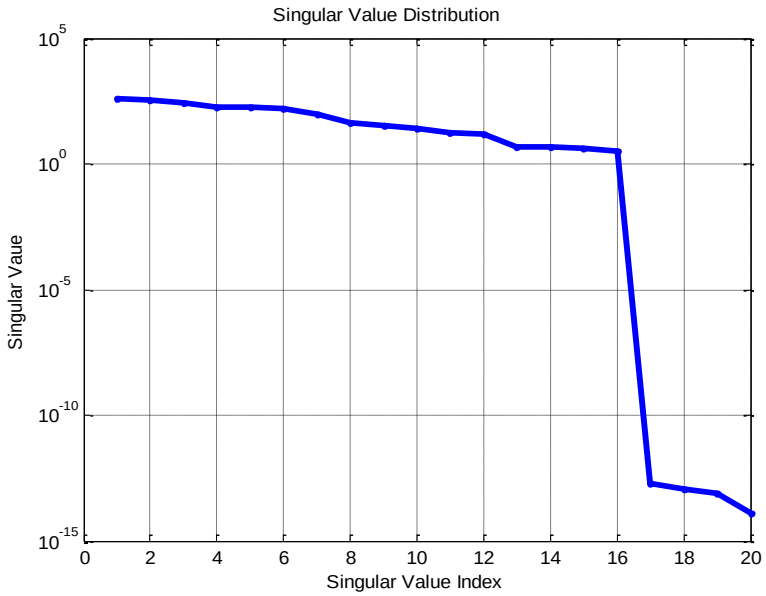

Figure 3.4. A typical singular value distribution of the system matrix for multipole ESM.

3.4.2 Validate and Compare ESM's with Different Flexibilities

As mentioned before, the model parameters were estimated using the near-field measurement data, and the model performance (i.e., the accuracy of the model predicted sound field) is indicated by comparing the measured and the model predicted sound pressure at the 324 far-field measurement locations. For the fixed-location model, all the equivalent sources were placed at the center of the loudspeaker; for both the collocated (all source locations were the same but undetermined) and the non-collocated models (sources of different orders can have different locations but the sources of the same order have the same location), the source locations were constrained to move only within the loudspeaker. The initial guesses of the source locations in both the collocated and the non-collocated models were all at the center of the loudspeaker for the lowest frequency component and the calculated source locations for the current frequency component was used as the initial guess for the next (higher) frequency component.

Results for models with three different flexibilities (i.e., the fixed-location model, the collocated model and the non-collocated model) are shown in Figure 3.5 to Figure 3.11, where the predictions from each of these three models are compared with the measurement at the frequencies of 400 Hz, 1 kHz, 2 kHz, 3 kHz, 6 kHz, 10 kHz and 20 kHz respectively. The microphone indices from 1 to 54 are on plane parallel to the front face of the loudspeaker; 55 to 108 the right face; 109 to 162 the back face; 163 to 216 the left face; 217 to 270 the top face; and 271 to 324 the bottom face. It is clearly observed that predictions from the fixed-location model are accurate up to 2 kHz, however, starting at 3 kHz the model performance is deteriorating, and for frequencies of 6 kHz and above, no

meaningful predictions are obtained from the fixed-location model. The other two models, i.e., the collocated and the non-collocated models, both achieve good prediction accuracies for all the frequencies. Although small mismatches to the measurement can be found for the predictions from the collocated and the non-collocated models, it is noted here that the plots shown in those figures are in linear scales, and these discrepancies become much less noticeable if decibel scales are used. The highest frequency shown here, 20 kHz, is already the upper limit for the human audible frequency range, so it is concluded that the collocated and the non-collocated models can be used to reconstruct the sound field for the whole audible frequency range, at least for sources similar to the loudspeaker used in the current experiment.

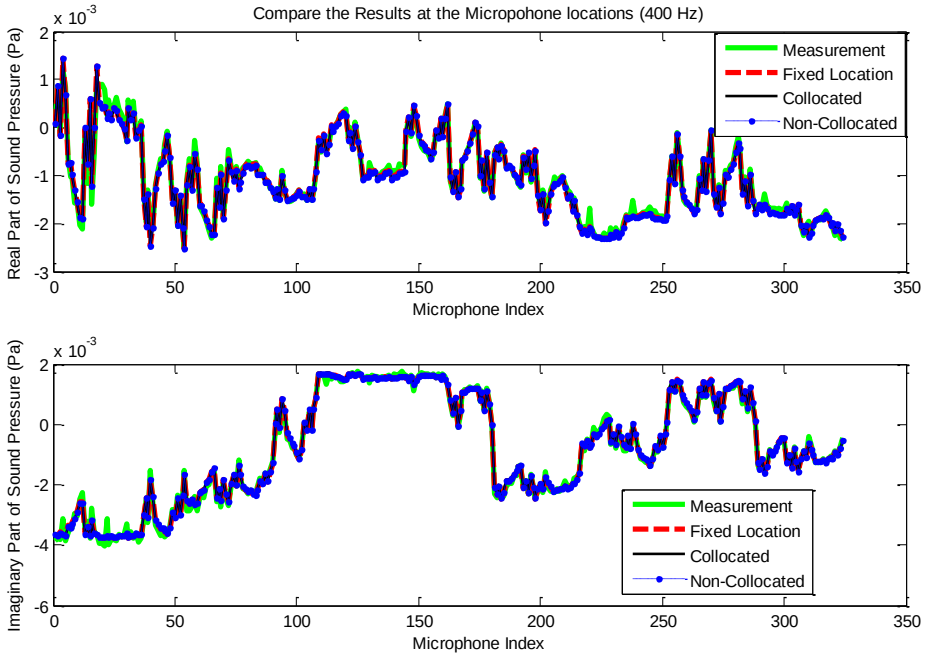

Figure 3.5. Performance comparison among ESM's with different flexibility at 400 Hz.

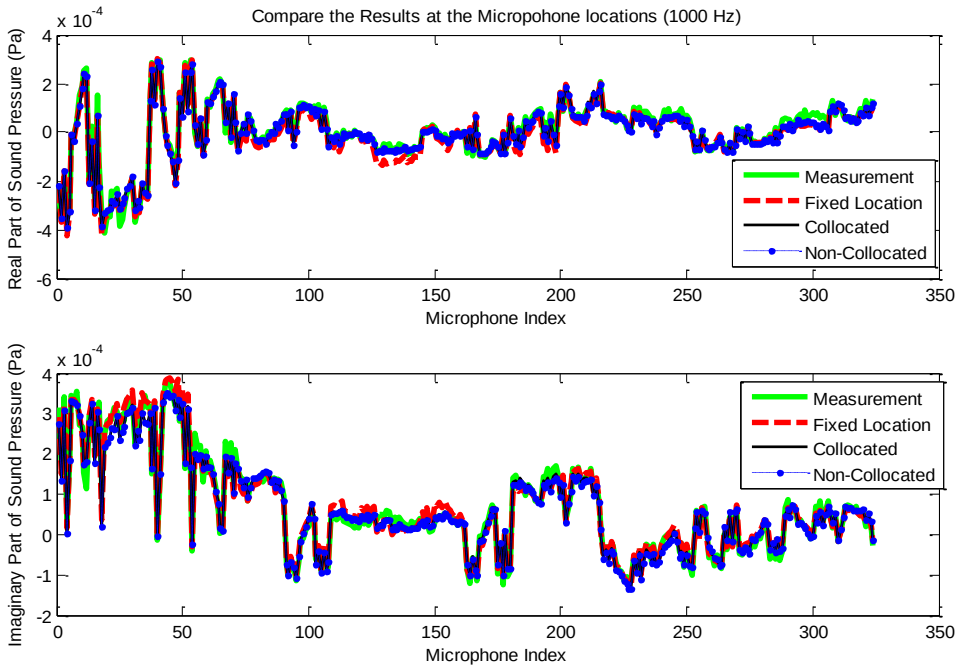

Figure 3.6. Performance comparison among ESM's with different flexibility at 1 kHz.

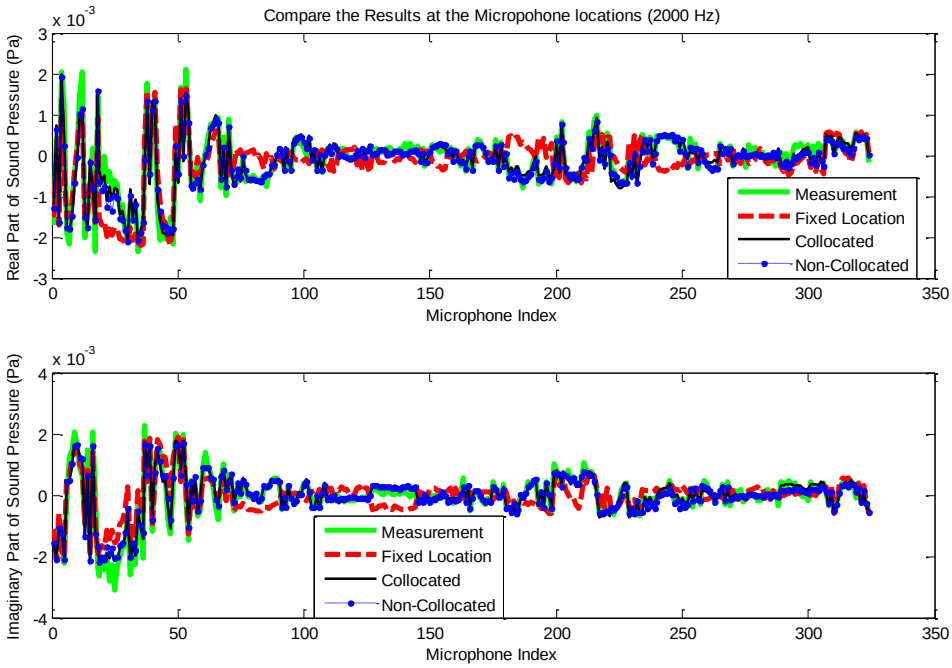

Figure 3.7. Performance comparison among ESM's with different flexibility at 2 kHz.

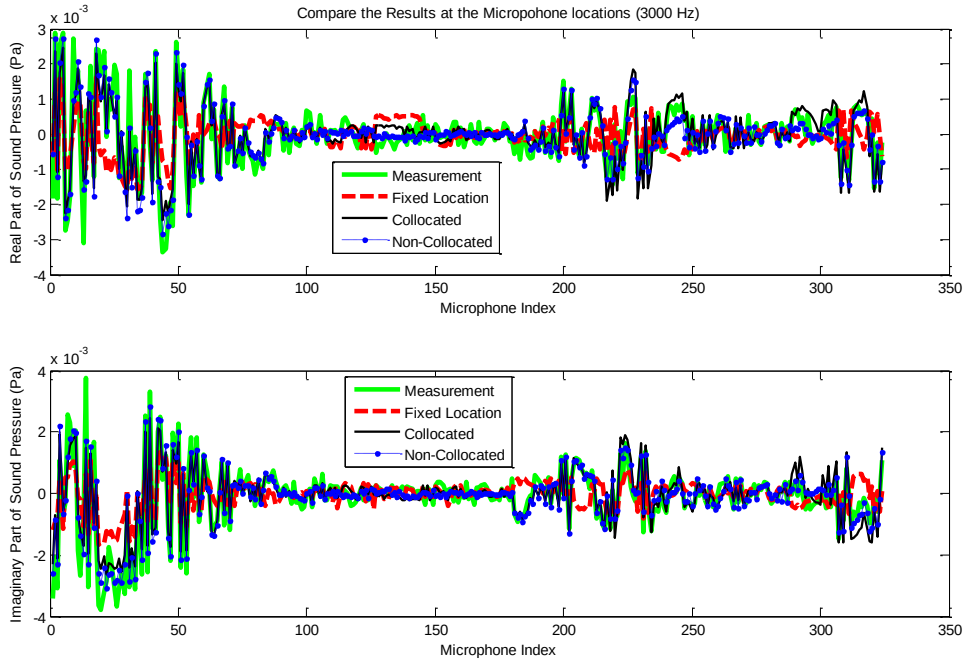

Figure 3.8. Performance comparison among ESM's with different flexibility at 3 kHz.

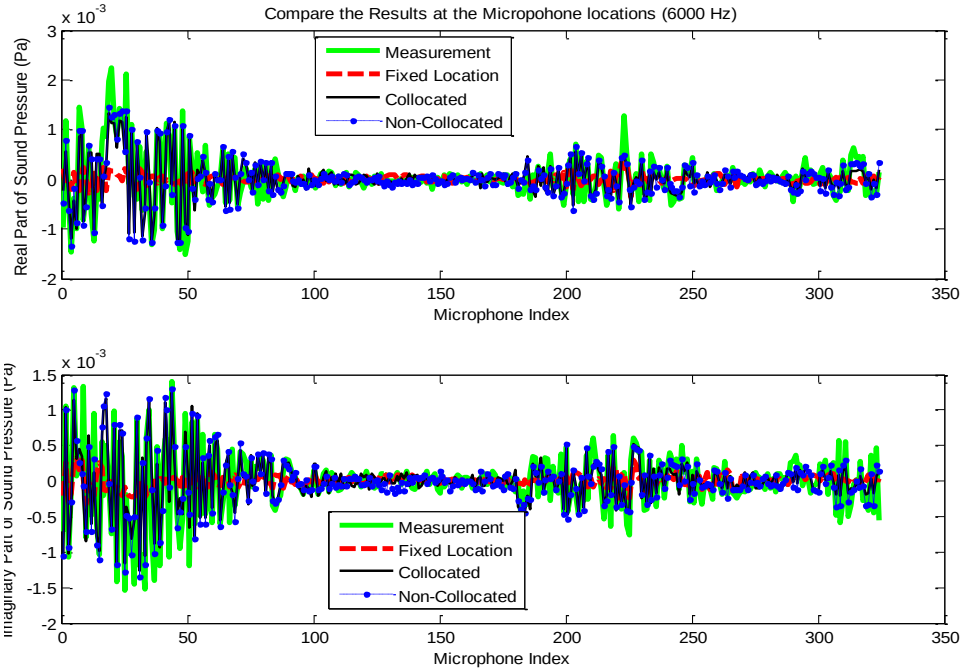

Figure 3.9. Performance comparison among ESM's with different flexibility at 6 kHz.

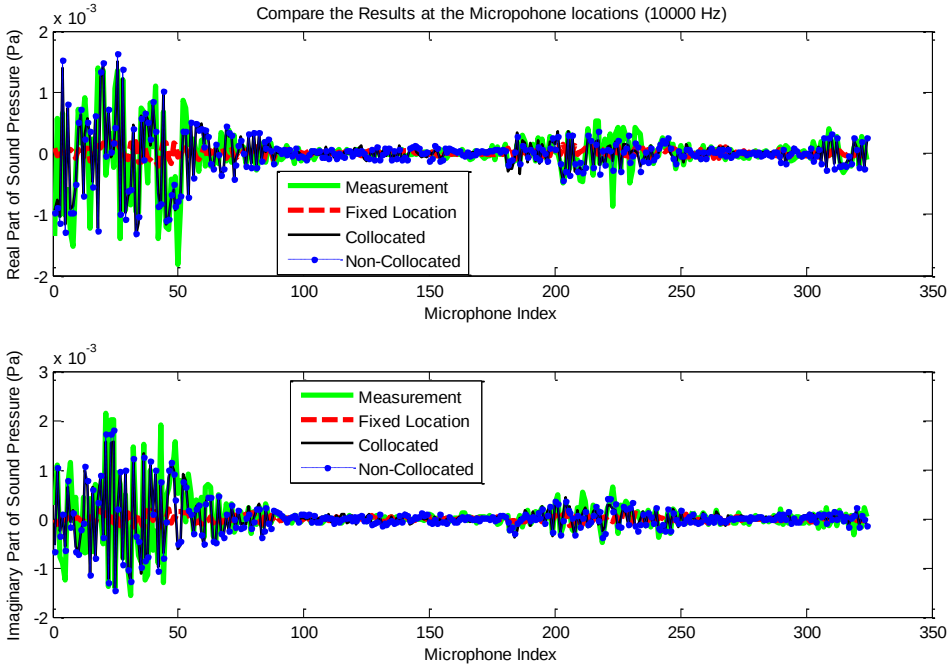

Figure 3.10. Performance comparison among ESM's with different flexibility at 10 kHz.

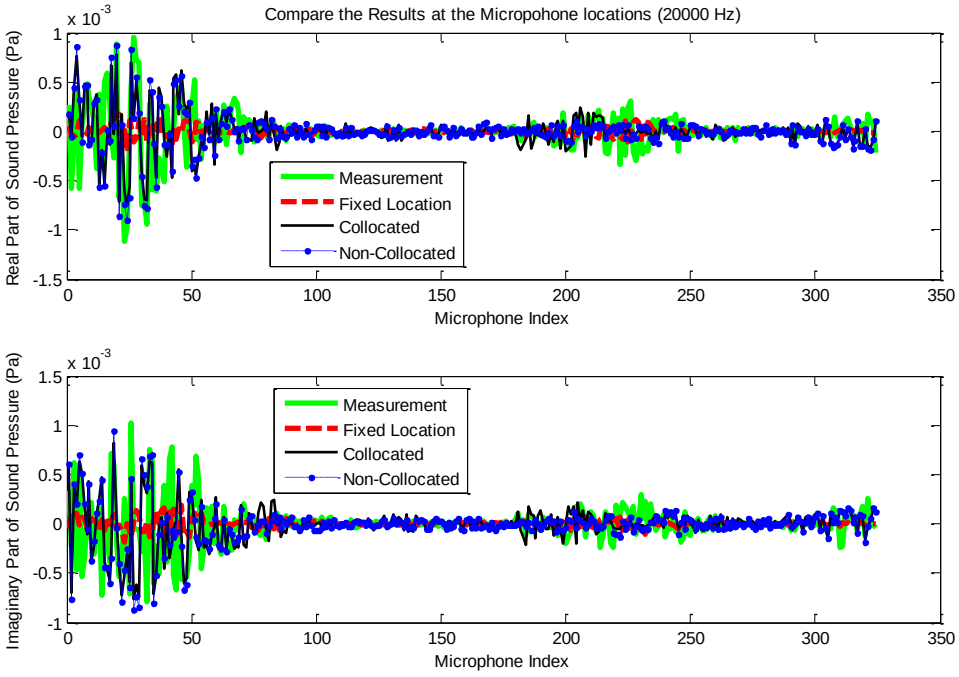

Figure 3.11. Performance comparison among ESM's with different flexibility at 20 kHz.

Since both the collocated model and the non-collocated model gave good performances for all frequencies, but the collocated model had fewer source location parameters to optimize (recall that optimizing the source locations is a non-linear process), the collocated model is preferred both from a computational intensity point-of-view and from the model efficiency point-of-view. Thus only the collocated model was used in the following further validations.

First, instead of comparing the measurement with the prediction at each microphone index in 2D plots, the 3D spatial distribution of the sound pressure levels at each microphone were also compared between the measurements and the predictions from the collocated model (Figure 3.12 to Figure 3.15). The results indicate that the model can also accurately predict the spatial pattern of sound field.

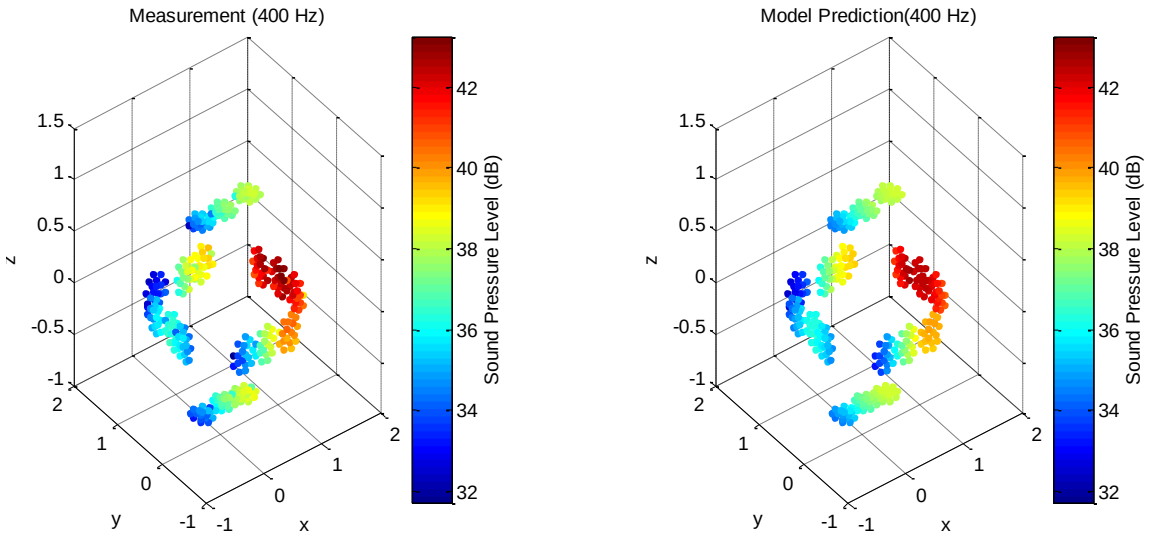

Figure 3.12. Comparison of sound pressure level spatial distribution at 400 Hz (collocated model results vs. measurement).

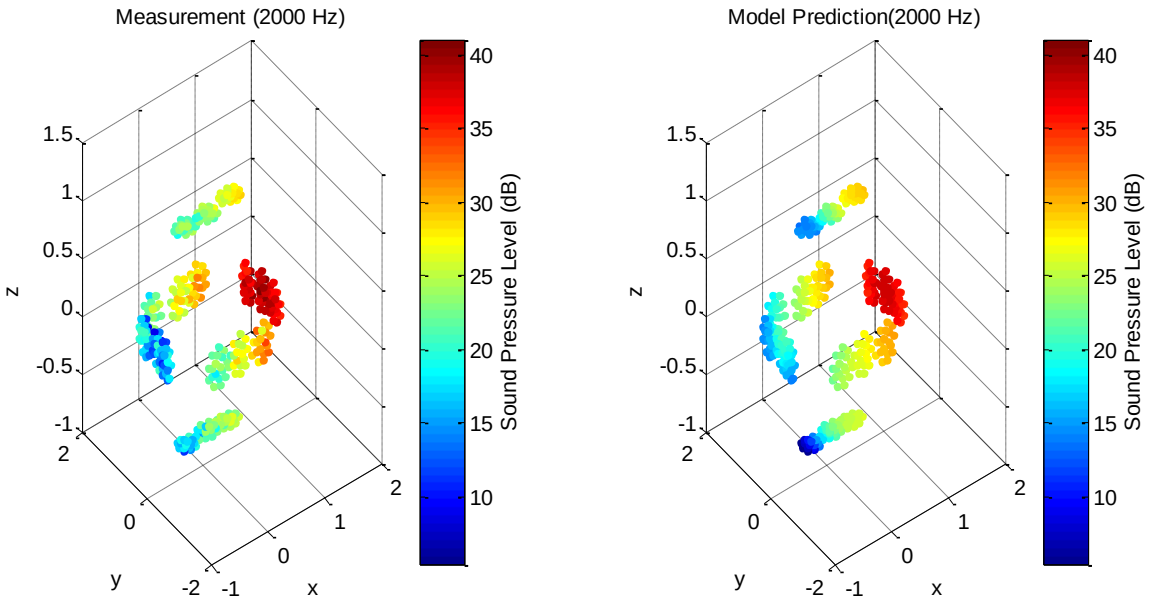

Figure 3.13. Comparison of sound pressure level spatial distribution at 2k Hz (collocated model results vs. measurement).

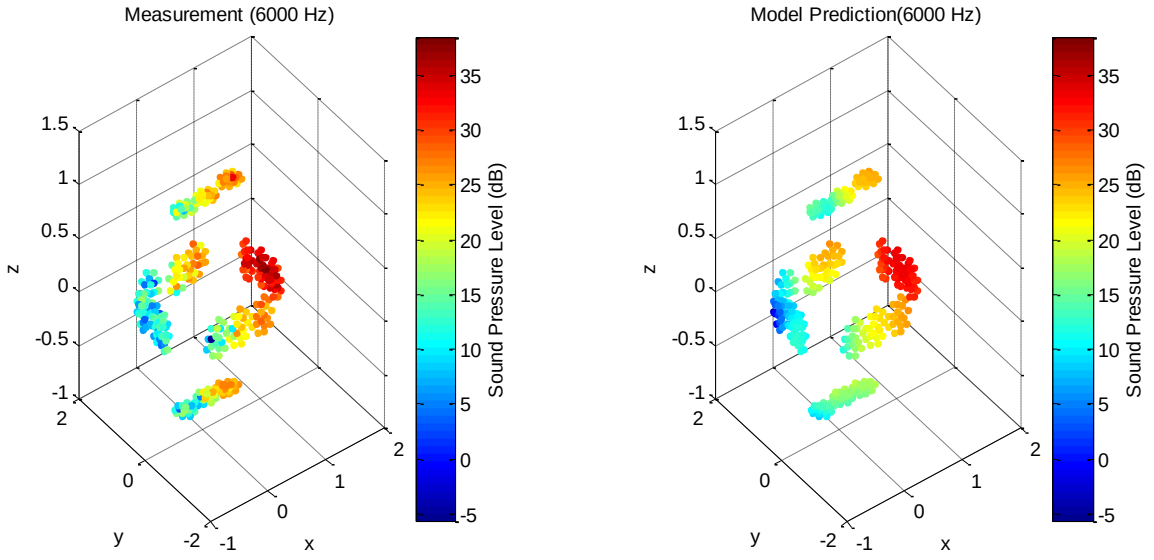

Figure 3.14. Comparison of sound pressure level spatial distribution at 6k Hz (collocated model results vs. measurement).

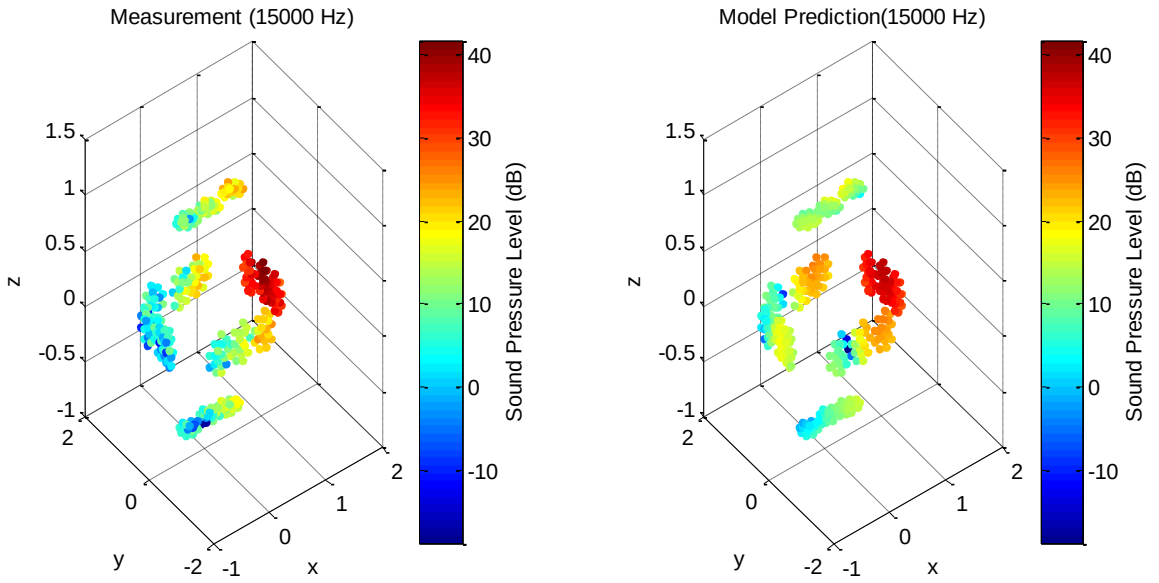

Figure 3.15. Comparison of sound pressure level spatial distribution at 15k Hz (collocated model results v.s. measurement).

Another interesting result from the collocated model is the change of the calculated source location (through the non-linear process described in Section 3.2.3) with the increase of frequency. In Figure 3.16, the relative location of the calculated source location from the collocated model to the dimension of the loudspeaker are plotted at 400 Hz, 2 kHz, 4 kHz and 6 kHz. It is observed that the source location is always close to the front face of the loudspeaker and is located close to the diaphragm center at lower frequencies (400 Hz and 2 kHz), but the source starts to move to the tweeter location of the loudspeaker for frequencies above 4 kHz. This phenomenon is consistent with the cross-over frequency at 3 kHz as listed on the specification of the loudspeaker. It is also consistent with the measured frequency responses (using a laser vibrometer with a Polytech PSV-400 scanning head and a Polytech OFV-5000 Controller) of the vibrating velocity to the loudspeaker's input signal for the diaphragm and for the tweeter, as shown in Figure 3.17 and Figure

3.18. It is noticed that the diaphragm has zero response above 3 kHz where the tweeter's velocity is large; and the tweeter has zero response below 1.5 kHz; there is, however, some small tweeter response between 1.5 kHz and 3 kHz where the diaphragm is also contributing, which, to some extent, supports the source location at 2 kHz in Figure 3.16 being in between the diaphragm and the tweeter locations.

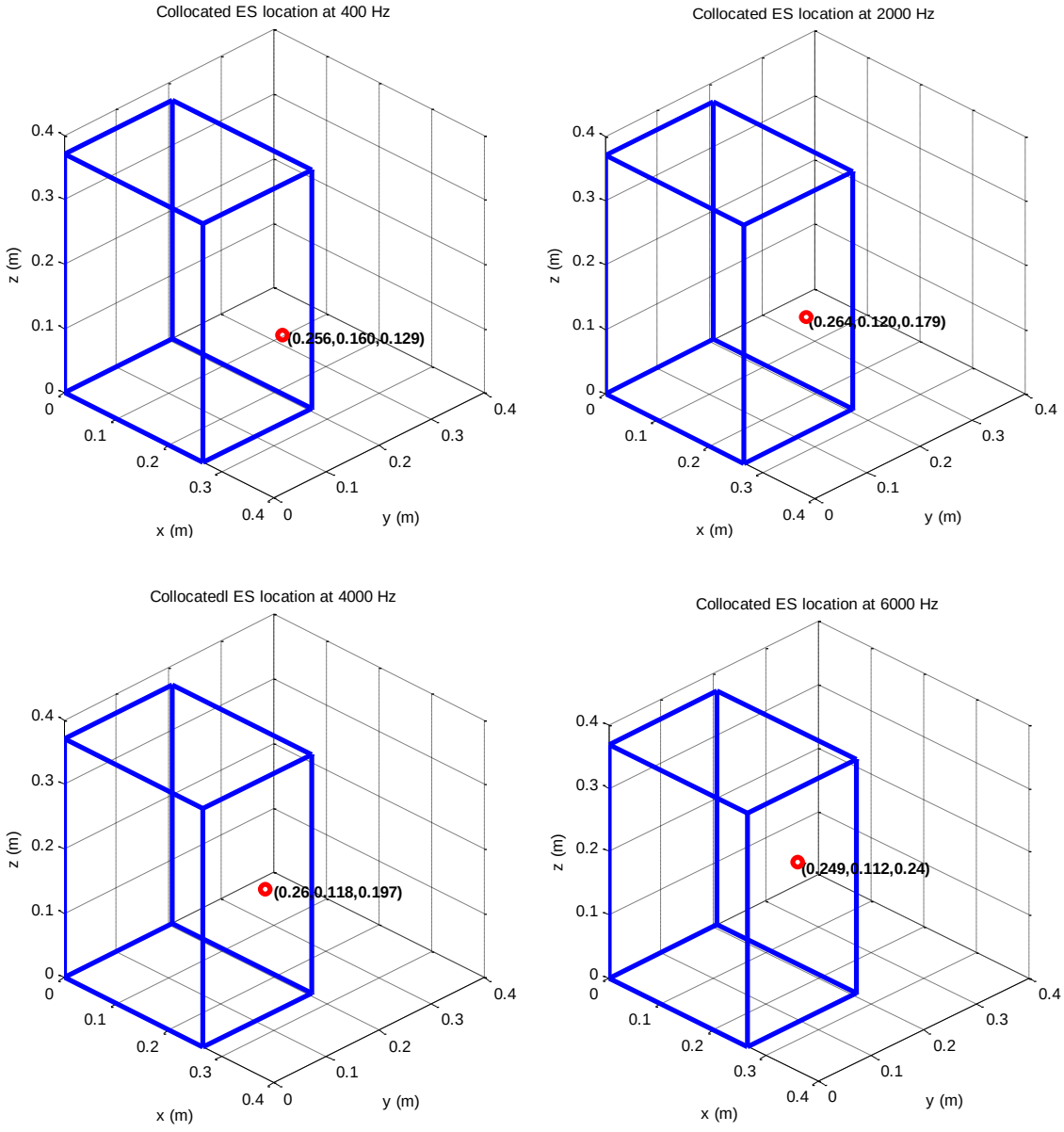

Figure 3.16. The (collocated model) calculated source locations at different frequencies.

Figure 3.17. Photos of the laser vibrometer measurement.

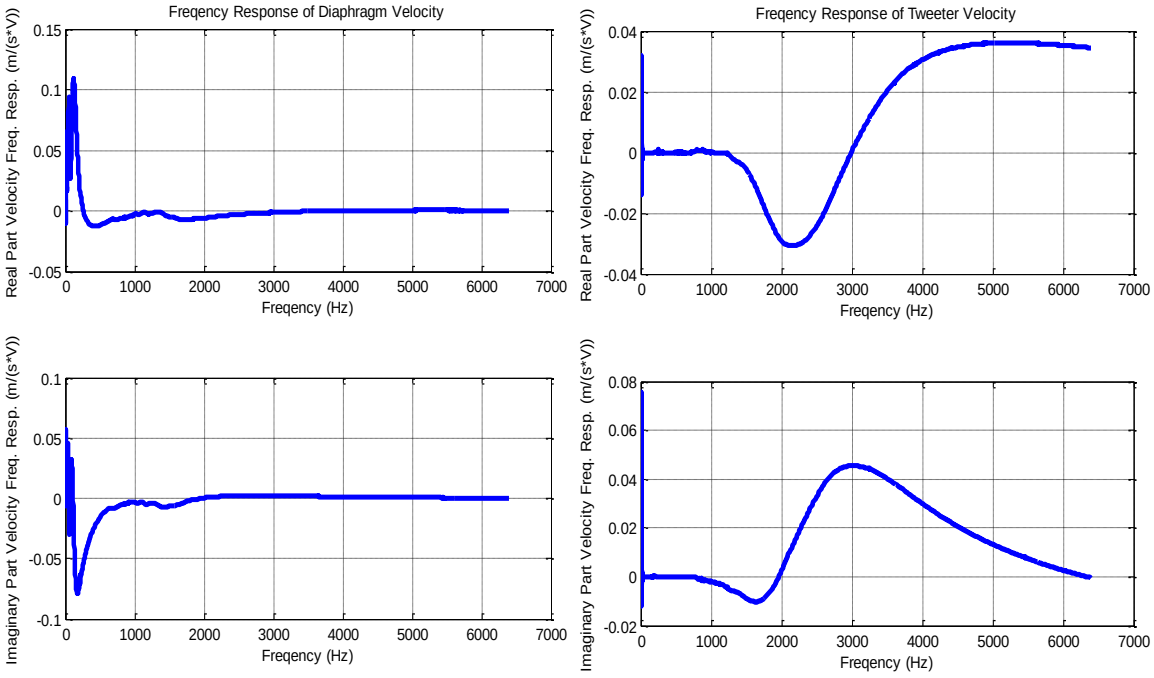

Figure 3.18. Frequency responses of the diaphragm and the tweeter velocity.

3.4.3 ESM Source and Sound Field Visualization and Comparison with BEM

To demonstrate the use of the proposed multipole ESM in visualizing the source information, here the collocated model was used to predict the sound pressure distribution on the loudspeaker surface, which was then verified by comparison with the BEM prediction of sound pressure on the same surface.

In the BEM calculations, the boundary mesh for frequencies below 2200 Hz are the same, which have more than 6 nodes per wavelength at 2200 Hz, and the mesh for higher frequencies have also satisfied the criterion of at least 6 nodes per wavelength. The boundary condition used in the BEM is a velocity boundary condition, such that the diaphragm and the tweeter are both vibrating like rigid bodies with the velocities being the measured velocities from the laser vibrometer experiment (Figure 3.17 and Figure 3.18), and the remaining areas (physically made of wood) have zero velocity (i.e., assuming the wooden surfaces are acoustically hard). The collocated ESM predicted sound pressure are compared with the BEM predictions on the loudspeaker surface (Figure 3.19 to Figure 3.21) and are compared with both the BEM predictions and the measurements at the near field and the far field measurement locations (Figure 3.22 to Figure 3.24). It is noted that the collocated model used here to compare with the BEM results was slightly difference from the collocated models used previously in Section 3.4.2: the constraint region within which the sources were allowed to move was smaller than the one used in the previous collocated models. The reason for this difference and the details in choosing the constraint region is discussed later, after the source visualization results and the performance comparison with the BEM results are commented upon. From Figure 3.22 to Figure 3.24, it is noticed that

the BEM predictions agree with the measurement and the ESM results, which validates the use of the velocity boundary condition mentioned earlier: i.e., the diaphragm and the tweeter were assumed to have rigid-body motions and the remaining surfaces were acoustically hard. Thus it is reasonable to claim the accuracy of the BEM predictions on the loudspeaker surface as well. In Figure 3.19 to Figure 3.21, the ESM predicted sound pressures are found to be in agreement with the BEM results: errors occur only in areas where the sound pressure is low and both predictions have successfully captured the location change of the pressure "hot spot" from the diaphragm to the tweeter location as the frequency is sweeping through the cross-over frequency of the loudspeaker at 3 kHz. This demonstrates that the proposed ESM can be used to accurately predict and visualize the source information.

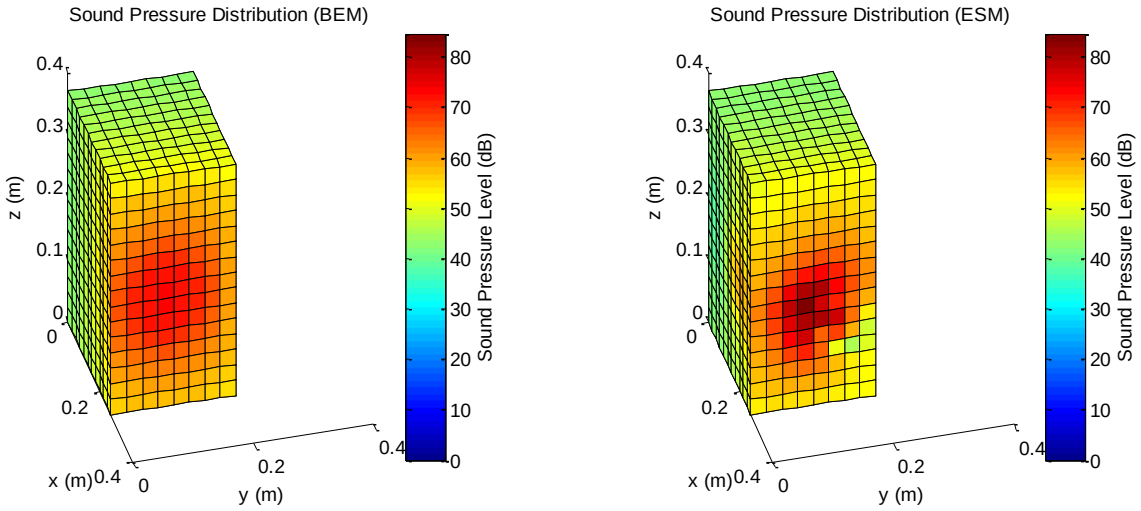

Figure 3.19. Sound pressure prediction compared on the loudspeaker surface at 400 Hz.

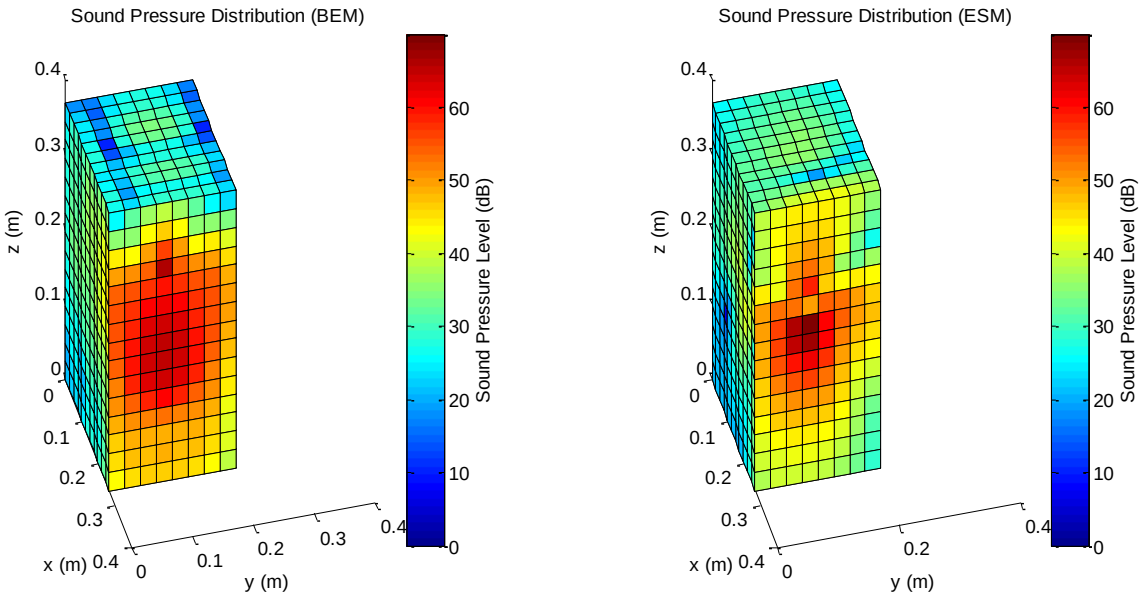

Figure 3.20. Sound pressure prediction compared on the loudspeaker surface at 2 kHz.

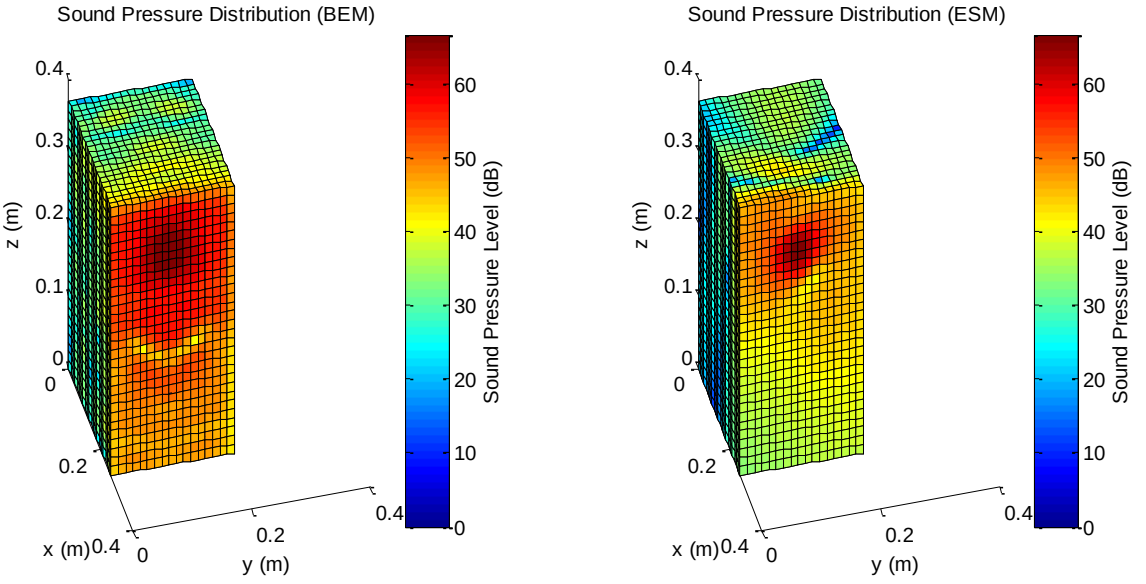

Figure 3.21. Sound pressure prediction compared on the loudspeaker surface at 4 kHz.

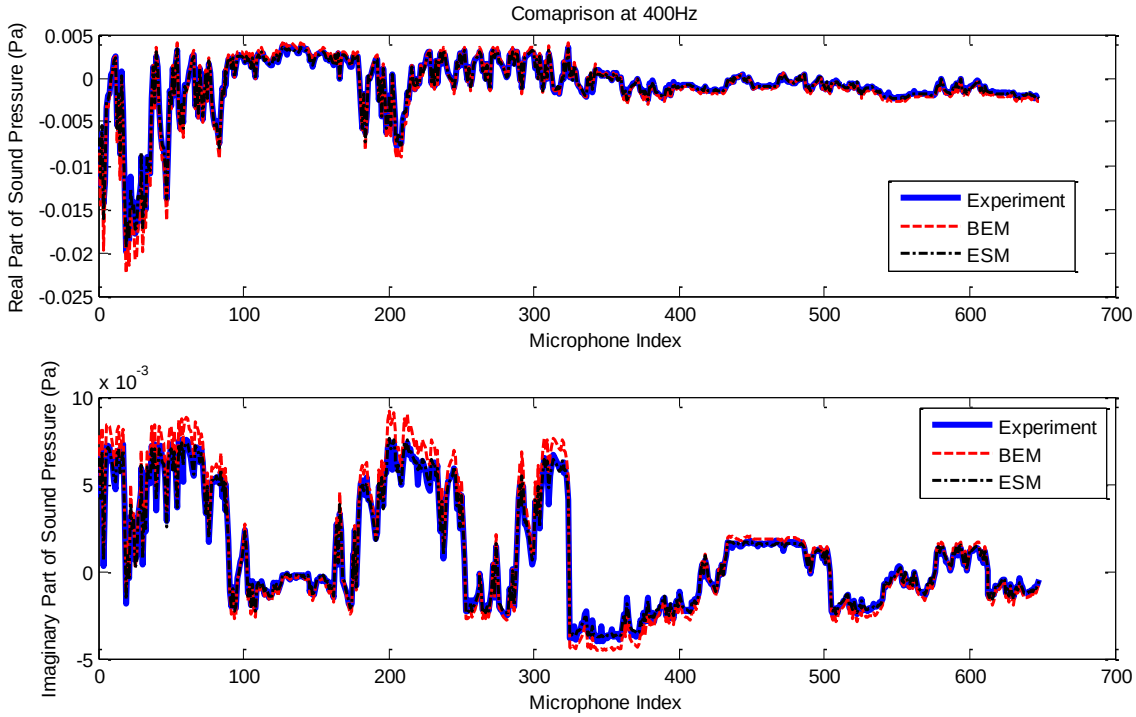

Figure 3.22. Sound pressure comparisons at the microphone locations at 400 Hz.

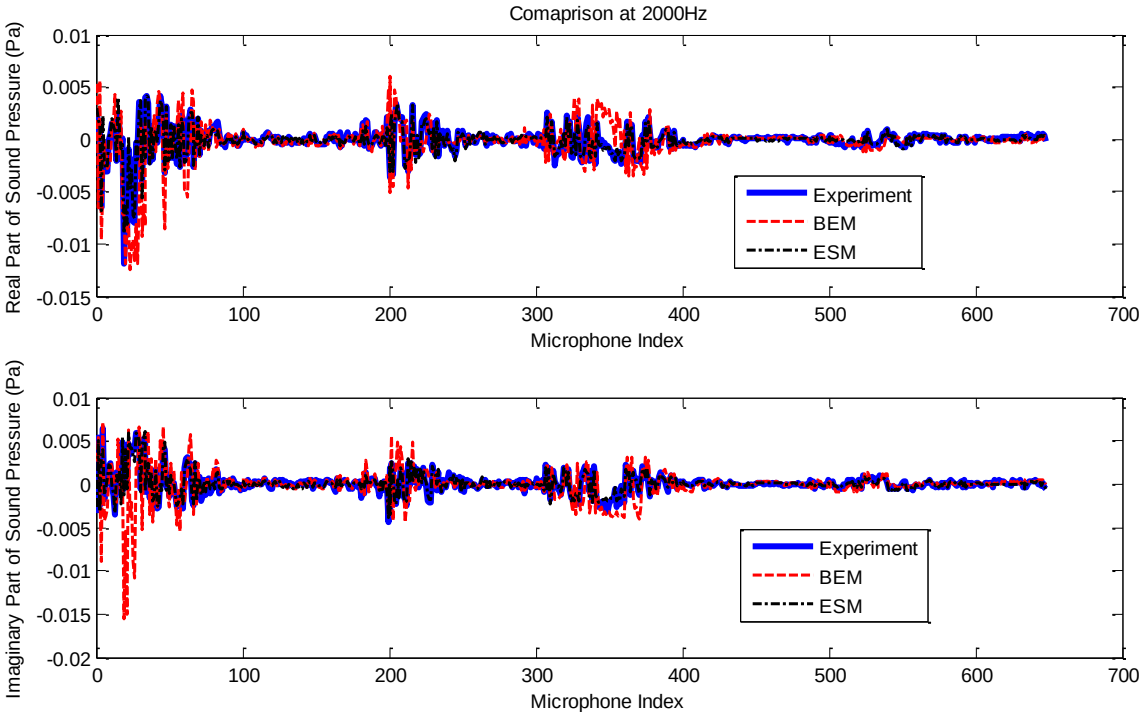

Figure 3.23. Sound pressure comparisons at the microphone locations at 2 kHz.

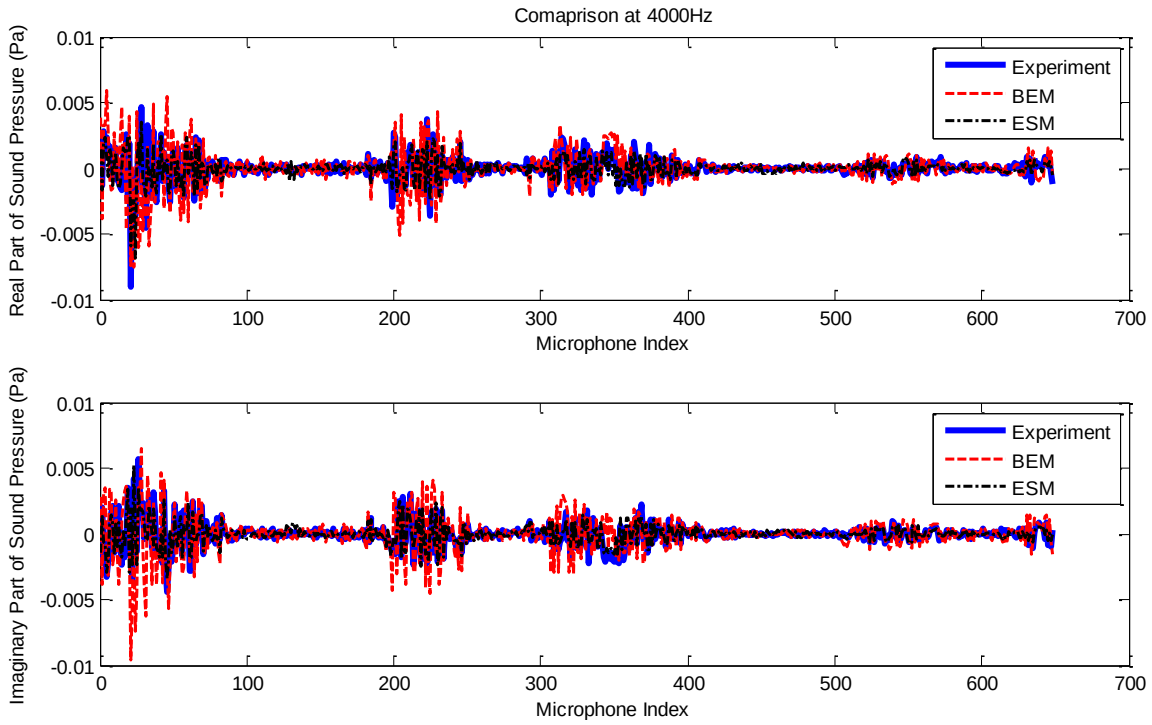

Figure 3.24. Sound pressure comparisons at the microphone locations at 4 kHz.

One more issue that needs to be discussed is the difference between the collocated ESM used here in Section 3.4.3 and the one used earlier in Section 3.4.2. This difference resulted from a problem with using the collocated model to predict the sound pressure on the loudspeaker surface: the model-estimated source locations are usually close to the front face of the loudspeaker as shown in Figure 3.16; thus, when predicting the sound pressure at the points on the front face that are close to the calculated source location, the prediction errors become large (since the sound pressure expressions have singularities at the source location). One way to circumvent this is to constrain the source location to a smaller feasible region (i.e., the region within which the sources are allow to move) such that the source is still inside the loudspeaker but its distance to the loudspeaker's front face is larger than certain value. This distance threshold should be large enough to avoid the close-to-

singularity issue when evaluating the sound pressure on the front face, but, at the same time, should be small enough so that the feasible region for the source location optimization is not too small. After trying a few distances, by gradually increasing this value and comparing with the BEM predicted sound pressure on the surface as well as the measured sound pressure at the far field measurement locations, 4 cm was found shown to be a good choice of this distance threshold. This is validated by the good agreements at all frequencies shown in Figure 3.25 to Figure 3.28, where the performance from the modified collocated ESM used here (labeled as "Collocated (-4 cm)" in the figures) and that from the previously used collocated ESM (where the feasible region for the source location is exactly the loudspeaker region).

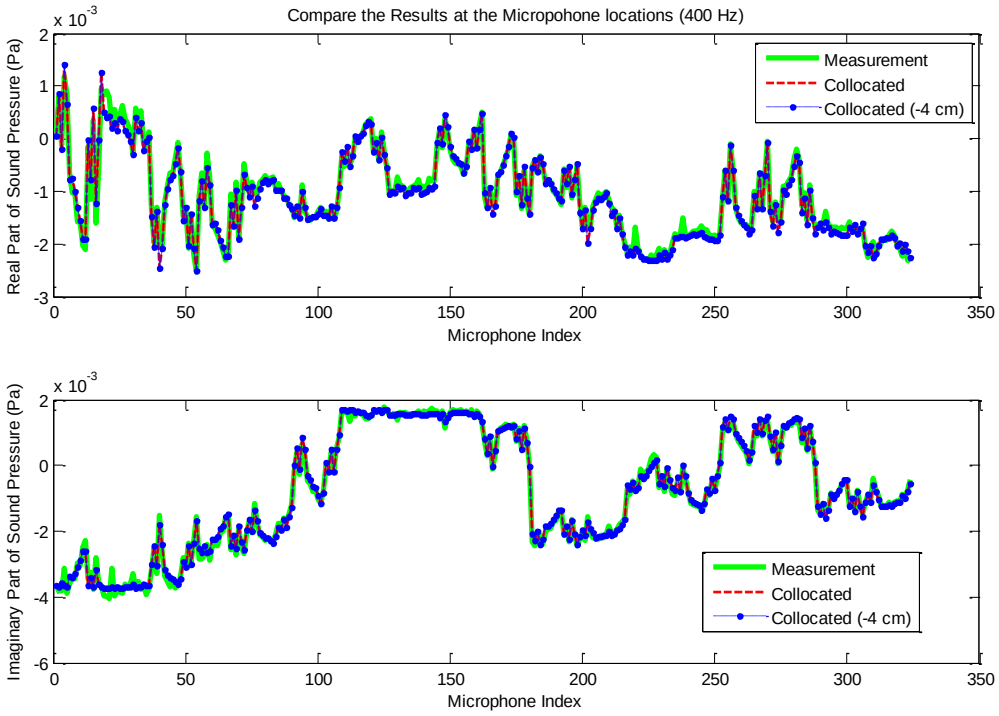

Figure 3.25. Performance comparison between two different collocated ESM at 400 Hz.

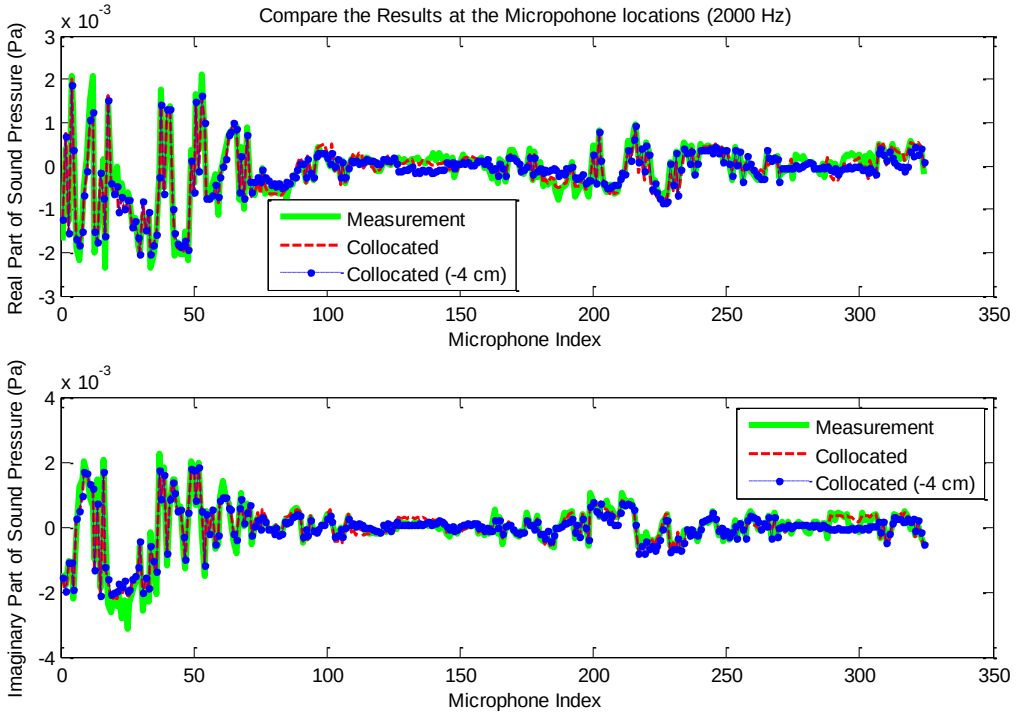

Figure 3.26. Performance comparison between two different collocated ESM at 2 kHz.

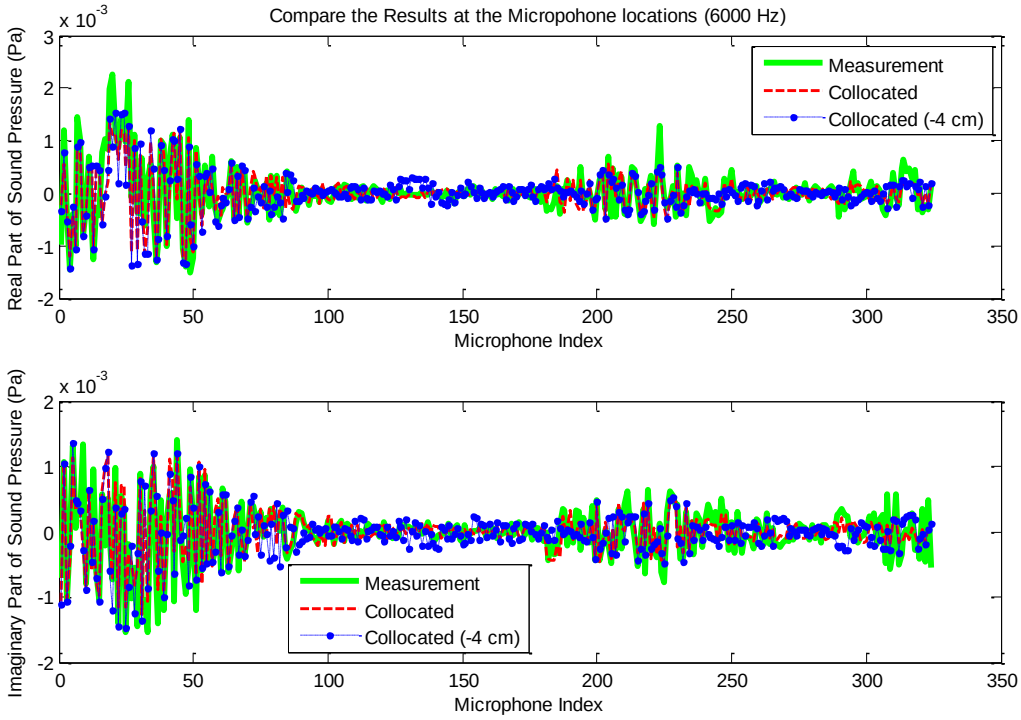

Figure 3.27. Performance comparison between two different collocated ESM at 6 kHz.

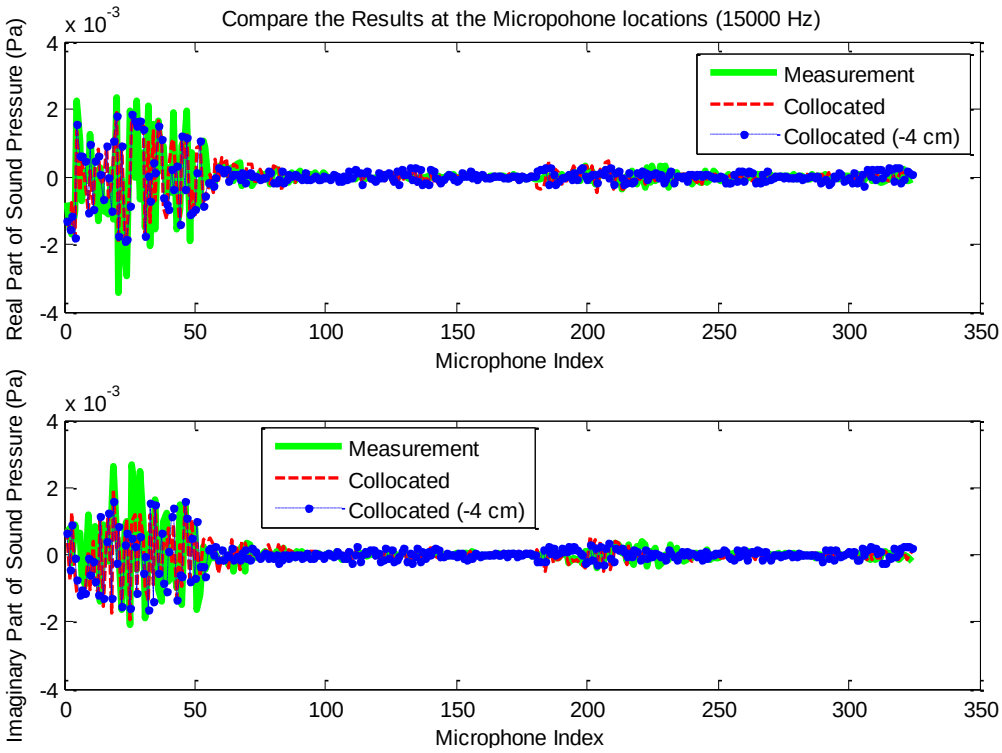

Figure 3.28. Performance comparison between two different collocated ESM at 15 kHz.

3.5 Summary

For the purpose of developing an efficient model for free-space sound field prediction, the higher order equivalent source model with un-fixed source locations was proposed as a new ESM category, which makes use of a set of higher order multipoles to approximate the actual sound field, which, in contrast with traditional methods, allows the component locations of the sources to be undetermined and allows different sources to have different locations. A nonlinear optimization approach was used to determine the source locations that achieved the least discrepancy between the measured and the model-predicted sound fields.

A measurement of the free space radiation of a loudspeaker was carried out to validate the accuracy of this model and its use in visualizing the source information. The performances of the multipole ESM's with three different degrees of flexibilities were investigated: the fixed-location model, the collocated model and the non-collocated model, in which the highest source order was chosen to be the octupoles. By comparing the model predictions with the measurements, it is shown that the fixed-locations can only accurately predict the sound field below 3 kHz, while the collocated and the non-collocated models can both have accurate predictions for the whole audible frequency range (i.e., up to 20 kHz). Since there is no large performance difference between the collocated and the non-collocated models, and the former has fewer parameters that need to be nonlinearly optimized, the collocated model is preferred in reconstructing and visualizing the sound field from sources similar to a loudspeaker. The calculated source locations, when using the collocated model, change from the physical diaphragm location to the tweeter location as the frequency sweeps through the designed cross-over frequency of loudspeaker from the low frequency region to the high frequency region, which is an indirect validation of the use of the proposed multipole ESM's in sound field reconstruction.

When calculating the sound pressure on the loudspeaker surface, in order to avoid evaluating the sound pressure at field points close to the source locations, it is necessary to constrain the sources to being inside the loudspeaker and, at the same time, constrain the distances between the sources and the front face of the loudspeaker to being larger than 4 cm (a value that could be application-dependent). After this additional constraint, the

predicted sound pressure distribution on the loudspeaker surface agrees well with the BEM predictions, and is thus considered to be accurate.

.

CHAPTER 4. REDUCED ORDER SIMULATIONS IN ROOM ACOUSCTICS USING EQUIVALENT SOURCE METHODS WITH SOURCES OF FINITE SIZES

4.1 Introduction

An efficient model has been described in Chapter 3 for simulating the free-space sound field radiation of a source, the result of which can be taken as the input to the room acoustics model developed in this chapter to accomplish the task of the prediction of the sound field in different room environments. A similar motivation (i.e., to predict the sound field using fewer model parameters) is applied here, as that which lies behind the work discussed in the previous chapter. In this chapter, a reduced order model for room acoustics is constructed. In the application concerned in the current work, the source, such as a loudspeaker, flat screen television, etc., usually has a finite geometric dimension that cannot be neglected, which is in contrast with the prediction of sound field from a musical instrument in a large concert hall. Thus the objective for this chapter is to develop a suitable room acoustics model that can be applied to sources with finite sizes and that has a relatively low model order.

It is not difficult to conclude from the review of commonly used room acoustics models in Chapter 2 that they cannot be directly implemented here, since: (1) the techniques such as the Image Source Model, the Ray Tracing Model and Hybrid Model usually require the point source assumption and the calculations involved are not derived from a rigorous

mathematical foundation (solving boundary value problem for governing equations); and (2) the simulations from models of FEM and BEM types, although they can be very accurate and can be used in the case of finite-size sources, are usually too intensive from a numerical computation point of view. Therefore new modeling alternatives need to be developed. The characteristics of the target application and the analysis of the limits of traditional room acoustics techniques have motivated the idea of developing a reduced order room acoustics model based on the Equivalent Source Models (ESMs) which was previously designed for free-space sound field prediction only.

As already mentioned in earlier chapters and it is recapped here, in a slightly different manner, the ESMs were originally developed and primarily implemented in the context of Near-field Acoustical Holography (NAH) in which the goal is to determine and visualize the source characteristics. For the purpose of NAH, it is first assumed that the total sound field is generated by a finite number of sources with unknown parameters, but whose fields satisfy the governing equation in the domain; the unknown parameters are then estimated based on matching the measured sound pressure or particle velocity at certain locations (i.e., the fields must match the boundary conditions: the Direchlet boundary condition for sound pressure and the Neumann for velocity). To apply the ESM to room acoustics, however, some modifications are necessary, since the given information in this application is usually the free-space sound field radiated by the source and the impedances of the various boundary surfaces, rather than a direct measurements of sound pressure as in NAH applications. The necessary modifications include: (1) an accounting for the room component of the total sound field (defined here as: the total sound field minus the free-

space component) which is represented by the assumed equivalent sources, as suggested by the work of Bi and Bolton (2012); (2) satisfaction of the room surface impedance boundary conditions (i.e., the Robin boundary conditions) for the room component, which are matched to estimate the source parameters; and (3) the chosen equivalent sources need to be able to represent both outgoing and incoming wave components.

In the work presented in this chapter, the general process of constructing the room acoustics ESM are presented first, which is independent of the specific type of equivalent sources that are chosen to represent the room component sound field. Then, as a preliminary numerical validation of the developed model, two different types of ESMs were constructed to simulate the sound field in a two-dimensional room with a simple circular geometry: one model makes use of a distribution of monopoles as the equivalent sources (the monopoles are placed inside the source surface and outside the room surface as well), and the other model makes use of a multipole series of monopoles, dipoles, quadrapoles, etc. to represent the room component sound field. After this two-dimensional numerical validation, a similar three-dimensional simulation is performed with a more complicated room geometry. The ESM results are compared with the BEM solutions to analyze the performance of each model under different conditions. Finally, an experiment involving a loudspeaker in a small room environment is conducted to further validate the proposed ESM models and to demonstrate the use of ESM as a reduced order modeling technique in room acoustics.

4.2 Theories on the Room Acoustics ESMS with Finite Size Source

The total sound field in a room with acoustic sources of finite sizes, e.g. a large engine in a test cell, includes three components (Bobrovntiskii, et al., 1991) (Langrenne, et al., 2007): (1) the free-space component, i.e., the sound field without the room effect; (2) the incoming component, i.e., the sound field contributed by scattering from all the passive room surfaces; and (3) the source scattering component, i.e., the contribution from the scattering of the incoming component by the extended source surfaces. For the sake of convenience in the present work, the sum of the latter two components is defined here to be the "room component". Since the source characteristics are usually known in room acoustics simulations, meaning that the free-space component is either given or can be easily calculated from the given information, the total sound field prediction is accomplished if the room component can be predicted. Therefore the following explanations will be focused on how to predict the room component using an ESM based on the known free-space source components and the impedances of the surfaces of the room. Moreover, also for the sake of computational convenience, it is assumed here that all the boundary surfaces are locally reacting.

4.2.1 Boundary Conditions on Different Surfaces

The boundary conditions for the room component sound field need to be clearly identified and made distinct from the boundary conditions for the total sound field since they are to be used to estimate the parameters of the ESM that are used to represent the room component. When the size of the source is not negligible, as in the application of this work, boundary conditions need to be found for two types of surfaces: (1) the source surface, i.e.,

the surfaces whose motion generates the sound field; and (2) the room surface, i.e., the passive interior surfaces that have no initial motion.

Under the assumption of locally reacting surfaces, the boundary conditions for the total sound field for both the source surfaces and the room surfaces can be expressed as (Langrenne, et al., 2007):

$$\begin{cases} \beta_1(x)\, p_t(x) + u_0(x) = u_{nt}(x) & x \in \Gamma_1 \\ \beta_2(x)\, p_t(x) = u_{nt}(x) & x \in \Gamma_2 \end{cases}, \tag{4.1}$$

where Γ_1 and Γ_2 denote the source and room surfaces, respectively; β_1 and β_2 are the admittances on Γ_1 and Γ_2, u_0 is the *in-vacuo* normal driving velocity, and p_t, u_{nt} are the sound pressure and the normal particle velocity of the total sound field.

When considering only the free-space component on the source surfaces, there is a similar relation between the sound pressure and normal particle velocities: i.e.,

$$\beta_1(x)\, p_f(x) + u_0(x) = u_{nf}(x) \qquad x \in \Gamma_1 . \tag{4.2}$$

In this expression, p_f and u_{nf} represent the free-space sound pressure and the normal particle velocity, respectively. Since the total sound field is simply the sum of the free-space component and the room component, according to the previous definition, we can write:

$$\begin{cases} p_t = p_f + p_r \\ u_t = u_f + u_r \end{cases}, \tag{4.3}$$

where the subscript r denotes the room component. By substituting Eqs. (4.1) and (4.2) into Eq. (4.3), the boundary conditions for the room component sound field can be derived as:

$$\begin{cases} \beta_1(x) p_r(x) - u_{nr}(x) = 0 & x \in \Gamma_1 \\ \beta_2(x) p_r(x) - u_{nr}(x) = u_{nf}(x) - \beta_2(x) p_f(x) & x \in \Gamma_2 \end{cases}. \tag{4.4}$$

Equation (4.4) then relates the room component sound pressure and particle velocity to those of the free-space component which are assumed to be known, and thus can be directly used in the ESM construction process. Also note that for a problem in which only the driving velocity of the source surfaces, u_0, is given, the free-space pressure, p_f and particle velocity u_{nf} can be found by solving a free-space forward prediction problem. There are many techniques available to perform that task: BEM, series expansion or free-space ESM, etc.

4.2.2 The Construction of the ESMs for Room Acoustics

4.2.2.1 The Room Acoustics ESM in General

The general process of constructing an Equivalent Source Model, which is the same for both free-space and room acoustics simulations, is that the sound field in a region in space,

or a certain component of the sound field in the region, is first assumed to be equivalent to the sound field generated by a number of sources of certain types (with fixed or unfixed locations), but the strength of each source (together with their source locations if assumed to be unfixed) are treated as unknown parameters of the model which are then estimated by matching the required boundary conditions of the problem. In room acoustics, as mentioned before, the room component of the total sound field is to be represented by ESM, and the boundary conditions specified in Eq. (4.4) are to be used for parameter estimation. The focus on this work will be placed on fixed-source-location ESM only, but the construction of an ESM with unfixed source locations can be performed in a similar way as in Chapter 3.

Based on the above assumptions, the sound pressure at a location in space can be related to the equivalent sources by the expression:

$$p(x) = \sum_{i=1}^{N} g_i(x, y_i) Q_i, \tag{4.5}$$

where N is the total number of equivalent sources included in the model, x is the location where the sound pressure is to be evaluated; Q_i and y_i denote the source strength and the source location of the ith assumed equivalent source, respectively; and $g_i(x, y_i)$ is the sound pressure generated by the ith source of unit strength (which is known since it depends only on the assumed type of the ith source). A similar relation can be derived for the particle velocity, which is expressed as:

$$\vec{u}(x) = \pm \frac{1}{j\omega\rho_0} \sum_{i=1}^{N} \vec{\nabla} g_i(x, y_i) Q_i, \tag{4.6}$$

where $\vec{\nabla}$ denotes the gradient, the overhead arrow denotes a vector quantity and ρ_0 is the air density. The sign at the front of the expression is chosen to be positive if the time dependence is assumed to be $e^{-j\omega t}$, and be negative if $e^{j\omega t}$, where ω is the circular frequency and t represents time.

In order to estimate the model parameters, i.e., the source strength in the present work, Eqs. (4.5) and (4.6) are evaluated at a number of sampling points on both the source surfaces and the room surfaces, which turns the boundary condition expressions in Eq. (4.4) into

$$\begin{bmatrix} B_1 A_p^{(1)} - A_{u_n}^{(1)} \\ B_2 A_p^{(2)} - A_{u_n}^{(2)} \end{bmatrix} \vec{Q} = \begin{bmatrix} 0 \\ \vec{u}_{nf} - B_2 \vec{p}_f \end{bmatrix} \tag{4.7}$$

with

$$B_1 = diag(\beta_1(x_1), \beta_1(x_2), ..., \beta_1(x_{M_1})), \qquad B_2 = diag(\beta_2(x_{M_1+1}), \beta_2(x_{M_1+2}), ..., \beta_2(x_M)),$$

$$(A_p^{(1)})_{ij} = g_j(x_i, y_j), \qquad (A_{u_n}^{(1)})_{ij} = \frac{1}{j\omega\rho_0} \partial_n g_j(x_i, y_j),$$

$$(A_p^{(2)})_{ij} = g_j(x_{M_1+i}, y_j), \qquad (A_{u_n}^{(2)})_{ij} = \frac{1}{j\omega\rho_0} \partial_n g_j(x_{M_1+i}, y_j),$$

$$\vec{u}_{nf} = [u_{nf}(x_{M_1+1}), u_{nf}(x_{M_1+2}), ..., u_{nf}(x_M)]^T, \qquad \vec{p}_f = [p_f(x_{M_1+1}), p_f(x_{M_1+2}), ..., p_f(x_M)]^T,$$

where T denotes matrix transpose, $x_1, x_2, \ldots, x_{M_1}$ are the locations of the sampling points on the source surfaces, and $x_{M_1+1}, x_{M_1+2}, \ldots, x_M$ are the samples on the room surface; $\vec{Q}$ is a vector containing the strengths of the equivalent sources; and $\vec{p}_f$ and $\vec{u}_{nf}$ are the free-space sound pressure and normal particle velocities at the room surface sampling locations. The admittance matrices, B_1 and B_2, are diagonal matrices since here the room surfaces are assumed locally reacting. If the assumption of local reaction is removed, admittance matrices having non-diagonal forms would result.

Given known source locations in the model, all the matrices in Eq. (4.7) are constants since the sampling points are chosen before the parameter estimation process. Thus the source strengths, $\vec{Q}$, can be estimated by solving a linear optimization problem in which the least square method is usually applied with associated regularization schemes (Nelson and Yoon, 2000) (Yoon and Nelson 2000). Based on this general formula, an ESM of a specific type can be constructed by substituting the corresponding formula for $g_i(x, y_i)$ into Eq. (4.5).

Aside from the model construction process, the issue of model completeness is addressed here. In principle, as mentioned in Chapter 3, it needs to be verified that the assumed equivalent sources can be used to represent any possible sound field in the region if the number of the sources and the order of the sources approaches infinity, even when the model construction process does not depend on the type of assumed sources. Two specific types of sources are used as equivalent sources in this work: distributions of monopoles and multipole series. The completeness of the multipole series is shown in the Appendix

as mentioned in the previous chapter, and the completeness of the monopole distributions is a classical property of single layer potentials (Doicu, et al., 2000).

4.2.2.2 The Room Acoustics ESM with Monopole Distributions

In the monopole distribution ESM development presented here, a layer of monopoles are assumed to be distributed outside the room surface, and another layer is placed inside the source surface, similar to the source placement in the work of Bi and Bolton (2012). The geometry of the source distributions are chosen to be conformal to their associated surfaces. Since, in this chapter, the ESM with monopole distributions is only implemented in two-dimensional rooms, the descriptions here are presented with a focus on constructing models in 2D spaces. It is noted that the 3D counterpart can be constructed in a similar process, and the necessary modifications to the 2D version are commented along with the introduction of the 2D model construction process in this section. In a two-dimensional space, the sound field of a single monopole is the Green's function of the two-dimensional Helmholtz equation with the boundary condition of out-going waves. When the time dependence is assumed to be $e^{-j\omega t}$, the specific formula for the monopole sound pressure is:

$$g(x,y) = \frac{j}{4} H_0^{(1)}(kr), \tag{4.8}$$

in which r is the distance from the source location to the sound pressure evaluation location, k is the wavenumber, and $H_0^{(1)}(\cdot)$ is the zero order Hankel function of the first kind that satisfies:

$$(\nabla^2 + k^2)g(x, y) = -\delta(x - y). \tag{4.9}$$

Note that if the time dependence is assumed to be $e^{j\omega t}$, the Hankel function of the first kind, $H_0^{(1)}(\cdot)$, in Eq. (4.8) needs to be replaced by Hankel function of the second kind, $H_0^{(2)}(\cdot)$. Also if the model is to be constructed in a 3D space, the spherical Hankel functions need to be used, i.e., replace $H_0^{(1)}(\cdot)$ by $\frac{e^{jkr}}{4\pi r}$ for the $e^{-j\omega t}$ time dependence and replace $H_0^{(2)}(\cdot)$ by $\frac{e^{-jkr}}{4\pi r}$ for the $e^{j\omega t}$ time dependence.

The monopole distribution ESM can be constructed by substituting Eq. (4.8) into the general formula, Eq. (4.7), and then applying the linear least squares method to estimate the source strengths. Usually regularizations are necessary at this stage because of the possibly ill-posed nature of the problem. In Section 4.3, the effect of the chosen regularization method will be discussed in detail.

4.2.2.3 The Room Acoustics ESM with Multipoles

It is more complicated to construct a multipole ESM to represent the room component sound field than a monopole ESM, since the sound field expressions for the multipoles used here, i.e., monopoles, dipoles, quadrupoles and so on, do not have as simple forms as the monopoles which were described in the previous chapter Section 3.2.1. Also the linear dependence relation among different multipole orders is detailed in the Appendix. Compared with the construction of the free-space multipole ESM in Chapter 3 where only

the outgoing multipoles are included, the room acoustics model described here should include a series of sources that represent the in-coming waves as well as the outgoing waves, since the room component, physically, contains both types of waves.

The sound field expression of the outgoing multipoles in 3D space was derived in detail in Chapter 3. With some simple modifications to these, the corresponding expressions can be obtained for the incoming multipoles and for 2D space. With the time dependence of $e^{-j\omega t}$, the outgoing and the incoming monopoles (zeroth order of the multipole series) in 3D space are defined respectively as:

$$P_0^{out}(x,y) = \frac{e^{jkr}}{4\pi r}, \qquad P_0^{in}(x,y) = \frac{e^{-jkr}}{4\pi r}, \tag{4.10}$$

where k is the wavenumber, and r is the distance between the source and the receiver locations. For the time dependence of $e^{j\omega t}$, the expressions of the incoming and outgoing sources need to exchanged. For 2D space, the zeroth order multipoles are defined, with time dependence of $e^{-j\omega t}$, as:

$$P_0^{out}(x,y) = \frac{j}{4} H_0^{(1)}(kr), \qquad P_0^{in}(x,y) = \frac{j}{4} H_0^{(2)}(kr), \tag{4.11}$$

in which the notations are the same as those in Eq. (4.8). Also similarly, the expressions of the incoming and outgoing sources are exchanged for the $e^{j\omega t}$ time dependence.

The n th order multipole is then defined, in the same process as in Chapter 3, as all possible n th order partial derivatives of the zeroth order multipole, P_0, with respect to the receiver

location variable, which may include differentiations in the x, y and z directions different number of times but the sum of the times differentiated in all directions is n. Mathematically, the n th order multipole includes all sources having the sound field expressions of the following form:

$$P_n = \frac{\partial^n}{\partial x^i \partial y^j \partial z^k} P_0 \quad with \quad i + j + k = n. \tag{4.12}$$

For Eq. (4.12), the same redundancy issue as discussed in Chapter 3 applies here, since the differentiation only depends on the number of times the function is differentiated in each direction rather than the sequence of the differentiation: e.g., $\partial_{xyz} = \partial_{yxz}$. Thus there are less than 3^n sources comprising a nth order multipole. Similar to Eq. (3.5), the expression to determine the number of multipoles (for both 2D and 3D space) of each order is:

$$N(n,r) = \begin{cases} 1 \quad , & n = 0 \\ C_{n+r-1}^{n}, & n > 0 \end{cases}, \tag{4.13}$$

where $N(n,r)$ denotes the number of multipoles of order n in a r-dimensional space.

In the current work, a highest source order was chosen before the construction of the ESM, and then the non-identical components of all the multipoles (both in-coming and out-going) up to that highest order were included as the equivalent sources that represent the room component sound field. To estimate the sources strengths in the model, the linear least square method was applied, as in the process of constructing the monopole distribution

ESM, together with regularization methods which will be discussed in detail in the next section.

4.3 Numerical Simulations for Model Validation and Analysis in 2D Space

As a preliminary investigation of the room acoustics ESM developed in this chapter, numerical simulations were first conducted in two-dimensional room spaces with simple room geometries. In this section, two room acoustics ESMs (i.e., the monopole distribution ESM and the multipole ESM) were constructed, validated and analyzed by using a numerical simulation of the sound field in a two-dimensional room with a circular shape and with a finite-size source. Some of the advantages of the multipole ESM, compared with the monopole distribution ESM, are illustrated by the results of this simulation.

4.3.1 Description of the Simulation Setup

The intent of the simulation is to predict the sound field in a two-dimensional room with its geometry shown in Figure 4.1 in which the outer circle, having a radius of $R_2 = 2$ m, represents the boundary surface of the room, and the concentric inner circle, having a radius of $R_1 = 0.5$ m, represents a vibrating surface, referred to as the source surface. The receivers (i.e., the field evaluation points) in this simulation are placed on two circles, with the same center as the room surface: they have radii of $r_1 = 1$ m and $r_2 = 1.5$ m respectively as shown in Figure 4.1. There were 200 receivers in total with 100 of them being on each circle. A non-uniformly distributed *in-vacuo* driving normal velocity was applied on the source surface, as shown in Figure 4.2, which drives the upper half of the

source surface at a normal velocity of 2 m/s and keeps the lower half passive. The driving velocity distribution in this simulation was identical across all the frequencies considered.

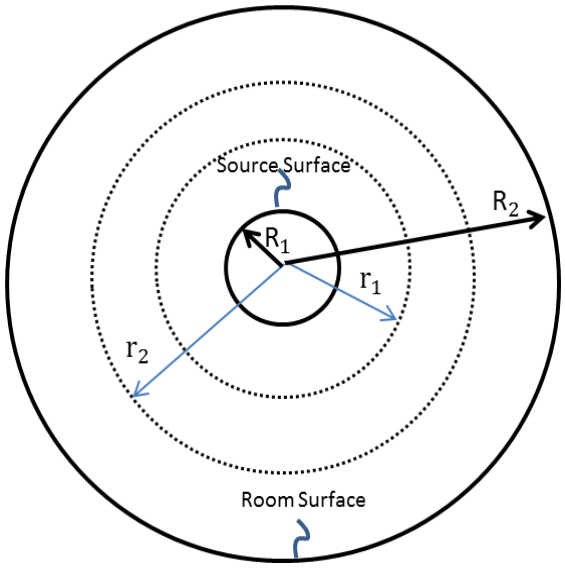

Figure 4.1. The geometry of the two-dimensional room used in the simulation.

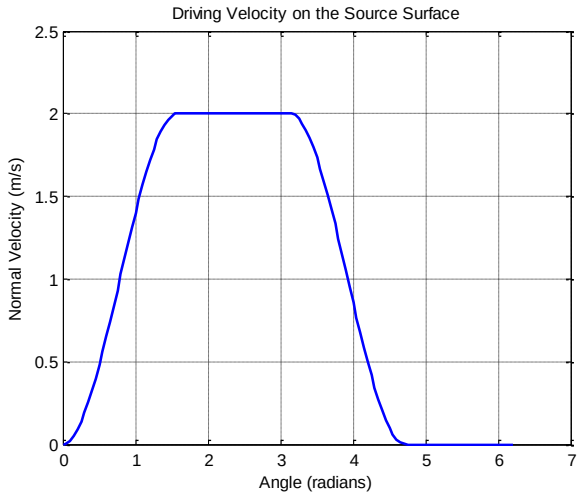

Figure 4.2. The driving normal velocity distribution on the source surface.

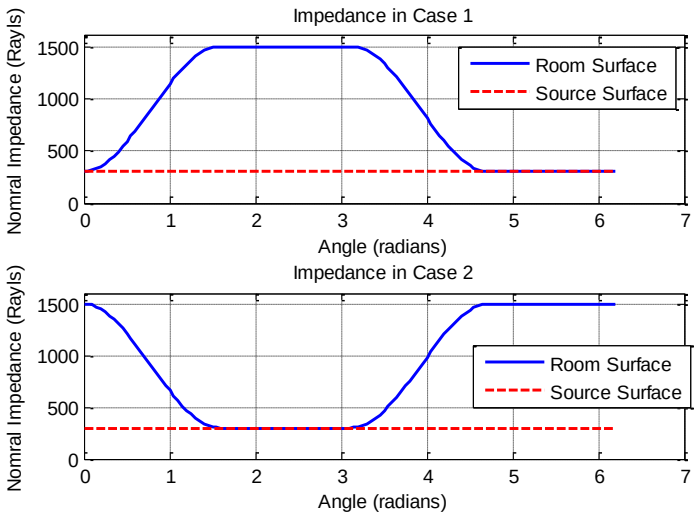

Figure 4.3. The normal impedance of different surfaces for each simulation case.

Two cases were carried out in this simulation with different room surface normal impedances but with the same source surface normal impedance. In both cases, the normal impedance on the source surface was uniformly distributed (300 Rayls), and the impedance distribution on the room surface had two different regions: a high impedance region (1500 Rayls) and a low impedance region (300 Rayls). The difference between the two cases, shown in Figure 4.3, is that in Case 1, the high impedance region is at the upper half of the room surface facing the active region of the source surface; in Case 2, the high impedance region occupies the lower half of the circle.

For the purpose of verifying the developed ESMs, a boundary element model was created for each simulation case, the results of which were used as the "true" values of the prediction in order to evaluate the prediction errors of the developed models. Monopole distribution ESMs with different numbers of assumed monopoles were implemented in

both cases, and in all these models the assumed monopoles were placed on two circles, referred to as the virtual source surfaces (the number of sources on each circle was different to maintain a similar source density on each source surface): one was outside the room surface (radius of 2.2 m) representing the inward-going wave of the room component sound field in the room region, and the other was placed inside the source surface (radius of 0.4 m) to represent the outgoing wave. To account for the impedance boundary conditions, the number of sampling points on the room surface and the source surface are chosen to be the same as the number of monopoles on the outer and inner virtual source surfaces respectively. The regularization method used in the monopole distribution ESMs was the Tikhonov method (Yoon and Nelson, 2000) in combination with the Generalized Cross Validation (GCV) method (Yoon and Nelson, 2000) to determine the regularization parameters. For the multipole ESMs, all the multipoles were placed at the origin, and models differing in the included source orders were implemented: in these cases, Truncated Singular Value Decomposition (TSVD) regularization (Yoon and Nelson, 2000) was applied. The reason for choosing different regularization techniques for different types of ESMs and their associated regularization parameters can be illustrated by the singular value distributions of the system matrices for each model type, as shown in Figure 4.4 and Figure 4.5. It can be observed from the singular value distributions (which are similar at all frequencies), that in each of the multipole ESMs, there is a sharp transition separating the singular values greater and less than one, at which point the singular values can be truncated (e.g., the 14^{th} singular value for the 3^{rd} order multipole ESM as shown in Figure 4.5). This sharp transition of the singular values resulted from the linear dependence relation among different orders of multipoles (the same reason for the singular value transition in the free-

space ESM described in Chapter 3). The proof for this linear dependence relation was provided in the Appendix, where it is shown that the number of linearly independent 2D multipoles up to certain order is the same as the number of cylindrical waves up to the same order. It is then straightforward to verify that, when including both incoming and outgoing sources, there are exactly 14 linearly independent multipoles up to source order 3. By contrast, in the monopole distribution ESMs, no such sharp transition exists (as shown in Figure 4.4) and some more general techniques, such as the GCV method, are necessary to determine the parameters of the regularization process. In the presented simulation examples of the multipole ESMs (with source order up to 3 and 6), the same number of sampling points on the boundary surfaces are used: 100 on the room surface and 30 on the source surface. For the monopole distribution ESMs, as models of different combinations of source densities on the surfaces outside the room and inside the source is to be investigated later, the number of sampling points on the room surface was chosen to be the same as the number of monopoles on the surface outside the room and similarly the number of sampling points on the source surface is the same as the number of sources on the surface inside the source.

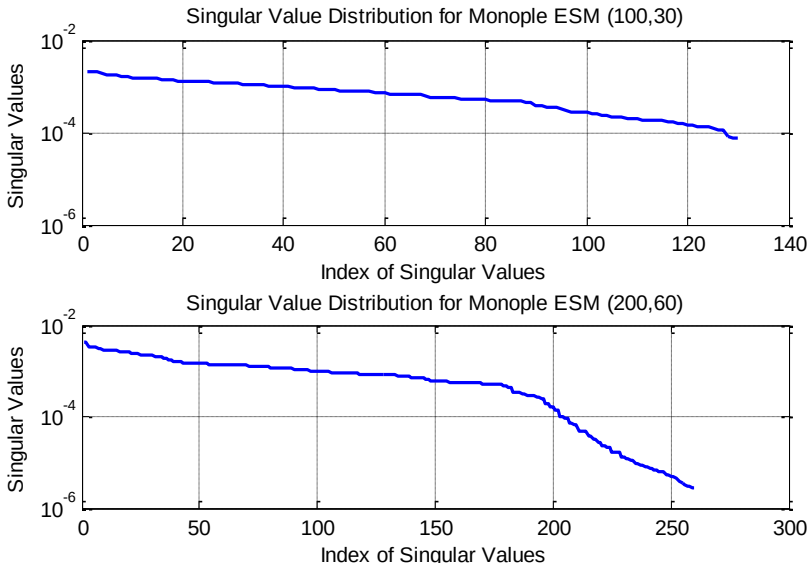

Figure 4.4. The singular value distributions for the monopole distribution ESMs (at the top: ESM with 100 monopoles outside and 30 inside; at the bottom: ESM with 200 outside and 60 inside).

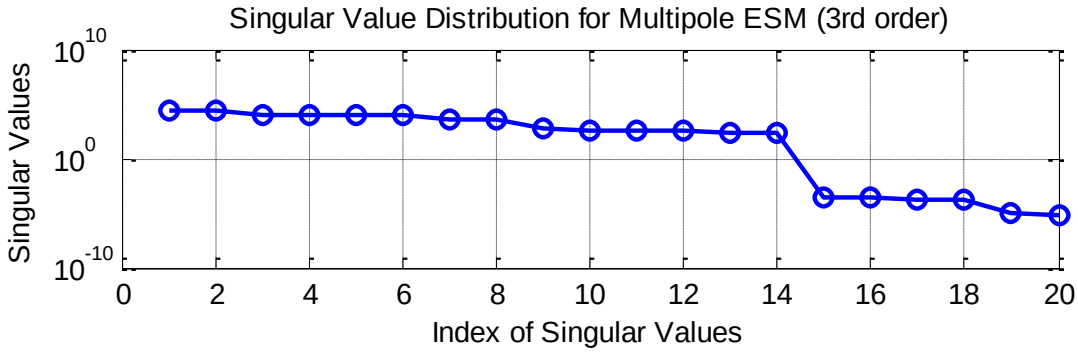

Figure 4.5. The singular value distributions for the multipole ESMs (up to the 3rd order multipole).

4.3.2 Simulation Results and Analysis

For the convenience of describing the simulation results, the two simulation cases, one with the active region of the source surface facing the higher impedance region on the room surface and the other with the active region facing the lower impedance region, are referred to as the cases 1 and 2, respectively (as illustrated in Figure 4.3). The overall prediction

accuracy for a developed ESM at a single frequency is indicated, in the present work, by the comparison of its averaged sound pressure prediction among all the receiver locations in the space, i.e., a spatially averaged performance, to that produced by the BEM model. Besides the overall prediction performance, the performance of different ESMs at individual frequencies were also investigated by comparing the predictions of developed models with that of the BEM at all the receiver locations at a single frequency component.

In the analysis of the monopole distribution ESMs, the effect of applying regularization was first investigated. It was found that no meaningful predictions could be obtained (specifically, the predictions differed from the true values by a factor of 10^n at all frequencies) if no regularization was applied to a model containing a large number of sources (more than 1000 monopoles). No figures were included here to show this, since the visual comparison between the true and the predicted sound field is not quite meaningful for such a large difference. However, when the number of sources was small, the resulting prediction could be accurate without regularization, but only at low frequencies. When regularization techniques were applied, on the other hand, the frequency region for which accurate predictions could be made expanded by adding more sources to the model. These situations are visualized in Figure 4.6 where the overall predictions of two monopole distribution ESMs are compared, one of which contains 100 monopoles on the outside virtual source surface and 30 on the inside surface (with no regularization); and the other one involves 1000 and 300 monopoles on the two virtual source surfaces, respectively (with regularization). It was observed that the model with 130 sources could be accurate at frequencies lower than 2500 Hz, while the one with 1300 monopoles could

achieve good predictions up to at least 5000 Hz. To investigate whether the reason for the failure of the first model (containing 130 monopoles) at higher frequencies was due to the lack of enough sources or due to the elimination of the regularization process, the results were compared for two models with the same source configuration but where one was regularized while the other was not: that comparison is shown in Figure 4.7, and it shows that there was no improvement in model performance by using regularization at higher frequencies. Thus it was concluded that 130 monopoles were simply not enough to describe the sound field at high frequencies in this simulation. It was also observed that the application of the regularization techniques introduced unstable predictions at some individual frequency components (possibly for frequencies where accurate results could be obtained without regularization), which can be seen in the results at lower frequencies in Figure 4.7, where the process of regularization actually enlarges the prediction error. This is due to the inappropriate choices of regularization parameters obtained by general algorithms such as GCV. However, by comparing the lower-frequency results of the model containing 1300 sources, with regularization, in Figure 4.6, and the one containing 130 source, also with regularization, in Figure 4.7, it was found that the instability introduced by the process of regularization was reduced when the number of contained sources was made large.

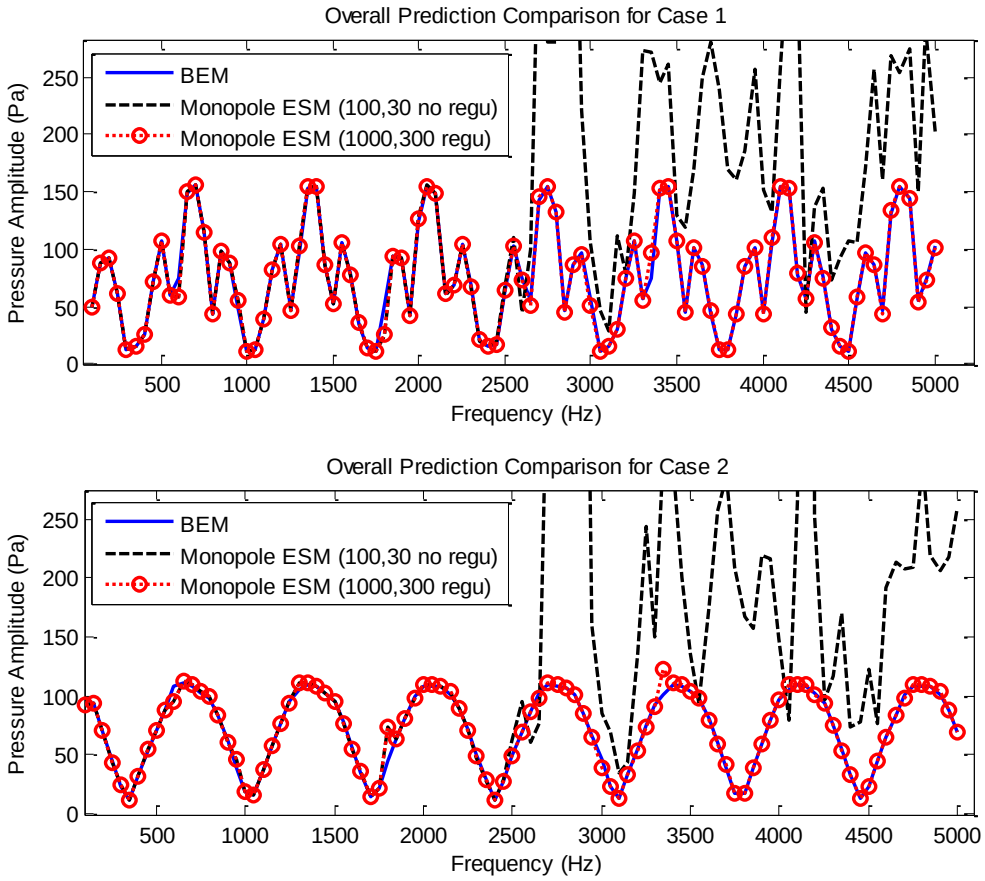

Figure 4.6. The spatially-averaged predictions of monopole distribution ESMs (solid line: result from BEM; dash line: result from ESM containing 130 monopoles, without regularization; dash line with circle: result from ESM containing 1300 monopoles with regularization).

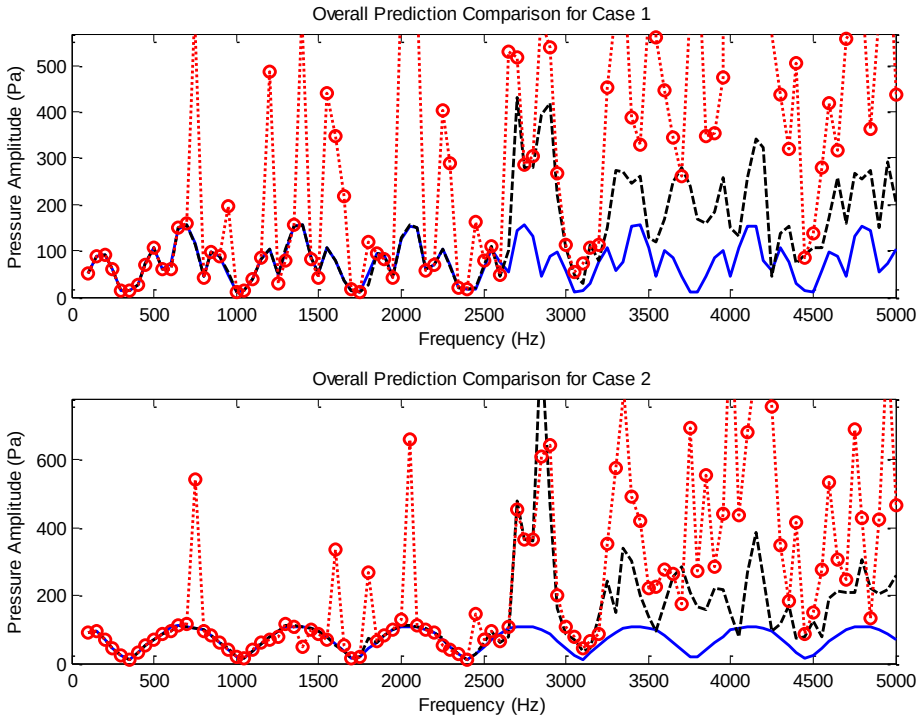

Figure 4.7. The spatially-averaged predictions of monopole distribution ESMs (solid line: result from BEM; dash line: result from ESM containing 130 monopoles, without regularization; dash line with circle: result from ESM containing 130 monopoles with regularization).

For the purpose of analyzing the model performance at various locations in the space, and to understand how the increase of the number of sources influences the model performance, the predicted sound field from models containing different numbers of sources were compared at all the receiver locations at some individual frequencies. From Figure 4.8, an increase in prediction accuracy at 2000 Hz can be seen as the number of the equivalent sources in the ESM increases from 130 to 260. A similar pattern of accuracy improvement at 4000 Hz can be observed in Figure 4.9, where the result of an ESM with 130 monopoles is not shown because its prediction was found to have a much larger error compared with the other two models. Thus it was concluded that a monopole distribution ESM with 200

monopoles on the outer virtual source surface and 60 on the inner virtual surface could accurately predict the room sound field up to at least 4000 Hz for the given geometry.

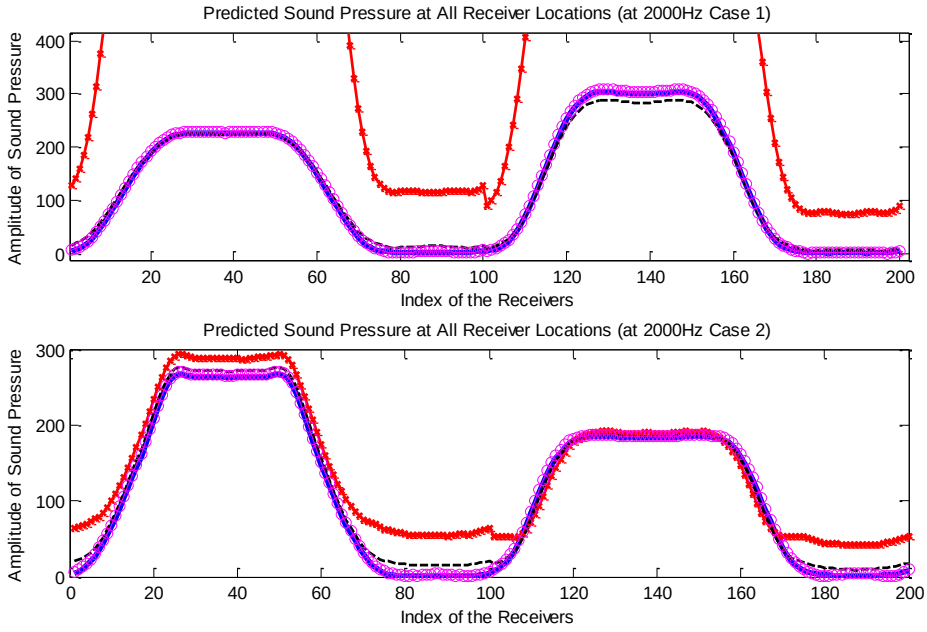

Figure 4.8. The sound pressure predictions from monopole distribution ESMs, all with regularization, including different numbers of sources at 2000 Hz (solid line: result from BEM; solid line with star: result from ESM containing 130 monopoles; dash line: result from ESM containing 195 monopoles; solid line with circle: result from ESM containing 260 monopoles).

Similar procedures were used to analyze the performances of multipole ESMs with different choices of the highest multipole order. Specifically, two multipole ESMs, one with mutipoles up to the 3rd order (octupole) and the other with sources up to the 6th order, were chosen as the analysis examples. It can be seen in Figure 4.10 that there is no distinguishable difference between these two models in the spatially-averaged sound field predictions: both agree well with the BEM result. This result, in particular, demonstrates a greater robustness of the multipole ESMs than the monopole distribution ESMs since no

instabilities introduced by the regularization were observed in the performances of the multipole ESMs. The improvement of the prediction accuracy obtained by increasing the source order in the model can be demonstrated in the comparison of the predictions from these two models at different spatial locations at single frequencies. By comparing the prediction results at 1000 Hz, 2000 Hz and 4000 Hz (shown in Figure 4.11 to Figure 4.13), it can be seen that the oscillations in the predicted results were continuously reduced as the source order was increased; and improvements similar to these examples were seen for all frequencies. The robust performance of the multipole ESM and the stable improvement by increasing the source order make it possible to flexibly balance the required computational time and the associated prediction error by choosing appropriate source orders involved in the model.

To analyze the parameter efficiency of the various ESMs used in the examples here, the number of required parameters for each model was summarized in Table 4.1. For the monopole distribution ESMs, the number of parameters was calculated as the sum of the number of monopoles placed on both the source (inside) surface and the room (outside) surface; for the multipole ESMs, it was calculated by summing up the number of independent sources for each order (using Eq. (4.13)). By investigating the number of parameters and the prediction accuracy (demonstrated previously), the conclusion is obvious that to achieve reasonable accuracy, the use of multipole ESMs requires many fewer model parameters than when using the monopole distribution ESMs: i.e., the multipole ESM appears to be more efficient than the monopole distribution ESMs.

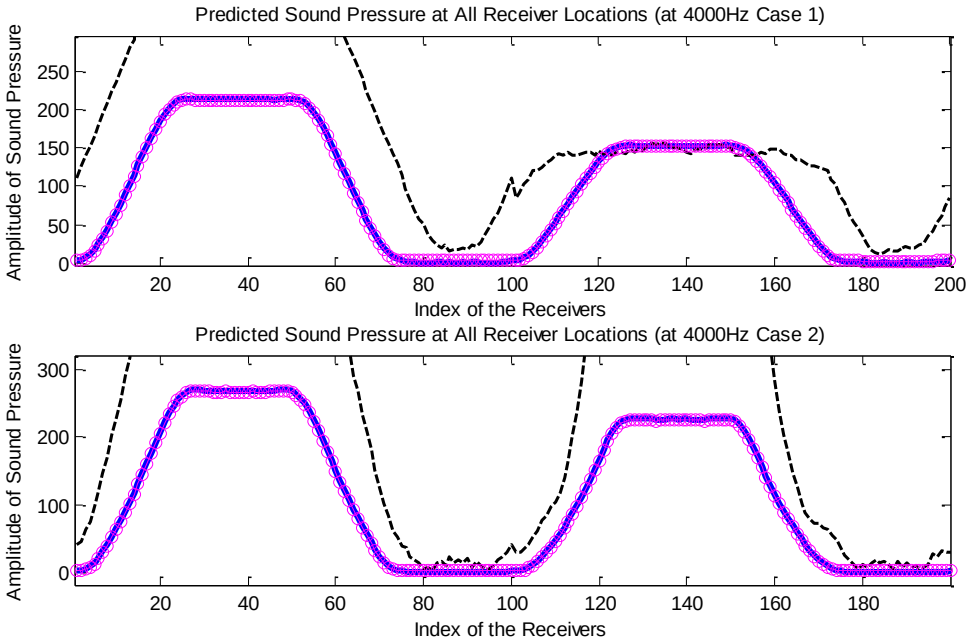

Figure 4.9. The sound pressure predictions from monopole distribution ESMs, all with regularization, including different numbers of sources at 4000 Hz (solid line: result from BEM; dash line: result from ESM containing 195 monopoles; solid line with circle: result from ESM containing 260 monopoles).

The computational times for the models that are able to provide adequate prediction accuracies are also compared to demonstrate the advantage of reducing the computational load when using ESMs. It has been shown that the monopole ESM with 260 monopoles and both multipole ESMs (with orders up to 3 and 6) can achieve relatively the same spatially averaged accuracies as the BEM. By comparing the computational times for these ESMs with that of the BEM (summarized in Table 4.2), it is clear that the ESMs requires less total computational time than the BEM. It is also noted that in the process of implementing the ESMs in the present work, the free space sound field information (treated as an input in the model construction) is computed by a free-space BEM which constitutes the most time consuming steps, and in principle, the ESMs would require even less time if

other schemes, such as series expansion or free-space ESM, were used to calculate the free-space information.

Table 4.1. The required model parameters for the ESMs presented in the simulations.

Type of ESM	Number of Parameters
Multipole ESM (order up to 3)	10
Multipole ESM (order up to 6)	28
Monopole ESM (outside: 100; inside: 30)	130
Monopole ESM (outside: 150; inside: 45)	195
Monopole ESM (outside: 200; inside: 60)	260
Monopole ESM (outside: 1000; inside: 300)	1300

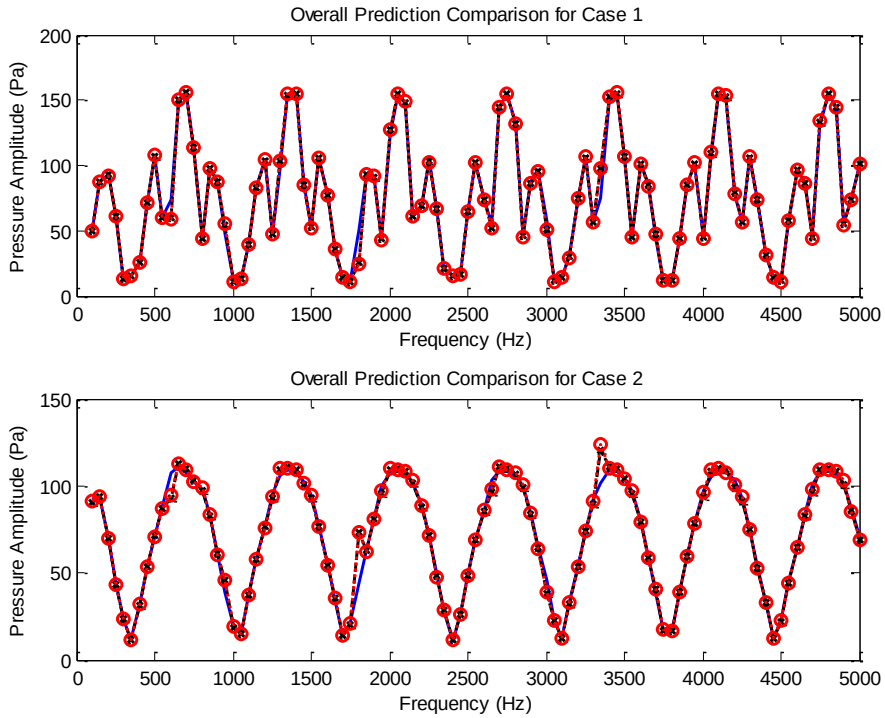

Figure 4.10. The spatial averaged predictions of multipole ESMs (solid line: result from BEM; dash line with star: result from ESM with multipole order up to 3; dash line with circle: result from ESM with multipole order up to 6).

Table 4.2. The computational time for each model yielding acceptable accuracy (unit: sec).

Frequency		200 Hz	500 Hz	1000 Hz	2000 Hz	4000 Hz
BEM	Total	7.72	16.80	45.74	138.12	475.49
Monopole ESM (260)	Free space pressure at sampling points	2.60	2.43	4.83	11.87	33.15
	Free space velocity at sampling points	10.41	10.17	20.37	48.94	131.07
	Free space pressure at receivers	2.63	2.47	4.97	12.00	32.11
	Room acoustics prediction	0.42	0.33	0.30	0.29	0.26
	Total	16.06	15.40	30.48	73.09	196.61
Multipole ESM (max order: 3)	Free space pressure at sampling points	1.48	1.43	3.12	7.99	25.23
	Free space velocity at sampling points	6.07	5.66	12.12	32.92	98.25
	Free space pressure at receivers	2.59	2.44	4.90	11.75	31.60
	Room acoustics prediction	0.38	0.19	0.18	0.19	0.20
	Total	10.52	9.72	20.31	52.85	155.29
Multipole ESM (max order: 6)	Free space pressure at sampling points	1.45	1.37	2.93	8.08	24.32
	Free space velocity at sampling points	5.96	5.66	12.16	32.46	97.69
	Free space pressure at receivers	2.61	2.46	4.92	11.94	32.06
	Room acoustics prediction	3.00	2.79	2.55	2.42	2.39
	Total	13.01	12.28	22.56	54.90	156.46

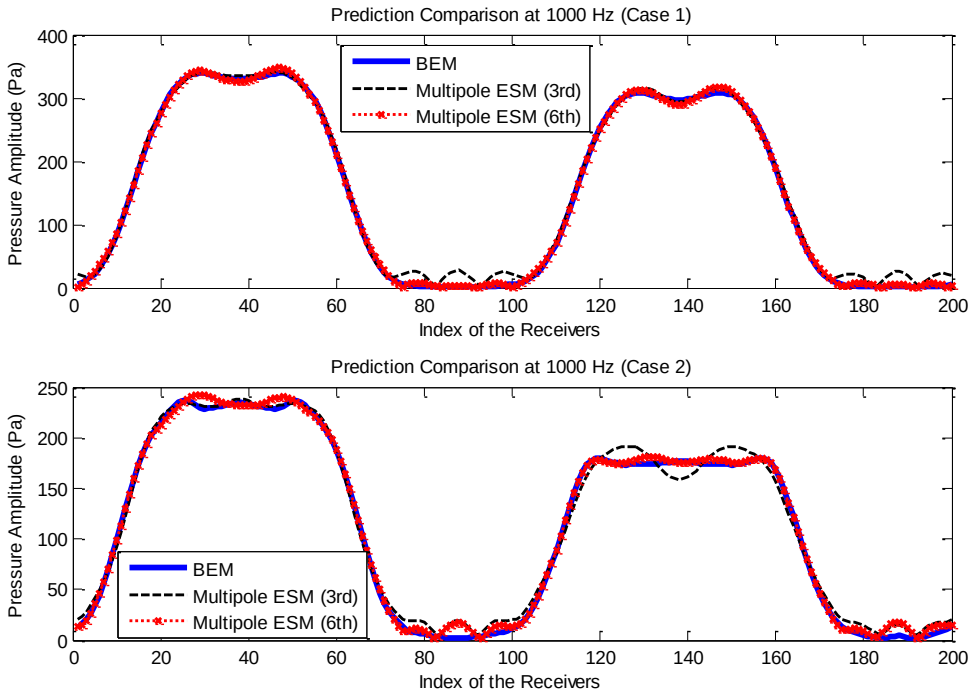

Figure 4.11. The predictions from the multipole ESMs at 1000 Hz (solid line: result from BEM; dash line: result from ESM with multipole order up to 3; dash line with star: result from ESM with multipole order up to 6).

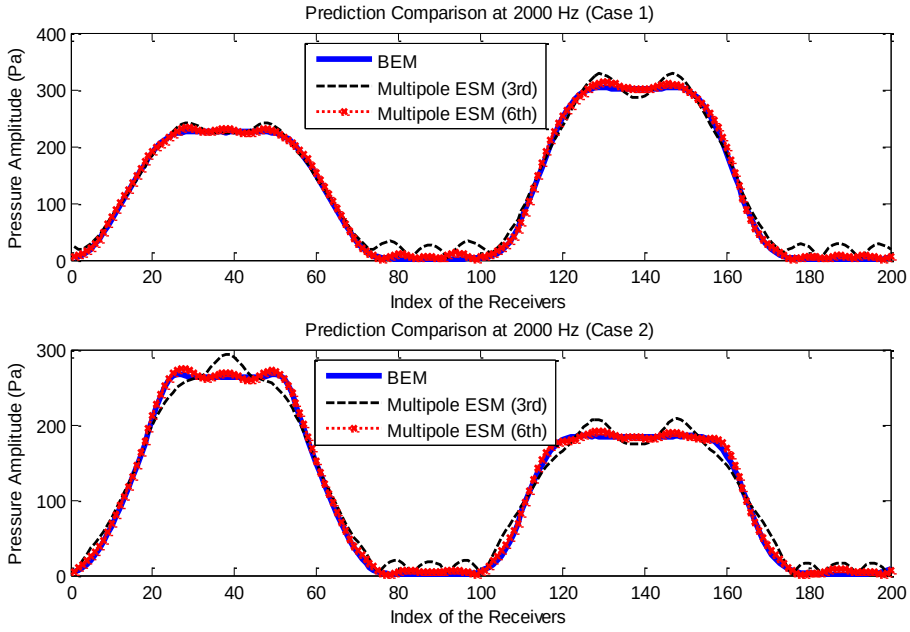

Figure 4.12. The predictions from the multipole ESM at 2000 Hz (solid line: result from BEM; dash line: result from ESM with multipole order up to 3; dash line with star: result from ESM with multipole order up to 6).

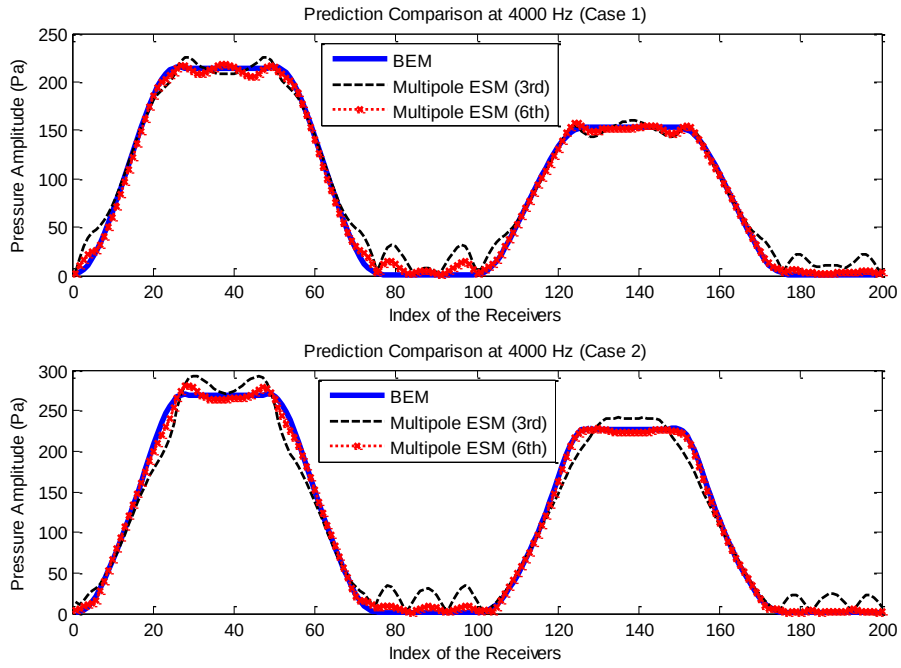

Figure 4.13. The predictions from the multipole ESM at 4000 Hz (solid line: result from BEM; dash line: result from ESM with multipole order up to 3; dash line with star: result from ESM with multipole order up to 6).

4.4 Numerical Simulations in 3D Space

In order to further validate the use of the room acoustics equivalent source model in the simulation of the sound field in a 3D room with an irregular geometry and with a source of finite size, numerical simulations were conducted, at different frequencies, to compare the prediction from the room acoustics ESM and the result calculated by the boundary element method (treated as the true sound field in this simulation).

4.4.1 Description of the Numerical Simulations

An Alpha Cabin (Chappuis, 1993) was used as the room geometry in the simulation. The source involved is a sphere located at the center of the room with part of it driven by a given *in-vacuo* normal velocity. The purpose of using an Alpha Cabin in the simulation was only to demonstrate the capability of using the room acoustics ESM for irregular room geometries. The original purpose of the Alpha Cabin, i.e., to measure the acoustics absorption of a material sample, is not focused on here. Three layers of receivers are placed in the room at different heights, at which the predictions from BEM and the ESM are compared. An illustration of the geometric configurations of the room, the source and the receivers is presented in Figure 4.14. More specifically, the room surface consists of six planes and a conical surface. In terms of the coordinates, the list here keeps three decimal places with the unit of meter, the four vertices of the bottom plane (in counter-clock-wise order viewing from the top) are located at (0, 0 ,0), (2.200, 0, 0), (2.550, 1.690, 0) and (-0.350, 1690, 0); similarly, the four vertices' coordinates of the top plane are: (-0.050, -0.050, 1.200), (2.250, -0.050, 1.200), (2.649, 1.790, 1.550) and (-0.449, 1.790, 1.550); the vertex of the cone is at (1.093, 0.838, 0.800) and the angle between the revolution side and the center axis of the cone is 49.22 degree. The radius of the spherical source surface is 0.3 m, and its center is located on the center axis of the cone, but the z-coordinate is 0.4 m. Each layer of the receivers are in the $x-y$ plane, spanning from 0.1 to 2.1 m in the x-direction and from 0.15 to 1.55 m in the y-direction, the spacing interval for each plane is 0.2 m in both x and y directions. The three layers of receivers are at the heights of 0.05, 0.4 and 0.75 m respectively, and the points inside the source surface are removed from this grid.

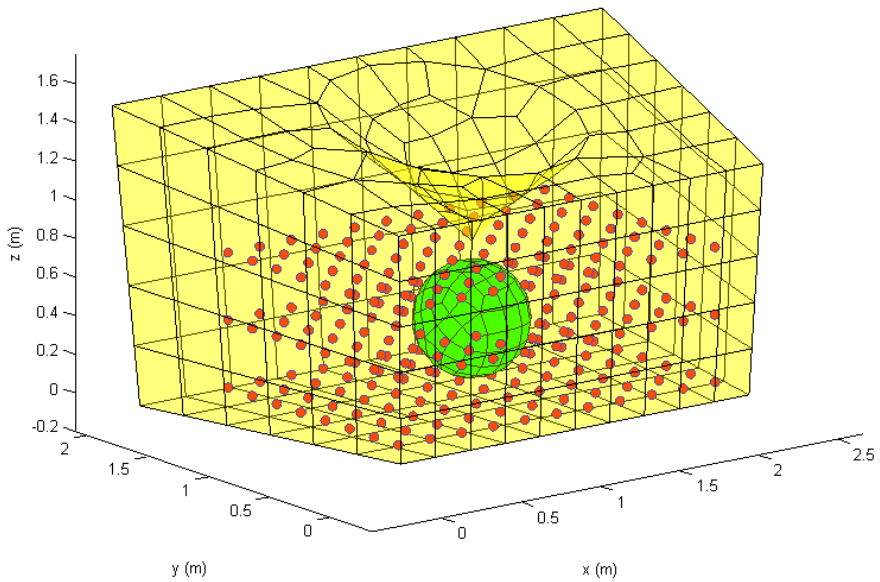

Figure 4.14. The geometries of the room surface (yellow), the source surface (green) and the receiver locations (red dots).

The *in-vacuo* normal velocity of the source surface is defined as:

$$u_0(\theta) = \begin{cases} \cos^2(2\theta) & \theta \le \pi/4 \\ 0 & \text{else} \end{cases}, \tag{4.14}$$

where θ is the angle between the radial vector of the point on the sphere and the x-axis. This means that the part of the source surface facing in the positive x-direction is driven by a normal velocity distribution which decays to zero as the angle θ increases to $\pi/4$, and the rest of the sphere is passive. The impedance of the source surface is a real constant of 900 Rayls, and the impedance of the room surface is also uniform and real and was calculated by assuming a constant absorption coefficient of $\alpha = 0.5$: i.e.,

$$Z = \rho_0 c \frac{1+\sqrt{1-\alpha}}{1-\sqrt{1-\alpha}}, \tag{4.15}$$

where ρ_0 and c denote the air density and the sound speed, respectively.

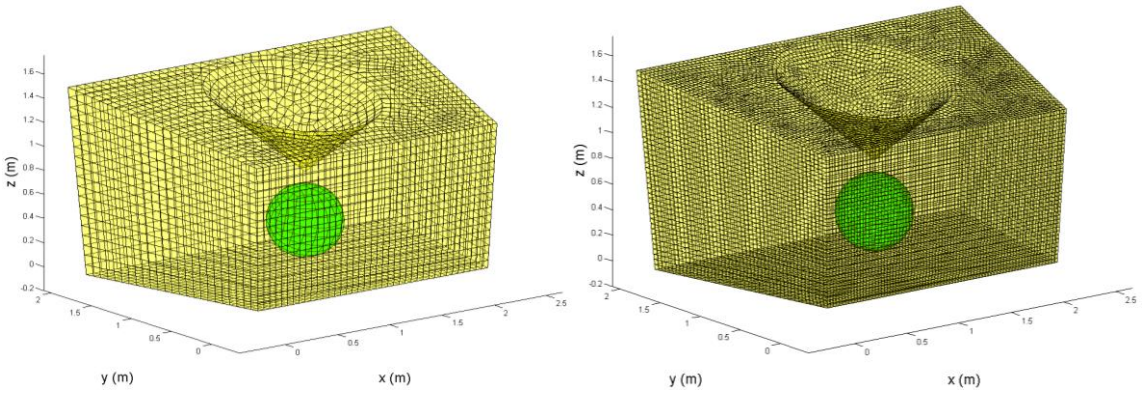

Figure 4.15. The meshes used in BEM calculations: the mesh on the left is for 125 Hz, 250 Hz and 500 Hz; the mesh on the right is for 1000 Hz.

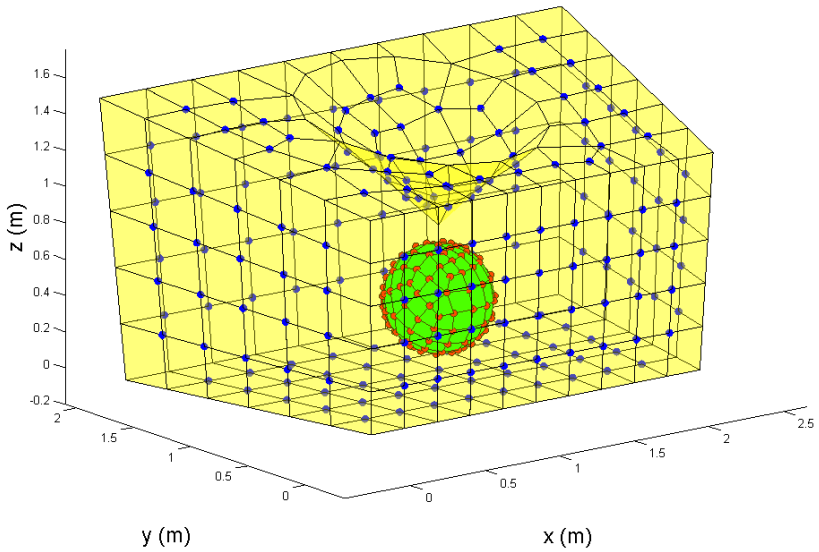

Figure 4.16. The sampling points used in the ESM simulations: the blue dots are samples on the room surface and the red dots are on the source surface.

The predictions of the sound field at the receivers from the room acoustics ESM are compared, at different frequencies, with the results obtained by BEM calculations. The OpenBEM (Henriquez and Juhl, 2010) Matlab package was used to perform the BEM calculations, and the meshes of the surfaces used in the BEM simulations were generated by Abaqus 6.14-1. Simulations were conducted at four different frequencies: 125 Hz, 250 Hz, 500 Hz and 1000 Hz. Two meshes were used in the BEM calculations: for frequencies from 125 to 500 Hz, a mesh with at least 8 nodes per wavelength at 500 Hz was used (4492 nodes on the room surface and 223 nodes on the sources surface); while for the 1000 Hz simulation, the mesh contained 8 nodes per wavelength at 1000 Hz (18367 nodes on the room surface and 903 nodes on the sources surface). The sampling points used in the ESM were the same for all frequencies with the nodes taken from a mesh with an inter-nodal distance of 0.1 m (124 nodes) on the source surface and 0.3 m (208 nodes) on the room surface, with the points on the edges and corners excluded. The two meshes and the locations of the sampling points are shown in Figure 4.15 and Figure 4.16. In the ESM simulations, the maximum multipole order (same for outgoing and incoming sources) was chosen to be 4 for frequencies of 125 Hz, 250 Hz and 500Hz; and it was chosen to be 6 for the 1000 Hz prediction. Due the limitation of the computing power of a personal computer, it was impossible to perform BEM simulations at higher frequencies for this problem.

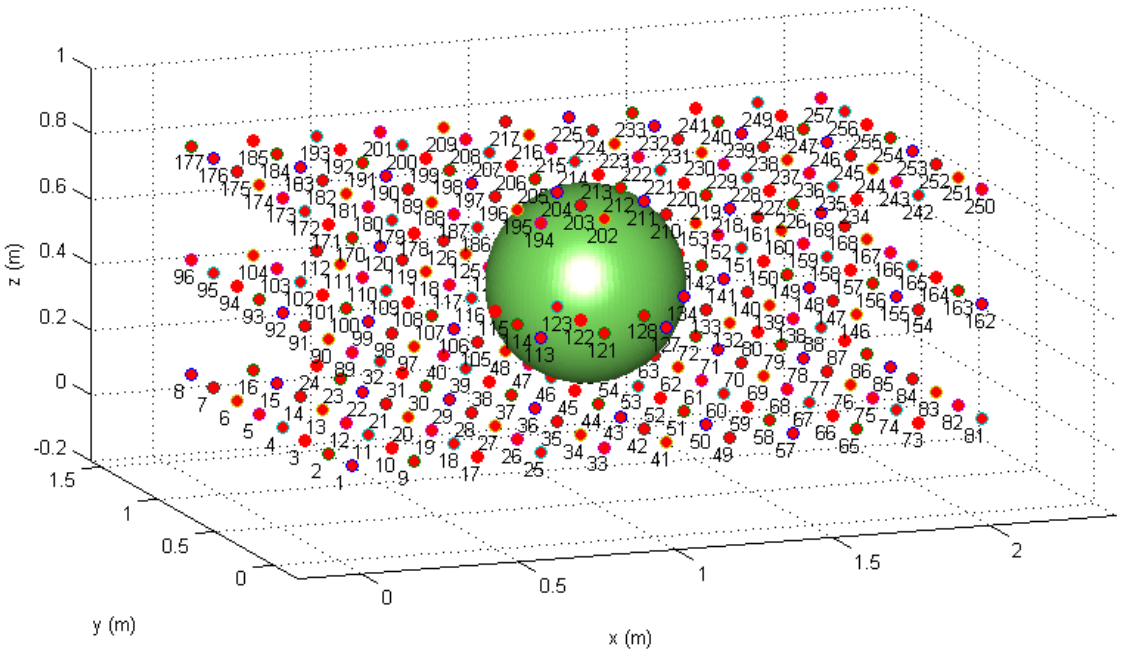

Figure 4.17. The lcations of the recerivers: the numbers are the receiver indices and the green sphere represents the source surface.

4.4.2 Results and Discussions

The predicted total sound field in the room from the room acoustics ESM was compared with the BEM predictions (treated as true values) at the receiver locations for the frequencies of 125 Hz, 250 Hz, 500 Hz and 1000 Hz. The locations of the receivers (identified by indices) are shown in Figure 4.17 together with the source surface. The prediction comparisons at different frequencies are shown in Figure 4.18 to Figure 4.21. Recall that the maximum source order in the ESM was 4 for the four lower frequencies and 6 for the highest frequency.

From the results shown in Figure 4.18 to Figure 4.21, it is easily observed that, in general, the ESM predictions are in good agreements with the true values (the BEM calculations)

at all tested frequencies without going to very high source order. It can also be noticed that there are some small mismatches at the receivers that have large sound pressure amplitudes for some frequencies which correspond to the receivers that are very close to the source surface. These mismatches are not significant since firstly, the differences would not be noticeable if a decibel unit were used to present the results and moreover, in most room applications, for example predicting the acoustics of a loudspeaker or a television in a room, the listeners' locations are usually not very close to the source surfaces, and thus such ESM predictions are well suited for this practice. It is also noted that although the results presented here are only up to 1000 Hz, limited by a PC's computation power to perform BEM calculations for higher frequencies, the ESM simulations are not restricted by this frequency limit. Therefore the validity of the room acoustics ESM is demonstrated in 3D cases and the conclusions from the 2D room acoustics ESMs can be similarly extended to 3D.

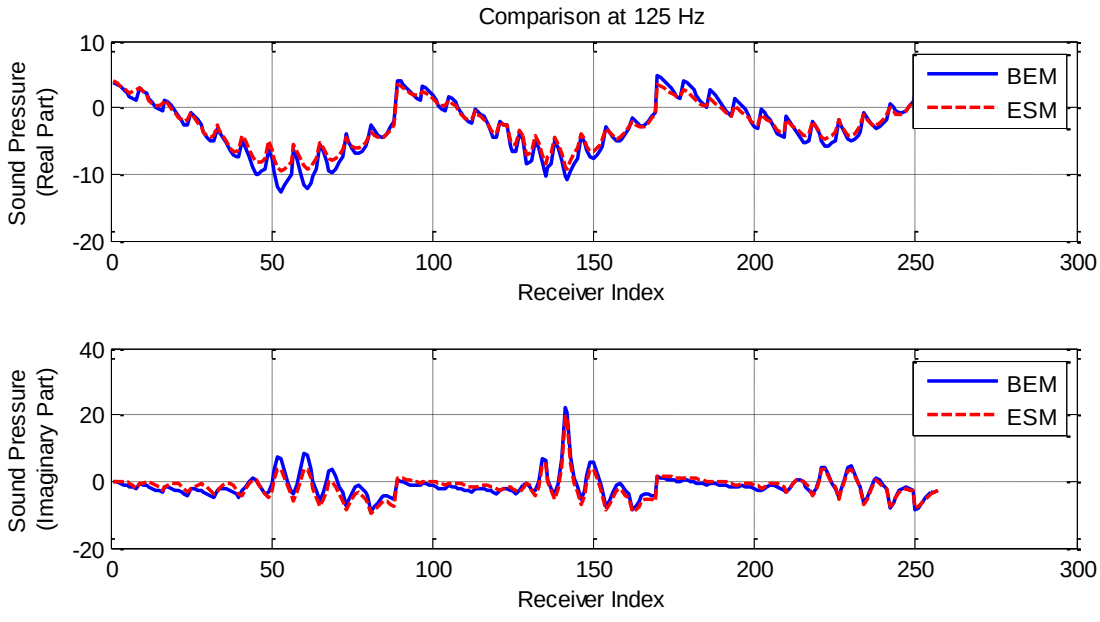

Figure 4.18. The comparison of the ESM and the BEM predictions at 125 Hz.

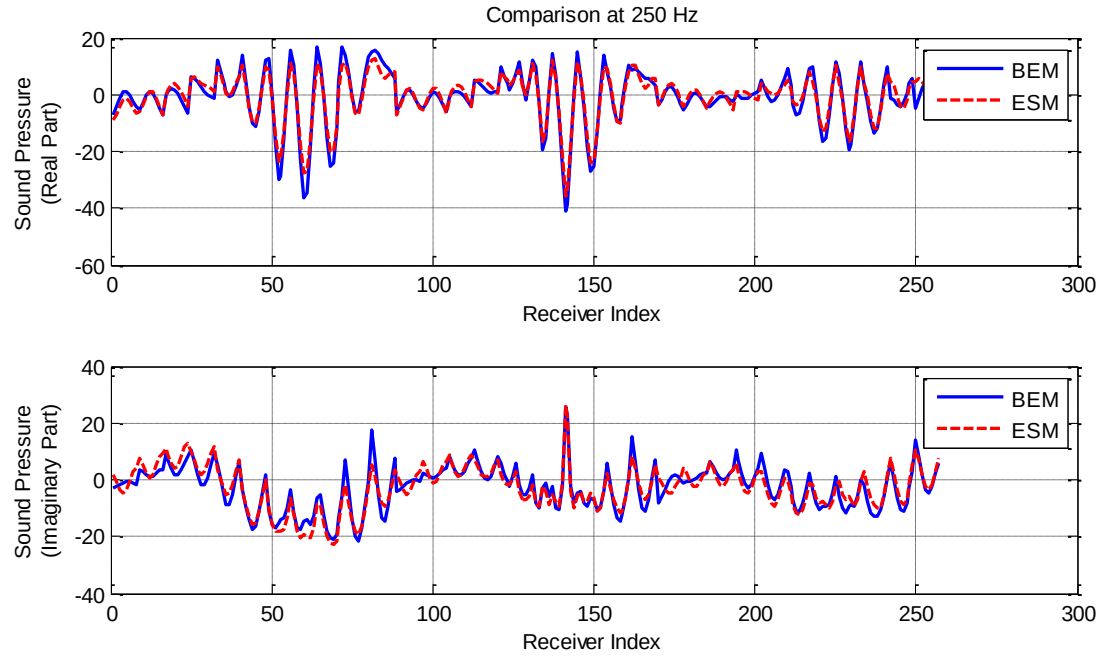

Figure 4.19. The comparison of the ESM and the BEM predictions at 250 Hz.

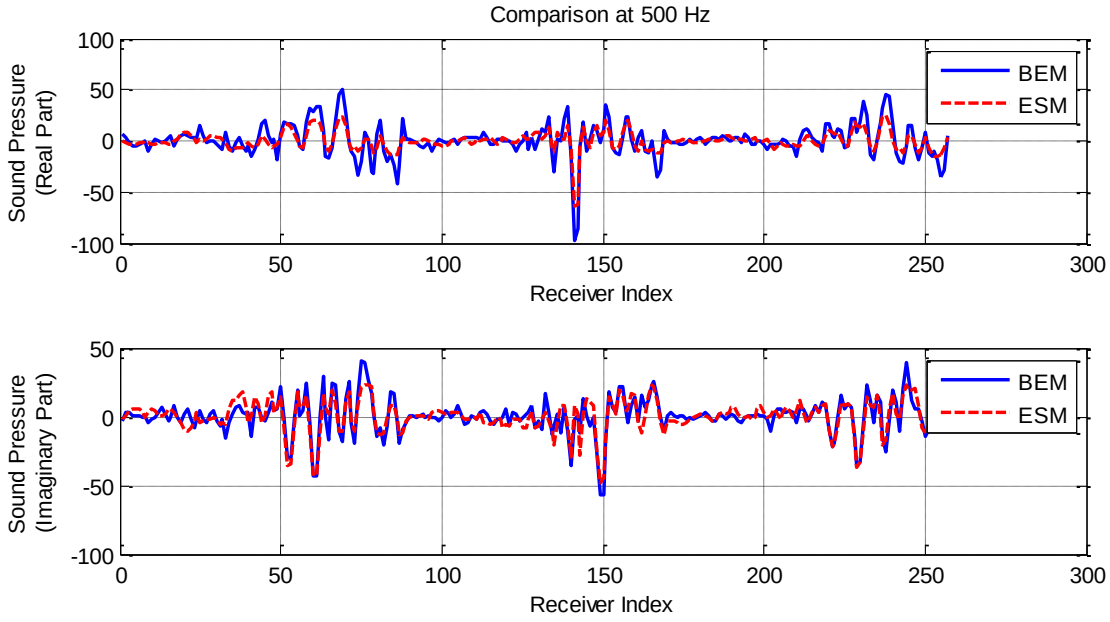

Figure 4.20. The comparison of the ESM and the BEM predictions at 500 Hz.

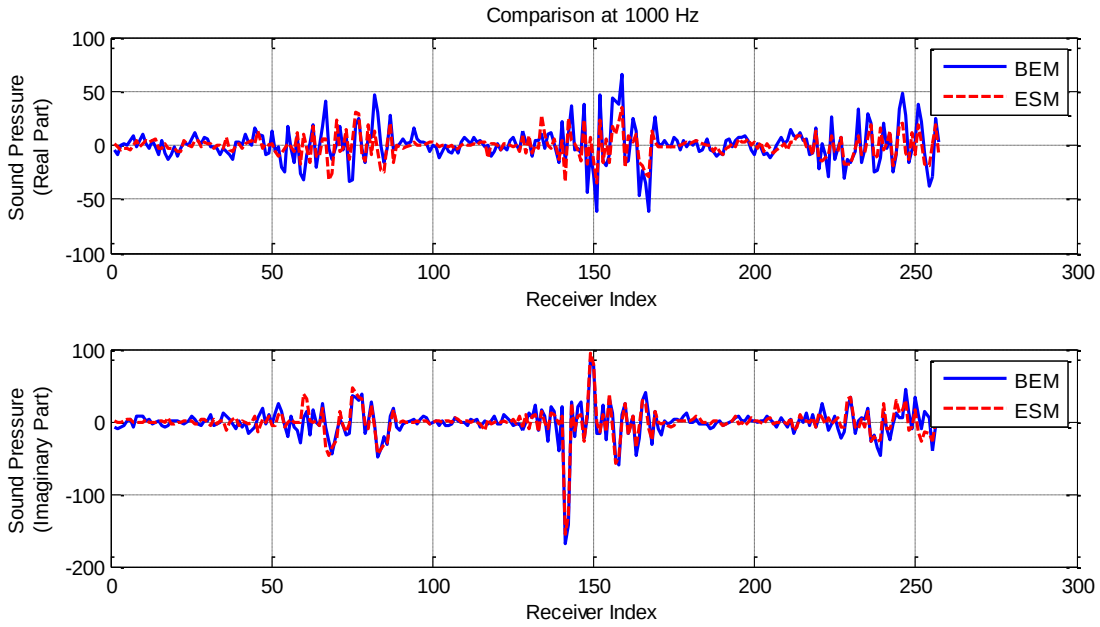

Figure 4.21. The comparison of the ESM and the BEM predictions at 1000 Hz.

4.5 Experimental Investigations

4.5.1 Experiment Setup

In the experimental validation of the room acoustics Equivalent Source Model, a measurement of the sound field generated by a loudspeaker was conducted in a small room with a non-uniform impedance distribution on its surfaces. The predicted sound pressure was then compared with the measured sound pressure at the receiver locations to indicate the performance of the model. Similar to the experimental setup in Chapter 3, the loudspeaker used in this experiment was Infinity Primus P163 with the dimension 0.265 m $\times$0.207 m $\times$0.37m; it was placed in a rectangular-shaped room (1.867 m$\times$1.771 m$\times$1.950 m) with all the surfaces of the loudspeaker parallel to the corresponding surfaces of the room. The setup of the experiment and the geometrical relation between the loudspeaker and the room are illustrated in Figure 4.22 and Figure 4.23, where the distance between the

back face of the loudspeaker to that of the room is 0.858 m; the distance between the right face of the loudspeaker and that of the room is 0.775 m; the distance between the two bottom faces is 1.00 m. The surfaces of the room were covered by plywood panels which were then partially covered by sound absorbing materials (Johns Manville, Microlite AA Premium NR Blankets) of 1 inch thickness. The uncovered regions are highlighted in the left figure in Figure 4.23. The sound field was measured by using a 18-channel planar array (Brüel & Kjær, sliced wheel array WA-1558-W; microphones: Brüel & Kjær, Type 4959), at four sides of the loudspeaker (measurement planes were parallel to the front, left, back and right faces of the loudspeaker). As shown in Figure 4.24, measurements are performed at the receivers on two planes on each side of the loudspeaker: one at a distance of 0.25 m away from the corresponding loudspeaker face and the other at a distance of 0.5 m. The sound field was measured separately on each measurement plane with a white noise input signal to the loudspeaker, and the individual measurements were then synchronized together to form a simultaneous measurement by using the transfer function method (Kim, et al., 2004) (Lee and Bolton, 2006) with the input signal to the loudspeaker as the reference signal.

Figure 4.22. Setup of the experiment.

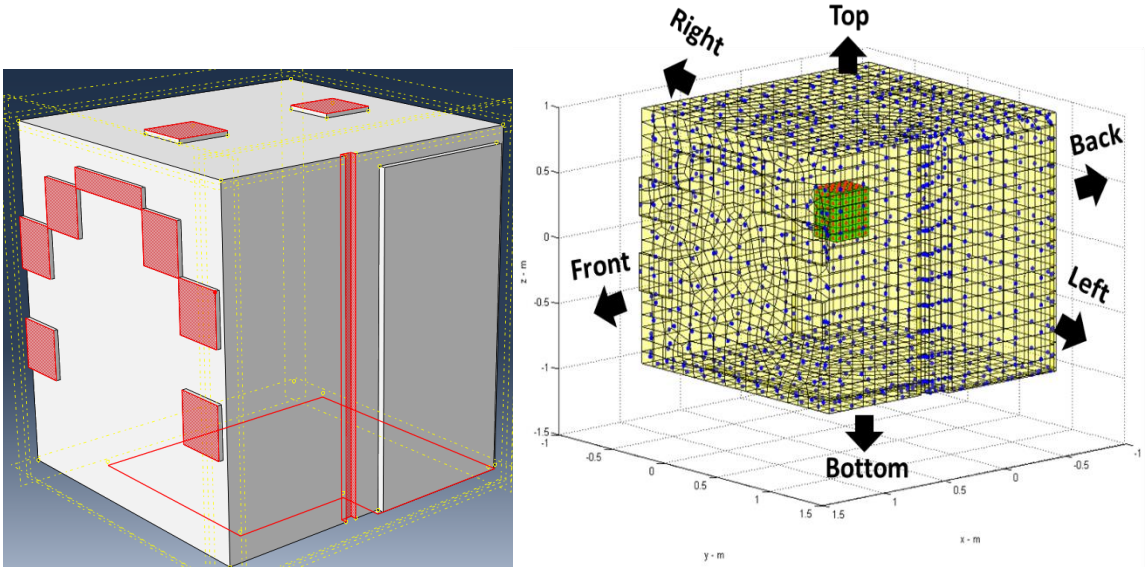

Figure 4.23. Left: room geometry (highlighted regions are not covered by sound absorbing materials); Right: geometry relation of the loudspeaker (green) and the room (yellow) and the sampling points on the source surface (red) and the room surface (blue) that were used in the Equivalent Sources Model.

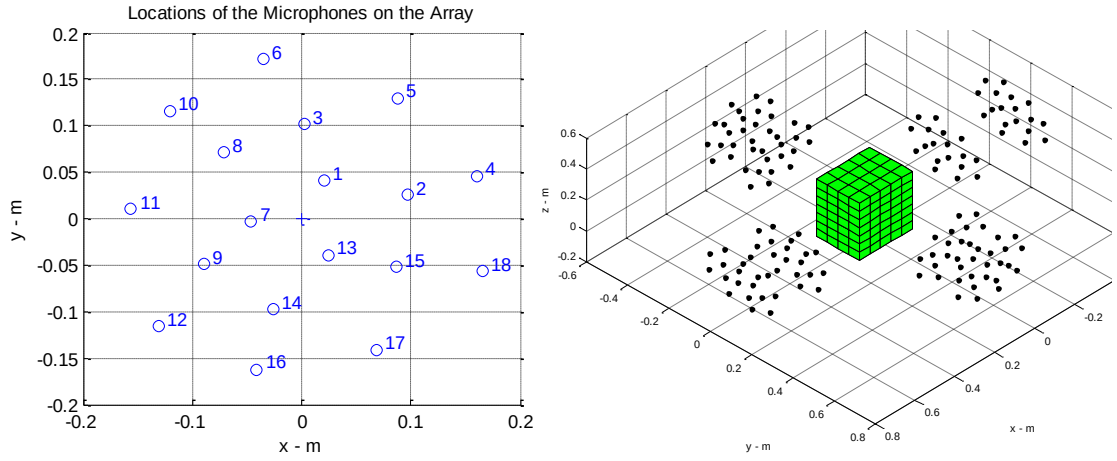

Figure 4.24. Left: the receiver locations on the array; Right: the receiver locations (black dots) in the whole measurement (the green box represents the loudspeaker).

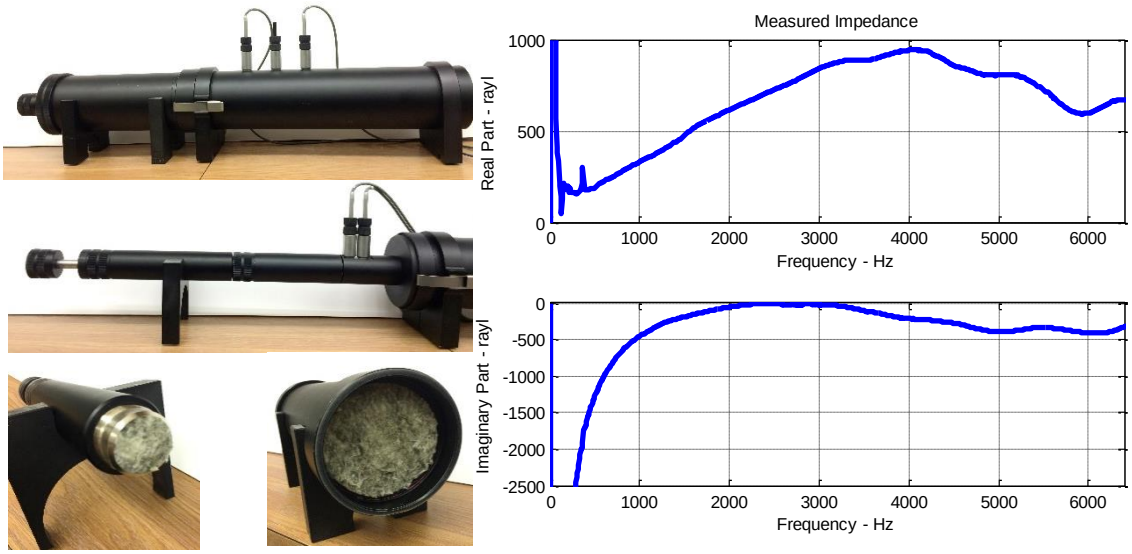

Figure 4.25. The setup and results of the impedance measurement.

The normal specific acoustic impedance of the sound absorbing material on a hard surface was measured by the two-microphone method (Standard I.S.O., 10534-2) in a standing wave tube (Brüel & Kjær, Type 4206). This measured impedance was used as the impedance boundary condition, under the assumption of local reaction, for the covered surfaces of the room. The setup and the result of the impedance measurement are shown in Figure 4.25. The uncovered plywood surfaces were considered to be acoustically hard surfaces. For the boundary condition on the loudspeaker surface, it was assumed that the normal velocity distribution on the source surface was the same as in the free-space environment: i.e., it was assumed that the sound reflected from the room surface caused negligible velocity change on the loudspeaker surface. The validation of these boundary conditions involves two parts: (1) validate that the velocity of the diaphragm and the tweeter of the loudspeaker is not changed by the presence of the reflected sound from the room surfaces; and (2) the velocity on the (uncovered) wooden surfaces can be assumed

zero (all the surfaces on the loudspeaker except the diaphragm and the tweeter are also made of wood). The first part was validated by another experiment (the setup of which is shown in Figure 4.26) where the velocity of the diaphragm and the tweeter of the loudspeaker was measured by a laser vibrometer (Polytech PSV-400 scanning head, Polytech OFV-5000 Controller) when the loudspeaker was placed with its front face facing a large wooden surface but at different distances (from 0.5 to 1.7 m). It was observed from the measurement results (shown in Figure 4.27) that the velocity of both the diaphragm and the tweeter is not changed within this distance range, i.e., the reflected sound field causes negligible velocity change on these regions. In the small room measurement setup mentioned earlier (illustrated in Figure 4.23), the distances between the loudspeaker and the room surfaces are within the distance range in the laser vibrometer measurements and the room surfaces are acoustically softer than the plywood surface used in the laser vibrometer measurement, thus the reflected sound field in the room experiment could cause even smaller velocity change to the diaphragm and the tweeter compared with the velocity change that occurred in the laser vibrometer measurement which can be regarded as zero. Therefore part (1) of the validation of the boundary condition is demonstrated. Part (2) of this validation, i.e., that the uncovered wooden surfaces are acoustically hard, is generally accepted in the acoustics area and can be further justified by the experimental results in Chapter 3, where the BEM prediction of the sound field agrees well with the measurement when using the velocity boundary condition on the loudspeaker surface such that the diaphragm and the tweeter have a rigid body motion (the velocities of which are obtained from the laser vibrometer measurement) and the rest of the surfaces have zero velocity. To apply the velocity boundary condition on the loudspeaker surface in this room acoustics

application, it is only necessary to set $\beta_1 = 0$ in Eq. (4.4). The velocity distribution on the source surface was calculated by a free-space Multipole Equivalent Sources Model obtained from the work in Chapter 3 where the sound pressure was measured for the same loudspeaker in an anechoic environment. Thus the simulation in the present work involves using a free-space Equivalent Sources Model as an input to a room acoustics Equivalent Sources Model.

Figure 4.26. Setup of the laser vibrometer measurement of the diaphragm and the tweeter's velocity of the loudspeaker.

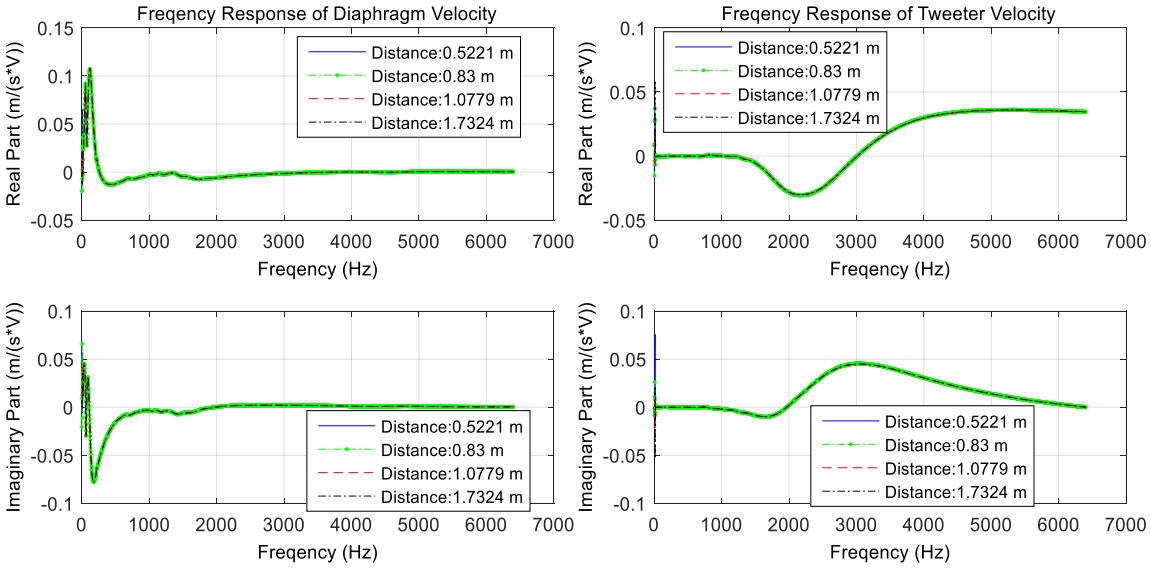

Figure 4.27. Measured frequency responses of the diaphragm and the tweeter's velocity to the input signal to the loudspeaker (no noticiable velocity changes within this distance range).

4.5.2 Measurement Results and Discussions

After determining the boundary conditions on different surfaces, the sound field in the room can be simulated by using the room acoustics Equivalent Sources Model described in Section 4.2.2. The equivalent sources used in the present work are the multipoles up to order three. To calculate the source strengths, 487 sampling points on the room surface and 166 sampling points on the source surface were used (illustrated in Figure 4.23). The model-predicted sound pressure is compared with the measured sound pressure at all the receiver locations, and the comparison results are shown at 520 Hz, 1024 Hz and 2000 Hz in Figure 4.28 to Figure 4.33, where the receiver indices are ordered such that receiver indices from 1 to 72 correspond to the measurements with a smaller distance (0.25 m) to the source, and 73 to 144 with a distance of 0.5 m; while at each measurement distance the 72 indices are ordered as front face measurement, left face, back face and then right face.

From the comparison results, it is seen that the Equivalent Sources Model (ESM) prediction does not agree well with the experiment result at 520 Hz. Although better agreement is seen at higher frequencies (1024 Hz and 2000 Hz), that does not indicate good model performance since the total sound field is close to the free-space sound field at these frequencies, which suggests that good model prediction occurs simply because the room surface is very absorptive at higher frequencies and the room component sound field is close to zero. Overall, the ESM prediction tends to be close to the free-space sound field.

To further analyze the reason for this, a simulation using the Boundary Element Model (the same process as in Section 4.4) was carried out at 520 Hz, in which there were 3438 nodes in the mesh (more than 6 nodes per wave length). From Figure 4.34, it is first noticed that the BEM prediction agrees reasonably well with the experiment. Also from the BEM calculation, the sound pressure and the normal particle velocity distribution of the room component sound field (i.e., the component that is represented by ESM) can be extracted for both the room surface and the source surface. With this information extracted from BEM, the source strengths of the ESM (with the same model structure as the ESM described in the previous paragraph) can be estimated based on three different types of boundary condition: the room component pressure boundary condition, the normal velocity boundary condition and the impedance boundary condition (Eq. (4.7)). By comparing the performance of the ESM's with these three boundary conditions, it is observed that the prediction using the pressure boundary condition shows a fairly good agreement with the BEM and the experiment results, while the other two boundary conditions result in predictions that are close to each other and are, seem from Figure 4.28, both close the free-

space sound field. These observations imply that it is valid to use a small number of higher order equivalent sources to represent the room component sound field, and that the use of the velocity boundary condition to calibrate the ESM is more likely to produce errors in sound pressure predictions. For the prediction from the impedance boundary condition, its formulation, as seen from Eq. (4.7), is a linear combination of the pressure and the velocity boundary condition, so the least square estimate can be viewed as a weighted average of the results from the other two boundary conditions. The admittance serves as the weighting factor of the result from the pressure boundary condition, while the weighting factor for the velocity boundary condition is one. Since, from Figure 4.25, the impedance is on the order of 10^{3}, the weighting factors for the pressure boundary condition (on the order of 10^{-3} for the material covered surfaces and zero for the hard surfaces) are very small compared with one. This causes the prediction from Eq. (4.7) to be closer to the prediction from the velocity boundary condition which produces large errors. This means that for cases where the admittance is small, the direct use of the least square estimate from Eq. (4.7) will produce large errors in the room acoustics predictions. One possible physical reason might be that the room geometry is almost rectangular and the sound field in the room is a combination of the room modes for a rectangular geometry which are difficult to represent by using the multipole equivalent sources. The room modes are relatively significant at this frequency, since it is observed that the near field of the sound field at the back side of the loudspeaker (receiver indices: 37 to 54) is large where the free-space component is small which is possibly due the contribution from the acoustical modes of the room. Based on the above observations, it is suggested here, as a possible solution to this issue in the future work, that the acoustical modes for the room geometry and the

corresponding impedance boundary condition on the room surfaces could be used as the equivalent sources at low frequencies and that the multipole equivalent source are used at high frequencies.

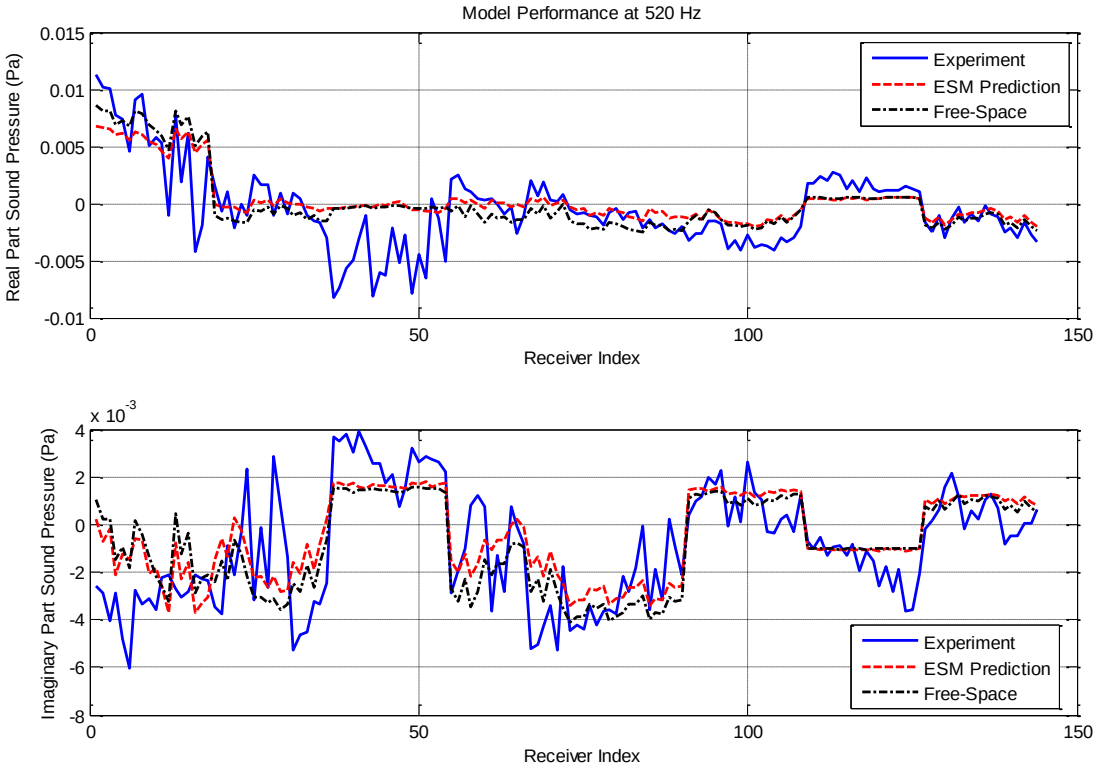

Figure 4.28. Comparison of measurement and model prediction at 520 Hz (plot with receiver indices).

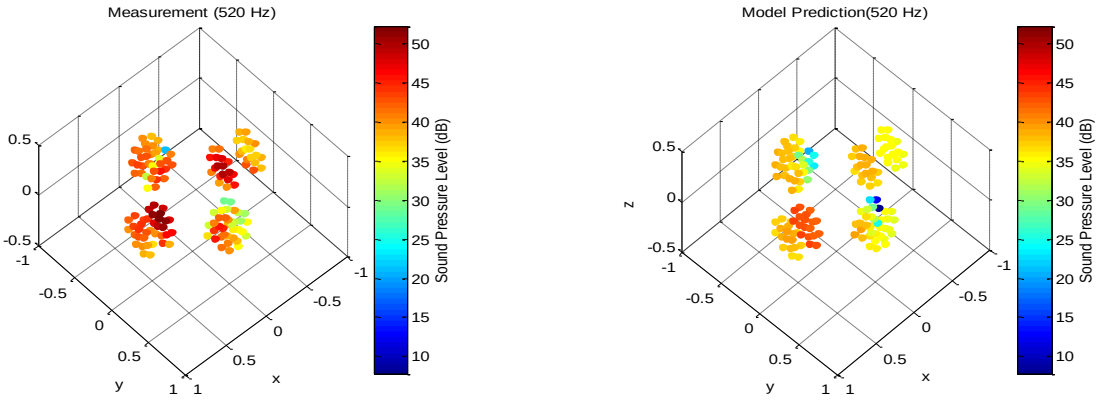

Figure 4.29. Comparison of measurement and model prediction at 520 Hz (spatial distribution).

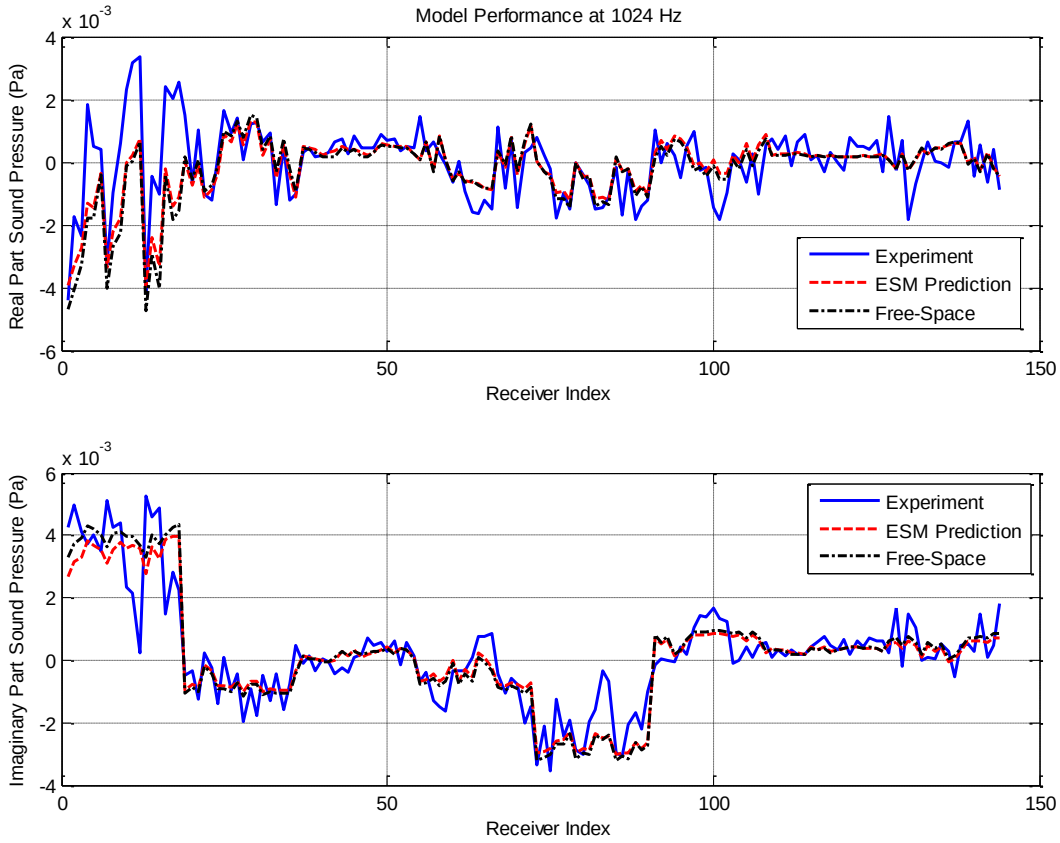

Figure 4.30. Comparison of measurement and model prediction at 1024 Hz (plot with receiver indices).

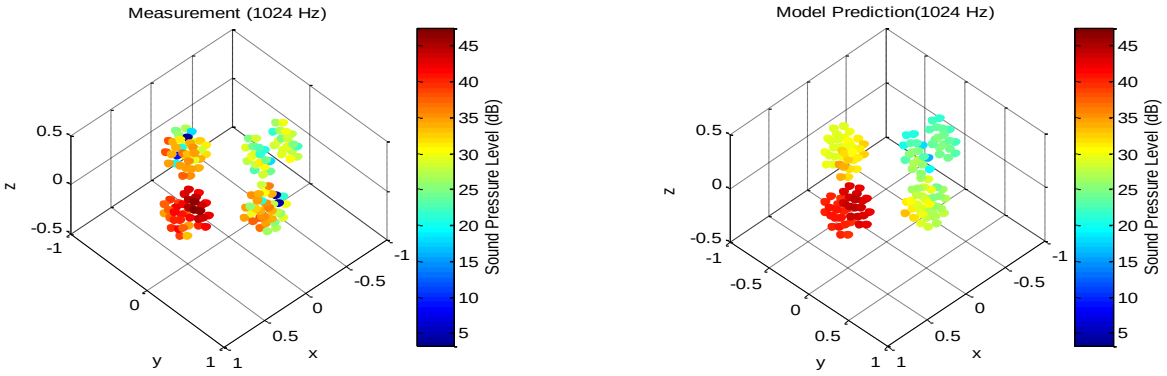

Figure 4.31. Comparison of measurement and model prediction at 1024 Hz (spatial distribution).

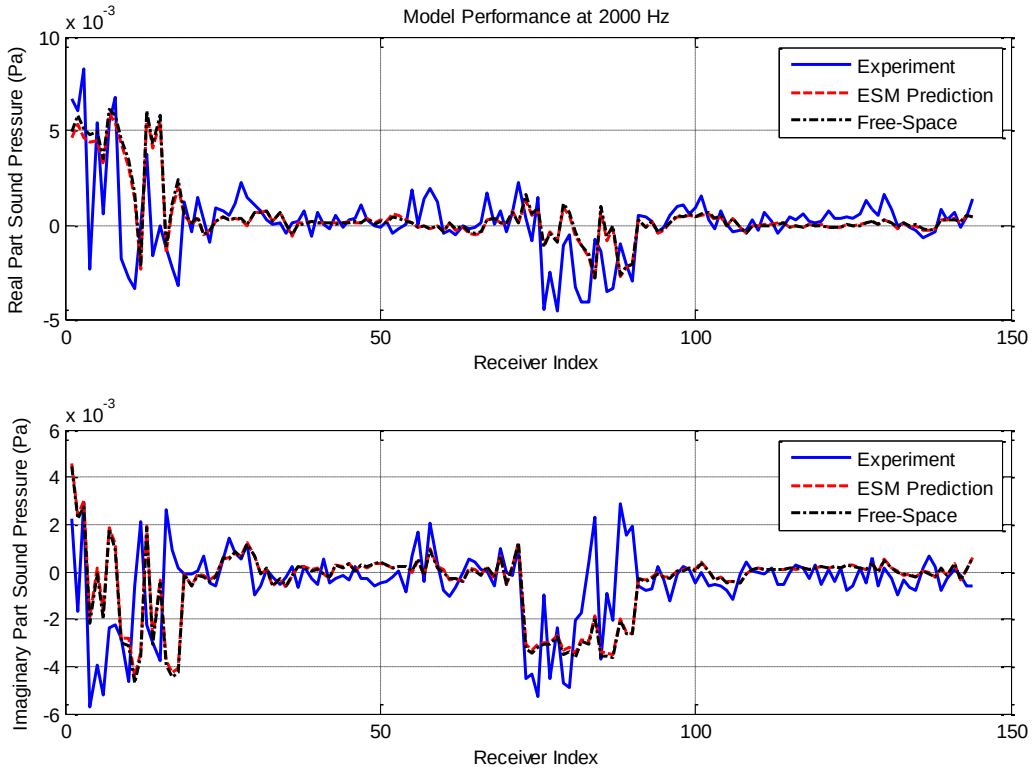

Figure 4.32. Comparison of measurement and model prediction at 2000 Hz (plot with receiver indices).

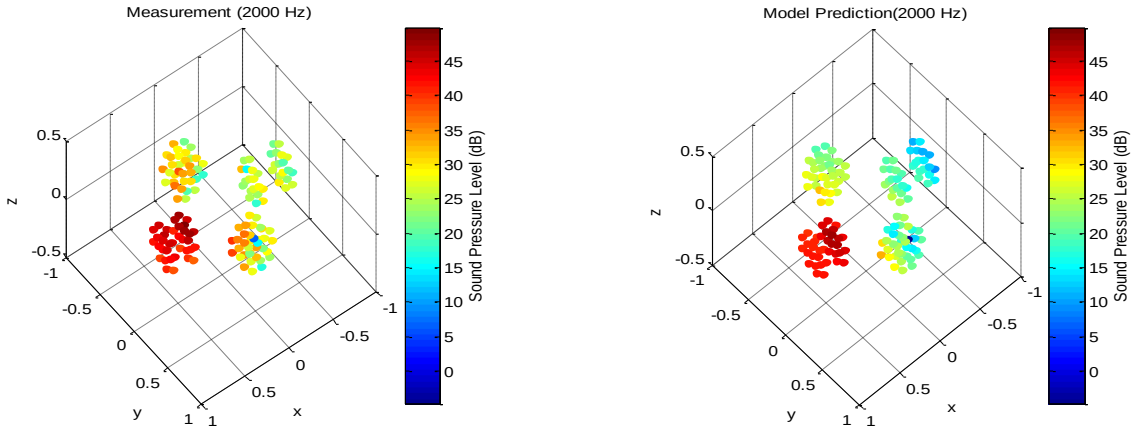

Figure 4.33. Comparison of measurement and model prediction at 2000 Hz (spatial distribution).

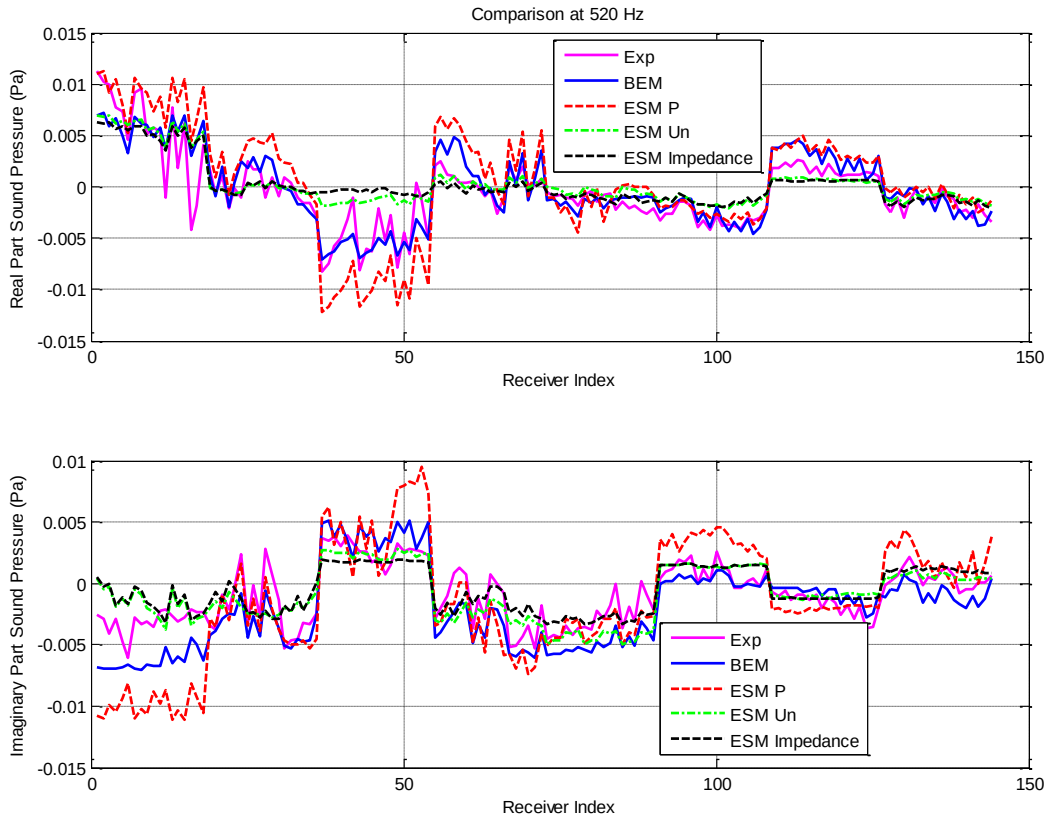

Figure 4.34. Comparison of model performance of BEM and ESM based on different types of boundary conditions (pressure, velocity and impedance boundary conditions) at 520 Hz.

4.6 Summary

A reduced order modeling method, the room acoustics Equivalent Sources Method (ESM), was developed to simulate the sound field in a room environment with arbitrary room geometries, sources of finite size and non-uniform surface impedances. This ESM for room acoustics, in contrast with those used for free-space predictions, describes the room component sound field rather than the total sound field as generated by the assumed equivalent sources. The boundary conditions for the room component, on both the room surfaces and the source surfaces, were derived in terms of the free-space component sound field and the surface normal impedance. With a knowledge of the free-space component, which can easily be calculated from the given source information, the parameters of the ESMs can be estimated and the process of the room acoustic simulation is then complete.

As a preliminary investigation, two types of Equivalent Source Models for room acoustics were constructed and implemented in simulations in two-dimensional rooms, one consisting of layers of monopoles distributed exterior to the room region and the other consisting of incoming and out-going multipoles. The monopole distribution ESM was implemented by estimating the source strength of monopoles that were placed both inside the source surfaces and outside the room surfaces to match the boundary conditions through a least-squares approach together with Tikhonov regularization and Generalized Cross Validation to determine the regularization parameters. For the construction of the multipole ESM, the sound field expression of an arbitrarily-oriented multipole of any order was derived and the source strengths were estimated in a process similar to that for the monopole ESM, but using truncated singular value decomposition to regularize the

estimation process. The regularization parameters for the multipole ESMs were chosen based on the observation of a sharp transition in the singular value distribution of the system matrix in the inverse process. The room environment in this 2D simulation involves a circular-shaped room surface with non-uniform surface impedance and a finite-size source surface of the same geometry driven by a non-uniform velocity distribution. The prediction accuracies of both types of ESMs, i.e., the monopole distribution ESM and the multipole ESM, were analyzed by comparing the predictions with the results from a BEM procedure (treated as the "true values"). The simulation results showed that the monopole distribution ESM without regularizations can only be applied to models with a relatively small number of sources, which can give stable and accurate predictions up to 2500 Hz in the present geometry. To achieve a wider performance range by increasing the number of assumed sources, the application of regularization is necessary. In general, to predict the sound field at higher frequencies requires a larger number of sources; however, accurate predictions at some frequency components, at which unstable results are introduced by the regularization, require a much larger number of sources than is necessary for even higher frequency components where the regularization does not cause any instability. In the analysis of the multipole ESMs, their performance was found to be more robust than that obtained from the monopole distribution ESMs, and an improvement in prediction accuracy can be achieved by increasing the highest source order contained in the model. It was also indicated that by appropriately choosing the highest source order included in the multipole ESM, the tradeoff between prediction accuracy and computational speed can be adjusted flexibly as needed in a particular application.

Further studies were conducted to investigate the possibility of extending the 2D implementation of the room acoustics ESMs to 3D. Due to the advantages of the multipole ESM, compared with the monopole distribution ESM, observed from the 2D simulations, only the multipole ESM is implemented in 3D room space simulations. An ESM using the 3D multipole series of monopole, dipoles, quadrupoles, etc. was constructed and the source strengths of which were estimated in a similar way as in the 2D simulations. By comparing the ESM predictions with the BEM results at frequencies up to 1000 Hz in an Alpha cabin with a sphere source at the center, it was shown that the 3D room acoustics ESM offers predictions consistent with the BEM results in the demonstrated frequency range. For higher frequencies, the ESM might still give accurate and efficient predictions, but it was not compared with the BEM results due to the computational limitation of a personal computer to conduct BEM calculations at higher frequencies.

After the simulation investigations, the performance of the room acoustics ESMs were also studied experimentally. In the experiment, a rectangular loudspeaker was placed at the center of a small rectangular room whose surfaces were made of plywood, but a large portion of the room surface were then covered by sound absorbing materials. The free-space ESM of the loudspeaker was used to give the source information which was then used as an input to the room acoustics ESM to simulate the sound field in the room. From the results, it was shown that when multipoles are used as the Equivalent Sources, the model prediction can achieve reasonable accuracy if the sound pressure boundary condition of the room component sound field is used to calibrate the model, but if the normal velocity boundary condition is used, the sound pressure prediction contains large errors. In a

realistic room acoustics simulation practice, the available boundary condition is the impedance boundary condition, and if a direct least-square estimate is used for calculating the strength of the equivalent sources, the prediction from the impedance boundary condition results in a weighted combination of the results from the pressure and the velocity boundary conditions where the value of the admittance is the relative weighting factor for the pressure boundary condition result. For the experimental condition in the present work, the admittance is small compared with one, which leads to a model prediction that is close to the result using the velocity boundary condition. Physically, this relatively large discrepancy might result from the difficulties of using the multipoles to represent the sound field where the acoustical modes of a rectangular room geometry are significant. This leads to the suggestion to use the acoustical modes for the room geometry and satisfy the impedance boundary condition of the room surface as the equivalent sources at the low frequency range and then use the multipoles ESM for the mid and high frequency range.

CHAPTER 5. FREE-SPACE SOUND FIELD PREDICTION AT HIGH FREQUENCIES USING LOCAL-BASIS METHODS

5.1 Introduction

The development of the free-space sound field prediction model discussed in Chapter 3 makes it possible to accurately predict the sound field for almost the whole audible range, a feasible frequency limit much higher than most traditional methods in acoustical holography. It is, however, not expected to have such a wide feasible frequency range when the source is much more complicated than the loudspeaker which was used in the experiment in Chapter 3, since the spatial variation of the sound field generated by a complicated source is usually very large and a large number of measurement points are required in space to achieve accurate model prediction when equivalent source models are used. It will be demonstrated in this chapter that an alternative simulation technique can be constructed to accomplish the same task as that mentioned in Chapter 3, but specifically for very high frequencies.

The idea of proposing this new method for simulations at very high frequency is mainly based on the analysis of the sources of errors in the parameter estimation processes in Equivalent Source Methods (including the one constructed in Chapter 3). For realistic sound sources, the sound field usually becomes complicated at high frequencies, and the series representing the sound field (i.e., the sound field from the equivalent sources)

converges at very high orders, so that a large number of measurements with high spatial resolution are required to estimate all the coefficients, especially for those higher order terms with rapid spatial variations. This means that "required" information is missing in the spatial gaps among the measurements at high frequencies. Since each term in the series chosen to represent the sound field in most of the available techniques contributes to the sound field over the whole space, the missing information would affect the estimation of the series coefficient: i.e., the error in the coefficient estimation for each term is an accumulation of missing information in all measurement gaps. This observation has motivated the present approach of using a local basis, i.e., a basis that contributes to the sound field only in a certain region, to describe the sound field, instead of a global basis as used in most available techniques. One feature that makes it convenient to use a local basis in high frequency sound field reconstruction is that the radial dependence of the sound field generated by a single physical source (with a relatively small spatial size), when represented by spherical waves in a spherical coordinate system, can be, under the assumption of high frequencies, approximated by an expression (as discussed in detail in Section 5.2) such that the sound pressure along a radius at certain angular direction is determined by the sound pressure at one point on the radius and does not depend on the sound field at other angular directions. This feature is used differently in the development of the two local-basis methods described in this chapter: one for the case of a single source (or sources that are located within a small region in space), and the other extends to the case of multiple sources (e.g., the sound field generated by several loudspeakers, each of which is some distance apart from the others).

For the situation of having a single source, as the objective of the first local-basis method, the special feature for high-frequency sound fields described in the previous paragraph suggests that the sound field for the whole space is determined by the sound pressure distribution on the unit sphere centered at the origin of the spherical coordinate system, and also suggests that a measurement at an arbitrary location can be "projected" onto the unit sphere (i.e., the sound pressure at the location having the same angular coordinate, but with unit radius, can be calculated). After this projection, the measurement are converted to sound pressure sampling points on the unit sphere. Then, the sound pressure distribution on the unit sphere can be interpolated from these sampling points by using piece-wise interpolants, which are the local basis used in this first method. After the interpolation, the resultant sound pressure distribution on the unit sphere can then be used to predict the sound field for the whole space.

In the development of the second local-basis method, where multiple sources contribute to sound field at the same time, the measurement cannot be "projected" in a similar way to the first method. To overcome this difficulty, the primary idea in the second method is to avoid using interpolation: instead, first create mesh grids on the unit spheres around the origins of each set of spherical waves, so that the nodal sound pressure values on, and the corresponding shape functions (the local basis used in this method), can be used to determine the sound field in the whole space. The three-dimensional sound field can then be predicted after a least-squares estimation of the nodal values based on the measurements. Another advantage of using the local-basis methods over the global basis methods is that, due to the local nature of the basis, when measurement information is given only in certain

solid angle region, good predictions can still be achieved in that region and are not affected by the missing information in other regions. It is also noted here that this second local-basis method, in principle, can easily be extended to reconstruct the sound field in an interior environment as well, one must only include both incoming and outgoing sources and proceed with the prediction in the same way as described in this chapter.

5.2 Theories of High Frequency Sound Field Reconstruction

The use of the local-basis method to reconstruct the sound field at high frequencies is mathematically dependent on the approximated form of the sound field expression for a single source (or all sources that are located in a single small spatial region) under the assumption of large wavenumber, which will be derived and discussed in the first subsection below. This approximation can be interpreted as being: the sound field is similar to a monopole sound field with a certain angular directivity pattern. Then two different local-basis sound field reconstruction methods are introduced: one focusing on the situation of a single source and the other dealing with the case of multiple sources.

5.2.1 Approximate Representation of the High Frequency Sound Field

If there is only one small-sized source in space or there are multiple sources but that are all located within a small spatial region, the sound field generated by this source can be effectively represented by the spherical wave series with the origin located on the center of the small source region (referred to as the source location in this chapter). The approximated sound field expression can be derived from the spherical wave decomposition (Williams, 1999) of a sound field. Any out-going sound field in free space,

with the time dependence of $e^{-j\omega t}$, can be expressed as an infinite series of spherical waves, in spherical coordinates, as:

$$P(r,\theta,\phi)=\sum_{n=0}^{\infty}C_{mn}h_n(kr)\sum_{m=-n}^{+n}P_n^m(\cos(\theta))e^{jm\phi}, \tag{5.1}$$

where r is the radius, ϕ is the azimuthal angle ranging from 0 to 2π and θ is the polar angle ranging from 0 to π; k represents the wavenumber, $h_n(\cdot)$ denotes the nth order spherical Hankel function of the first kind, and $P_n^m(\cdot)$ denotes the associated Legendre polynomial; the integers m and n are referred to as the order and the degree of this series, and C_n^m is the coefficient of each term in the series (i.e., the spherical wave basis).

From Eq. (5.1), it is observed that the radial dependence of the sound field is expressed by the spherical Hankel functions with the product kr as the argument. The power series expansion of the spherical Hankel functions, $h_n(z)$, can be expressed as

$$h_n(z)=(-j)^{n+1}\frac{e^{jz}}{z}\sum_{m=0}^{n}\frac{j^m}{m!(2z)^m}\frac{(n+m)!}{(n-m)!}, \tag{5.2}$$

where, in the context of sound field representation: $z=kr$. Thus, the amplitude of the radial dependence of the sound field contains only negative powers of kr. When the frequency is high (i.e., for large wavenumbers), the argument kr is significantly large so long as the radius is not close to zero. The latter observation suggests that the terms in the expansion of the spherical Hankel function with powers less than -1 become very small at large kr, and thus can be eliminated from the series without introducing significant error.

After this truncation (by setting $m = 0$ in Eq. (5.2)), the approximated expression for $h_n(kr)$ is obtained as:

$$h_n(kr) \approx \frac{(-j)^{n+1}}{k} \frac{e^{jkr}}{r}. \tag{5.3}$$

After substituting the approximated expression in Eq. (5.3) into Eq. (5.1), the sound field at high frequencies (radius not close to zero) can therefore be approximated by the series:

$$P(r, \theta, \phi) \approx \frac{e^{jkr}}{r} \sum_{n=0}^{\infty} \sum_{m=-n}^{+n} D_{mn} P_n^m(\cos(\theta)) e^{jm\phi}, \tag{5.4}$$

where the coefficients: $D_{mn} = (-j)^{n+1} C_{mn}/k$.

Since the special case of radius close to zero is not considered here, it is assumed that no measurements are taken, and no predictions are made, near the origin. In that case, it can be seen from Eq. (5.4) that the radial dependence of the sound field at high frequencies is decoupled from the angular coordinates, and that the sound field in a certain solid angle region does not contain contributions from other solid angle regions. More specifically, given the sound pressure at an arbitrary location (r, θ, ϕ), the sound pressure at its corresponding location on the unit sphere, $P(1, \theta, \phi)$, can be easily evaluated by using the simple relation:

$$P(r, \theta, \phi) = P(1, \theta, \phi) \frac{e^{jk(r-1)}}{r}. \tag{5.5}$$

It is also noted that if the time dependence is, instead, assumed as $e^{-j\omega t}$, the spherical Hankel function of the second kind needs to be used to instead of the first kind in the derivation described above, which will then result in a similar relation to Eq. (5.5):

$$P(r,\theta,\phi) = P(1,\theta,\phi)\frac{e^{-jk(r-1)}}{r}. \tag{5.6}$$

Equation (5.5) or Eq. (5.6) is the approximated expression for the high frequency sound field which is used in constructing either the local-basis method to reconstruct the sound field from a single source or from multiple sources.

5.2.2 Local-Basis Reconstruction for a Single Source

In the development of the first local-basis method here, it is assumed that there is only one source (all physical sources are in a small spatial region) in space and a spherical coordinate is defined with the origin being the source location (center of the small source region). When the sound pressure at the locations corresponding to all of the measurements in space are evaluated by Eq. (5.5) or Eq. (5.6), the corresponding $P(1,\theta,\phi)$ can be calculated straightforwardly, i.e., after they are "projected" onto the unit sphere, the sound pressures at a number of distributed points on the unit sphere are obtained. Then the sound pressure distribution on the unit sphere can be estimated by using piece-wise interpolation from the distributed points (the piece-wise interpolants are the local basis for this method), which means that the estimated sound pressure in a small region on the unit sphere depends only on the neighboring sound pressures rather than on all measurement points. As mentioned earlier, when a localized basis is used to describe the sound field, the error in the estimation

does not accumulate from the missing information over the measurement surface (the unit sphere in the context here), and reasonable reconstruction results may be expected even if the measurement does not include complete information about the actual sound field.

The approximation of the sound pressure distribution on the unit sphere by a piece-wise interpolation from distributed data includes two main steps: (1) the division of the unit sphere into small regions (usually spherical triangles) by connecting the distributed points as the boundaries of the regions; and (2) the interpolation of the sound pressure inside each small region based on the sound pressure values on the nodes of the region and boundary conditions such as continuities of the function values as well as its derivatives.

Piece-wise interpolation of data on a two-dimensional plane, or a multi-dimensional Euclidian space, is a widely-studied area (Awanou, et al., 2005) (Bajaj, 1993), in which Delaunay triangulation (Lee and Schachter, 1980) and spline interpolation (Lai, 2007) are commonly used. For the case of interpolation on a sphere considered here, rigorously speaking, triangulation based on Geodesic distance (Renka, 1984) and spherical splines (Alfeld, et al., 1996 (1)) or polynomials defined on a sphere (Alfeld, et al., 1996 (2)) should be used, rather than performing interpolation directly by treating the angular coordinates as the Cartesian coordinates in a Euclidian space. However, for the purpose of demonstrating the advantages of using a local basis compared with a global basis to describe the sound field in a simple way, the “projected” measurements are assumed to be uniformly distributed on the unit sphere so that traditional interpolation techniques, i.e., techniques in Euclidian spaces, would give similar results to the methods specifically

designed for spherical surfaces, and thus the former were implemented in the present work. This is because, under this assumption, the result of triangulation based on both the Euclidian distance and the Geodesic distance would be similar. Specifically, the angular coordinates of the measurement locations are generated by the algorithm proposed by Leopardi (2006), in which the obtained points are the center of a specified number of regions on the unit sphere with equal areas and small diameters (i.e., close to regular shapes).

After triangulation, the sound pressure value within each triangle is interpolated by using a cubic spline on the domain $\theta \times \phi \in [0, \pi] \times [0,2\pi)$, with a periodic boundary condition specified in the ϕ direction as: $P(\theta, \phi) = P(\theta, \phi + 2\pi)$, and a boundary condition of constant value at the north and south poles: i.e., $P(0, \phi) = const$ and $P(\pi, \phi) = const$. Both types of boundary conditions are easily implemented in standard two-dimensional spline interpolation techniques. It is noted here that after projection to the unit sphere there is always a measurement point located on the north and south poles, respectively, when using the Leopardi algorithm; thus pressure values are always given at the north and south poles in the present work. If there are no measurements taken in the direction of the poles, the sound pressure at the poles can only be obtained by extrapolation.

5.2.3 Local-Basis Reconstruction for Multiple Sources

In the following formulation of sound field reconstruction from a number of sound pressure measurements in the space, it is assumed that the sound field is generated by multiple sound sources, not located close to each other, in space, and that each source is compact: i.e., it

can be enclosed by a sphere that is relatively small compared with the distance to the prediction locations. This assumption is necessary to guarantee the validity of the use of a spherical wave series to represent each source as well as the approximated form of each spherical wave series discussed earlier in Section 5.2.1. In addition, the locations of the sources, i.e., the origin of the spherical wave series describing each source, is assumed to be known. It is noted that a group of closely located sources can be treated as a single source in the current work.

If multiple sources are present, the total sound field in free space includes contributions from all of them, and the sound field generated by each individual source can be represented by a spherical wave series with its origin at the source location as described in Section 5.2.1. Thus the total free-space sound field can be expressed as:

$$\begin{aligned} p(\vec{x},\omega) &= \sum_{i=1}^{M} p_i(\vec{y}_i,\vec{x},\omega) \\ &= \sum_{i=1}^{M}\left[\sum_{n=0}^{\infty} C_{mn}^{i} h_n(kr_i)\sum_{m=-n}^{+n} P_n^m(\cos(\theta_i))e^{jm\phi_i}\right], \end{aligned} \tag{5.7}$$

where $p_i(\vec{y}_i,\vec{x},\omega)$ denotes the sound field contribution, evaluated at $\vec{x}$, from the ith source located at $\vec{y}_i$, ω is the angular velocity (as before, a time dependence of $e^{-j\omega t}$ is first assumed), and M is the total number of sources. The expression in the square brackets in the second line of Eq. (5.7) is the same spherical wave series representation as in Eq. (5.1) but applied to the ith source contribution, r_i, ϕ_i and θ_i are the radius, the azimuthal angle (ranging from 0 to 2π) and the polar angle (ranging from 0 to π) of the location $\vec{x}$ in the spherical coordinate system with its origin located at $\vec{y}_i$. All the other notations are the

same as in Section 5.2.1: k represents the wavenumber, $h_n(\cdot)$ denotes the nth order spherical Hankel function of the first kind, and $P_n^m(\cdot)$ denotes the associated Legendre polynomial, where the integers m and n are referred to as the order and the degree of this series, and C_{mn}^i is the coefficient of each term in the series.

The approximated expression of Eq. (5.5) can be applied to each source, the sound field component from the ith source can thus be related to the distribution of this sound field component on the unit sphere centered at the ith source location, $P_i(1,\theta,\phi)$, as:

$$p_i(r_i,\theta_i,\phi_i) = p_i(1,\theta_i,\phi_i)\frac{e^{jk(r_i-1)}}{r_i}. \tag{5.8}$$

By using the relation described in Eq. (5.8), the total sound field, created by all the sources, can be expressed, at high frequencies, as:

$$p(\vec{x},\omega) = \sum_{i=1}^{M}\frac{e^{jk(r_i-1)}}{r_i}p_i(1,\phi_i,\theta_i). \tag{5.9}$$

Recall that the above equation, Eq. (5.9), is for the time dependence of $e^{-j\omega t}$, and similar to the argument leading to Eq. (5.6), if the time dependence is $e^{j\omega t}$, the counterpart of Eq. (5.9) is

$$p(\vec{x},\omega) = \sum_{i=1}^{M}\frac{e^{-jk(r_i-1)}}{r_i}p_i(1,\phi_i,\theta_i). \tag{5.10}$$

After deriving this relation, the problem of constructing the total sound field is converted to estimating the sound field components from each source on the unit spheres centered at corresponding source locations.

Recall from Section 5.2.2 that the construction of the local basis representation of the sound field from a single source relies on the fact that there is only one term in Eq. (5.5) (or Eq. (5.6)). However, for the current consideration of having multiple sources, there is a sum of multiple terms as shown in Eq. (5.9) (or Eq. (5.10)). Because of this, the process of the direct projection of measurement to obtain sampling points on the unit sphere cannot be performed here. The main goal for this section is to overcome this difficulty.

In the construction of the local-basis formulation for multiple sources, a mesh grid is first generated on each unit sphere, S_i, whose origin is at the location of the ith source, as illustrated in Figure 5.1. It follows that the sound field component from the ith source on this unit sphere, $p_i(1, \phi_i, \theta_i)$, can be interpolated from the sound pressure at the nodes of the grid: specifically, the pressure can be expressed as:

$$p_i(1, \phi_i, \theta_i) \approx \sum_{q=1}^{N} p_i^{(q)} \xi^{(q)}(\phi_i, \theta_i), \tag{5.11}$$

where N is the total number of nodes of the grid on S_i, and $p_i^{(q)}$ denotes the sound pressure component from the ith source evaluated at the qth node of S_i. If (ϕ_i, θ_i) is located inside one of the neighboring elements of the qth node, $\xi^{(q)}(\phi_i, \theta_i)$ is the shape function associated with the qth node in that element; otherwise, $\xi^{(q)}(\phi_i, \theta_i) = 0$. It is again noted

here that the nodal pressure values, $p_i^{(q)}$, cannot be calculated directly from the measured sound pressures. In principle, there is no restriction on the choice of the grid generation method applied to the spheres; the basic polyhedron subdivision method (Fekete, 1990) was used here with the choice of the starting polyhedron taken from tetrahedron, octahedron or icosahedron (the choice criterion will be explained at the end of this section).

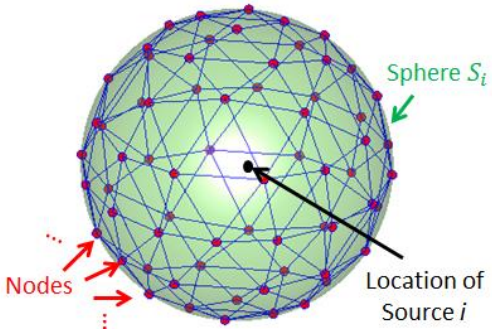

Figure 5.1. Mesh of the unit sphere around a source.

For convenience, a time dependence of $e^{-j\omega t}$ is assumed for the remaining part of this section, and one only needs to replace the wavenumber k by $-k$ in all the following derivations, if the time dependence is $e^{-j\omega t}$. With the same interpolation performed on unit spheres around all sources, the total sound field, by substituting Eq. (5.11) into Eq. (5.9), can then be expressed as:

$$p(\vec{x}) = \sum_{i=1}^{M} \frac{e^{jk(r_i-1)}}{r_i} \sum_{q=1}^{N} p_i^{(q)} \xi^{(q)}(\phi_i, \theta_i), \tag{5.12}$$

where the meanings of the various notations are consistent with Eq. (5.7) and Eq. (5.9), but the angular velocity, ω, in the time dependence has been omitted from now on for the

purpose of conciseness, thus implying that the reconstruction is performed for one frequency component at a time. By adopting a global index, t, to combine the two indices (i and q), and then evaluating $p(\vec{x})$ at all the measurement locations, the sound pressure at different measurement locations can be expressed as:

$$p^{(s)} = \sum_{t=1}^{M\times N} \hat{p}_t \hat{\xi}_t^{(s)}, \tag{5.13}$$

or in a matrix form:

$$\begin{bmatrix} p^{(1)} \\ p^{(2)} \\ \cdots \end{bmatrix} = \begin{bmatrix} \xi_1^{(1)} & \xi_2^{(1)} & \cdots \\ \xi_1^{(2)} & \xi_2^{(2)} & \cdots \\ \cdots & \cdots & \cdots \end{bmatrix} \begin{bmatrix} \hat{p}_1 \\ \hat{p}_2 \\ \cdots \end{bmatrix}, \tag{5.14}$$

where $p^{(s)}$ represents the total sound field at the sth measurement location, $\hat{p}_t$ is the same as $p_i^{(q)}$ in Eq.(5.11) and $\hat{\xi}_t^{(s)}$ is the expression $\xi^{(q)}(\phi_i, \theta_i)e^{jk(r_i-1)}/r_i$ evaluated at the sth measurement location. With the relation between the measurement values and the nodal values on the unit spheres written in the form of Eq. (5.14), the nodal values, $\hat{p}_t$, can be estimated from the measurements, $p^{(s)}$, by finding a least square solution. Once the nodal values, $\hat{p}_t$, are calculated, the sound pressure at any location in the space can be predicted by a substitution of $\hat{p}_t$ into Eq.(5.12), and the sound field reconstruction is thus achieved.

It is further noted that, in this reconstruction method, the interpolation accuracy, i.e., the number of nodes on each unit sphere, is limited by the number of measurements, since the error in the least-square estimation will be large if the number of nodes (summed over all

spheres), $\hat{p}_t$, is much greater than the total number of measurements, $p^{(s)}$. Based on this consideration, the mesh grid generation algorithm in the present work was, therefore, operated with the combination of the starting polyhedron type (chosen from tetrahedron, octahedron or icosahedron) and the number of subdivision times that gives the largest total number of nodes (same grid on all spheres) that was still less than the number of measurements available.

5.3 Simulation Analysis of the Method for a Single Source

Two simulations were conducted in the present work to validate the first local-basis method developed in this chapter that uses piece-wise interpolation to reconstruct the sound field from a single source in free-space and to demonstrate the features of this method. The first simulation was aimed at reconstructing the sound field in the whole space by distributing measurement points around the source (the number of measurement being much less than the number of actual source terms used to generate the field): here it was expected that the detailed spatial variations in the radiation would not be captured, but that the overall sound field would be predicted with reasonable accuracy. The purpose of the second simulation was to illustrate an implementation that cannot be achieved by methods in which a global basis is used to describe the sound field: i.e., it is demonstrated that the sound field in a certain solid angle region can be predicted in detail by using an array of measurements that covers that region only. This capability is practically valuable in situations in which the sound radiation in only a certain view angle is of interest: e.g., in predicting the sound field of a television projected towards a viewer.

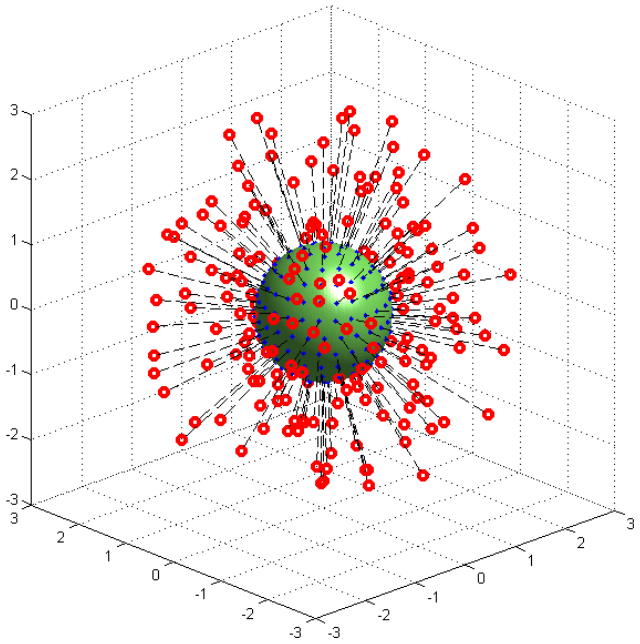

Figure 5.2. The projection of measurements onto the unit sphere.

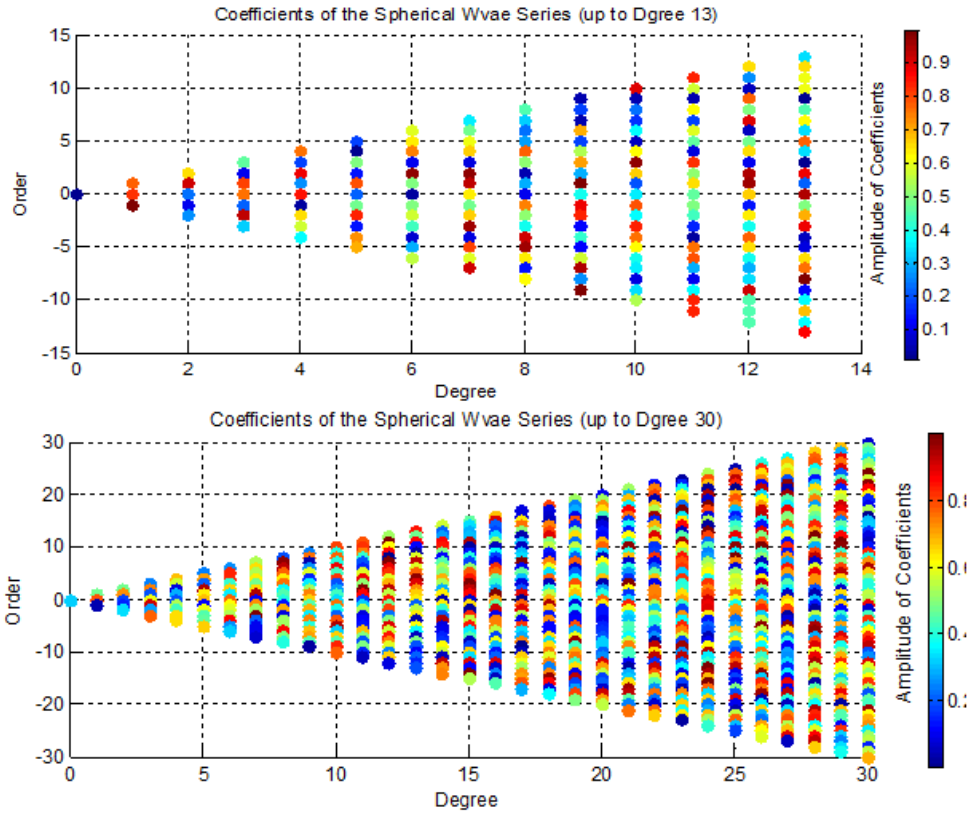

Figure 5.3. The coefficients of each spherical wave term in the actual source.

5.3.1 The Reconstruction of the Sound Field in the Whole Space

In the simulation focused on predicting the sound field in the entire space at high frequency (10 kHz was chosen as the example frequency here), 200 measurement points were placed around the origin with their angular coordinates generated by the Leopardi algorithm to ensure a relatively uniform sampling in all directions and their radii were generated from a uniform random distribution ranging from 1 to 3 m. The locations of the measurement points are illustrated in Figure 5.2. The source used in this simulation is specified in terms of the spherical wave series as in Eq. (5.1), where the coefficients in the series were generated from a uniform random distribution (from 0 to 1).

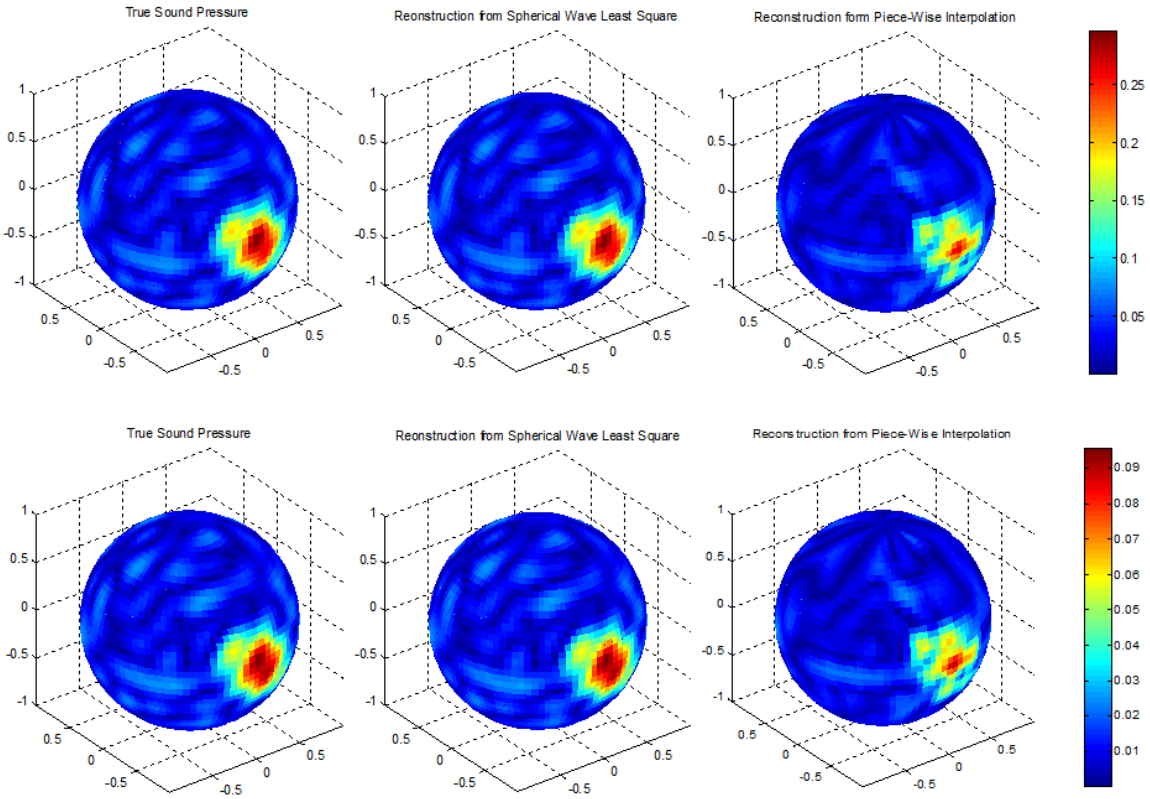

Figure 5.4. The performance comparison of the two methods when the number of actual source terms is less than the number of measurements: on the unit sphere (top) and on a sphere of $r = 3$ (bottom).

The sound field reconstruction results obtained by using both the spherical wave basis (i.e., a global basis) with a least-square method to estimate the coefficients and the piece-wise interpolation method described in Section 5.2.2 (i.e., the first local-basis method), are compared in two situations: (1) the number of terms in the actual source expression is nearly the same as the number of measurement; specifically, a source with spherical waves up to degree 13 (including 196 terms in total) was used; and (2) the number of source terms was much greater than the number of measurements (the usual case in high frequency sound radiation), where a source up to degree 30 (including 961 terms in total) was used. The coefficients of each source term in both situations are shown in Figure 5.3. To investigate the performance of the two reconstruction methods (i.e., the one using global basis and the one using local-basis), the predicted sound fields from both methods were compared with the true sound field on two surfaces: one was the unit sphere and the other was in the far field (a sphere with radius of 3 m).

Based on the performance of the two reconstruction techniques, shown in

Figure 5.4 and Figure 5.5, it can be seen that more accurate results can be obtained from the method using a spherical wave basis (a global basis) when the number of actual source terms is nearly the same as the number of measurements. However, the global basis method fails completely (i.e., gives no meaningful predictions) when the number of source terms is much greater than the number of measurements, whereas reasonable predictions, although with some detailed spatial variations being lost in the reconstruction, can still be obtained by the piece-wise interpolation method (i.e., the local-basis method). Since the latter situation is more likely to represent the case at high frequencies, it is concluded that

the local-basis method is a more suitable choice, compared with traditional methods based on using a global basis, when reconstructing the sound field at high frequencies.

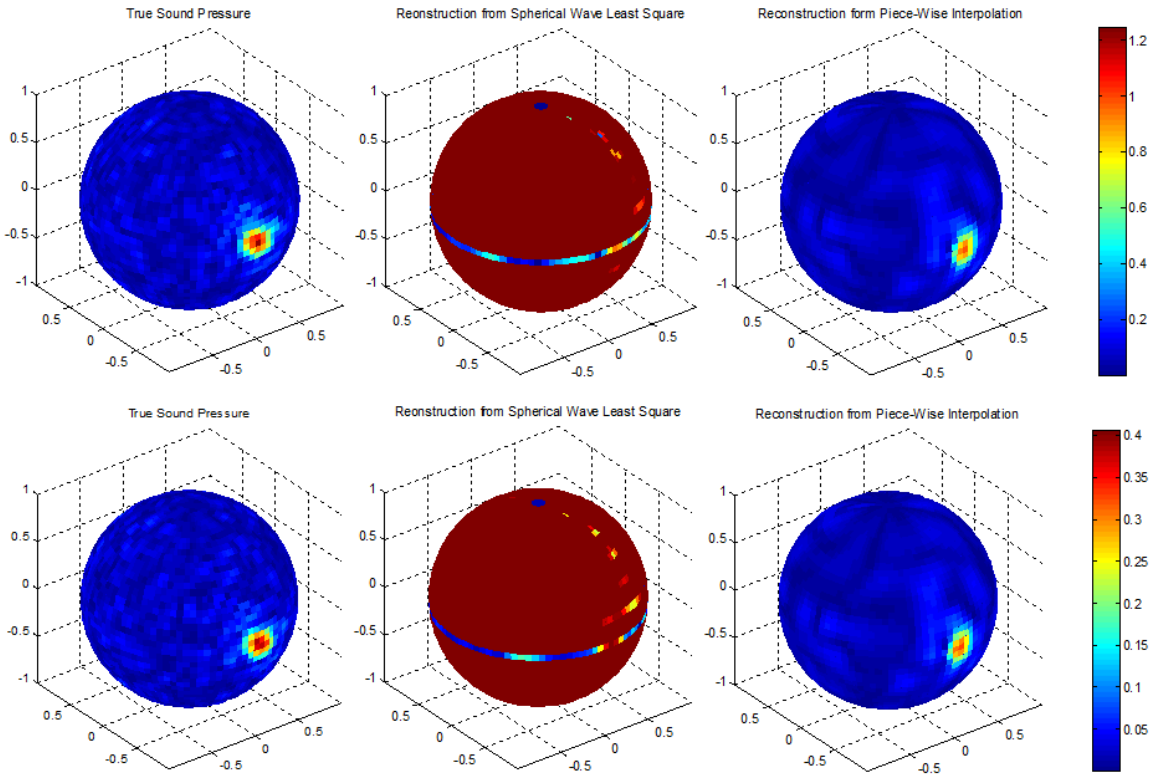

Figure 5.5. The performance comparison of the two methods when the number of actual source terms is greater than the number of measurements: on the unit sphere (top) and on a sphere of $r = 3$ (bottom).

5.3.2 The Reconstruction of the Sound Field in a Particular Region

In the previous simulation, the energy of the sound radiation was concentrated in several small, “hot-spot” solid angle regions. It is demonstrated in this second simulation that a hot-spot region can be reconstructed in detail by using measurements that cover that region only. A planar array of measurements was taken that covered the target region and the

distance from the measurement plane to the origin was 2 m (the locations of the measurements are shown in Figure 5.6). As in the previous simulation, the sound pressure in this solid angle region on the unit sphere was interpolated from the "projected" measurements. The true values and the interpolated values (shown in Figure 5.7) of the sound pressure in this region were compared on the unit sphere, which demonstrates that accurate reconstruction of sound field can be achieved (i.e., the details of the spatial variation can all be captured). It is noted here that the spacing of the measurements in the planar array is much wider than the spacing of the projections on the unit sphere, meaning that a high spatial resolution of measurements on the unit sphere can be obtained by "projection" from the widely-spaced array of measurements: i.e., this approach solves the problems, when using traditional techniques, that requires impractically small spacing of the measurement to capture the details of the sound field variations in space.

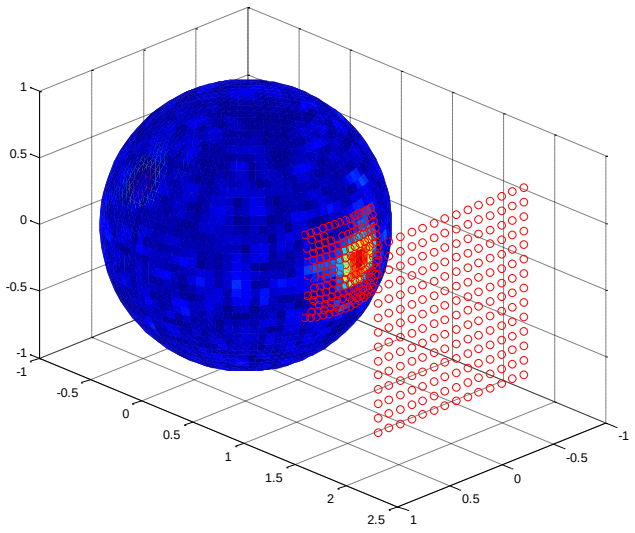

Figure 5.6. The locations of measurements used in predicting the sound field in a particular region.

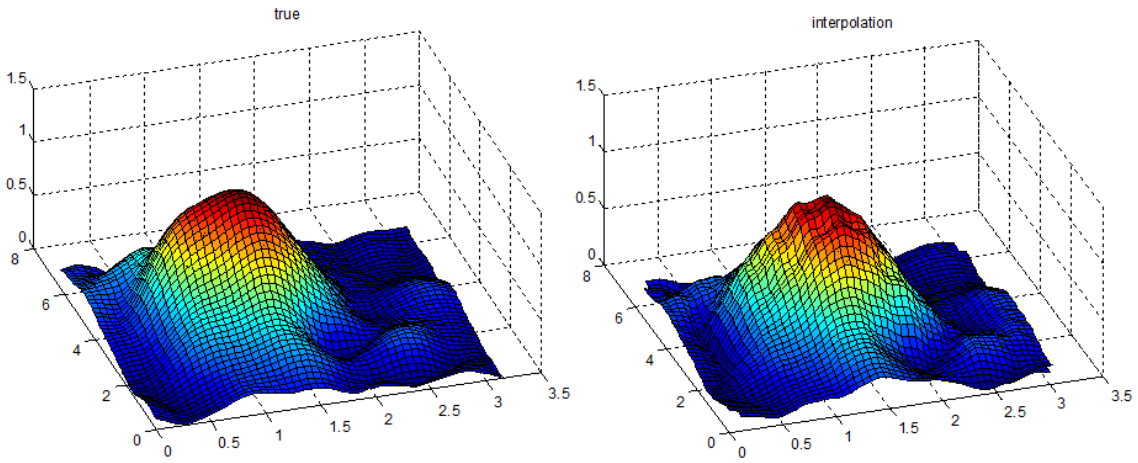

Figure 5.7. The comparison of the true and the interpolated sound field in a particular region on the unit sphere.

5.4 Simulation Analysis of the Method for Multiple Sources

For the purpose of demonstrating the validity of using the second local-basis method (described in Section 5.2.3) to reconstruct the sound field from multiple sources at high frequencies, only two sources were included in the numerical simulation presented here. As illustrated in Figure 5.8, the two source were 1 m apart from each other (located at (-0.5,0,0) and (0.5,0,0) in a Cartesian coordinate system), and the sound pressure was measured at 200 locations in the space whose distances to the origin were between 1 m and 3 m.

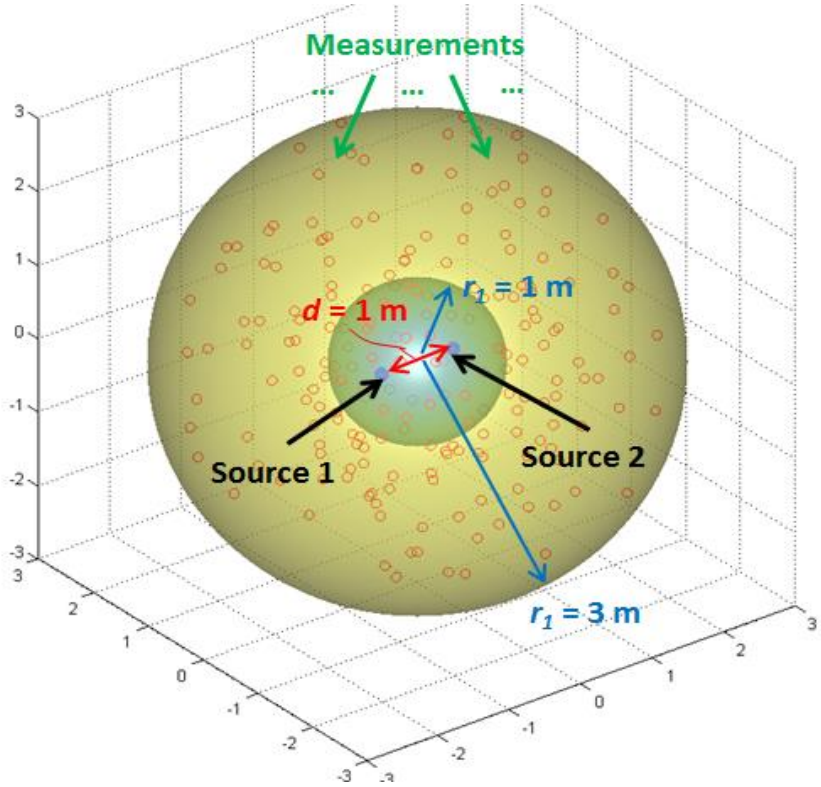

Figure 5.8. The geometry of the simulation setup (2 sources and 200 measurement locations).

To ensure that the reconstruction accuracy was not biased to any directions, the angular coordinates (spherical coordinates) of the measurement locations were generated using the Leopardi algorithm mentioned before (Leopardi, 2006) that can divide a sphere into an arbitrary number of small elements (measurement locations were chosen to be the centers of these element). The distance from each measurement location to the origin was obtained randomly from a uniform distribution ranging from 1 m to 3 m. Based on the number of measurements and sources (200 measurements and 2 sources) assumed here, the grid on the sphere around each source was, according to the criterion mentioned at the end of Section 5.2.3, generated from an octahedron subdivided twice which then includes 66 nodes on a single sphere. For the purpose of generating a sound field with a complicated

spatial directivity pattern (as usually occurs in realistic cases at high frequencies), each source was determined by a very high order spherical wave series (up to order 20) with the coefficients (both the real and the imaginary parts) of the involved source terms randomly generated from a standard normal distribution. The coefficients for both sources can be found in Figure 5.9, and then the total sound field in the simulation was generated according to Eq. (5.7). Simulation results at two representative frequencies, 8000 Hz and 15000 Hz, are presented here, which are generally considered to be in the high frequency range in usual cases.

To illustrate the accuracy of the proposed sound field prediction technique, the predicted sound pressure (the least-square solution of Eq. (5.14)) is compared with the true sound field at 500 test locations on a sphere of radius 1 m centered at the origin and at another 500 test locations on a concentric sphere with radius 3 m. The angular coordinates of these test locations were obtained from the same algorithm (Leopardi, 2006) that was used to generate the measurement locations. It is observed from these comparisons, from Figure 5.10 to Figure 5.13, that the prediction based on the proposed method can capture the general pattern of the actual sound field at high frequencies having very large spatial variations, although the result is not accurate in some angular directions. To further illustrate this observation and the spatial distribution of the prediction accuracy, the sound fields on a sphere with radius of 3 m (both actual and predicted) are plotted on a sphere (Figure 5.14). The present results are consistent with the conclusions regarding the performance of the first local-basis method demonstrated in Section 5.3. It is restated here that the purpose and the advantage of using local basis methods at high frequencies is to

be able to obtain a reconstruction of the general pattern of the sound field when its spatial variation is very large, i.e., having a complicated directivity pattern, where the traditional methods (methods using a global basis) would result in meaningless results. It is thus fair to conclude that the proposed method is a generalization, from a single source to multiple sources, of the sound field reconstruction method using local basis representations at high frequencies.

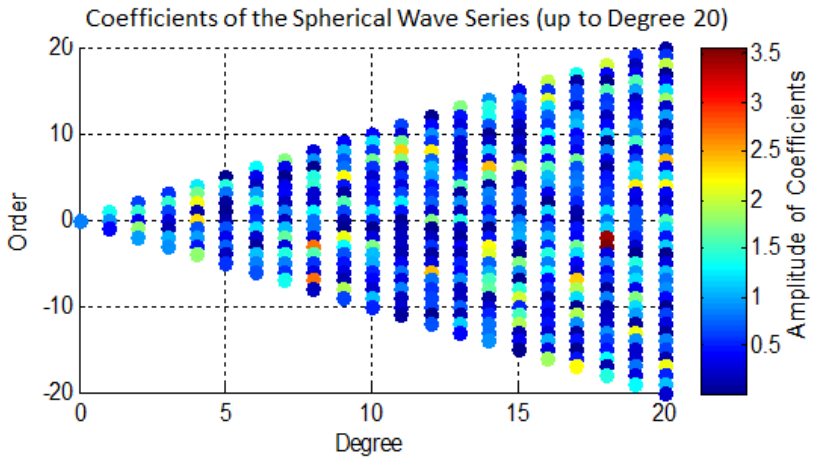

(a)

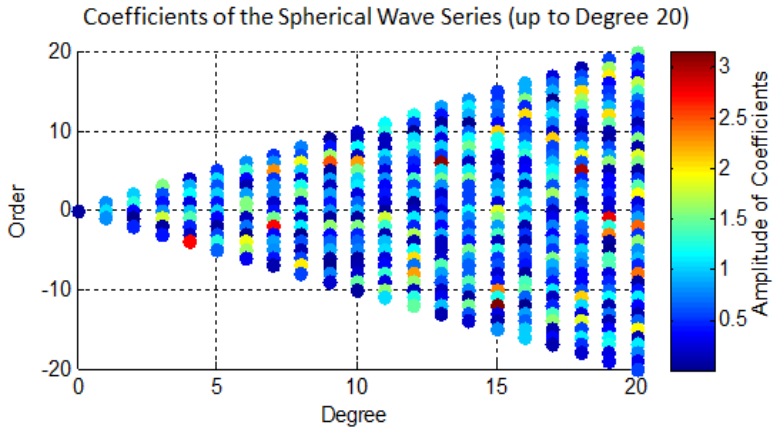

(b)

Figure 5.9. The amplitudes of the source terms in each source ((a) for Source 1 and (b) for Source 2).

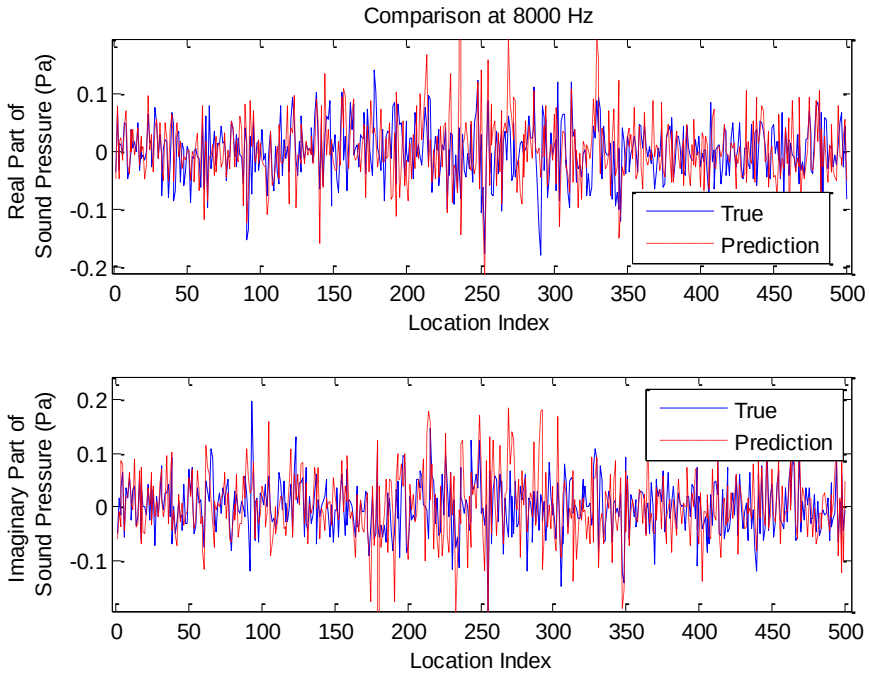

Figure 5.10. Comparison of the true and the predicted sound pressure at the sphere with radius of 1 m at 8000 Hz.

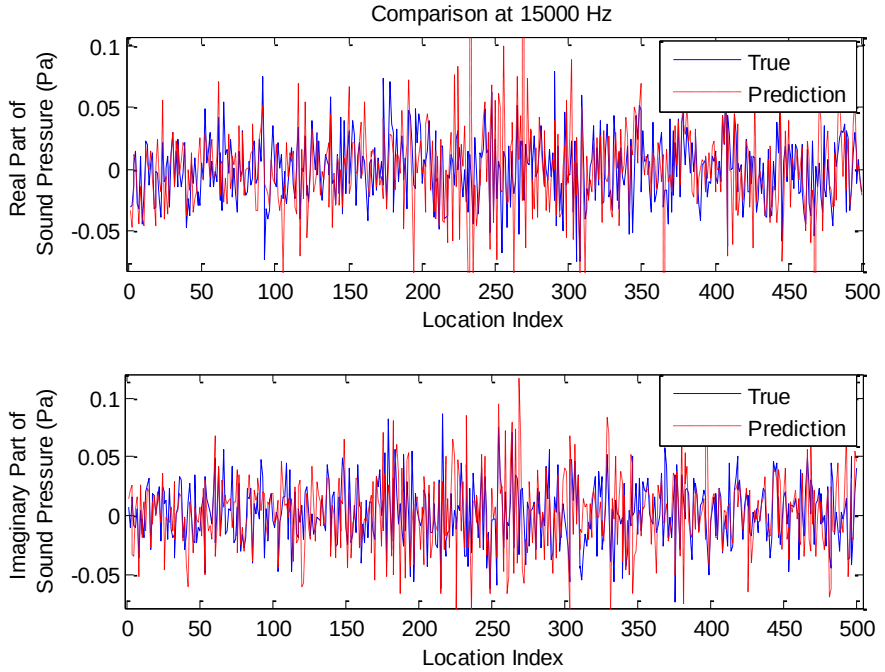

Figure 5.11. Comparison of the true and the predicted sound pressure at the sphere with radius of 1 m at 15000 Hz.

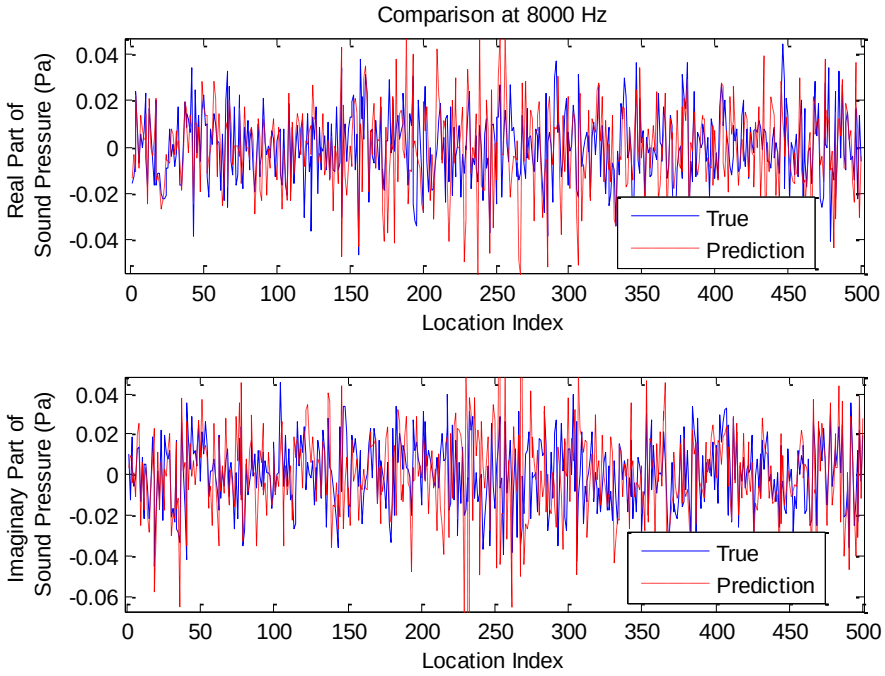

Figure 5.12. Comparison of the true and the predicted sound pressure at the sphere with radius of 3 m at 8000 Hz.

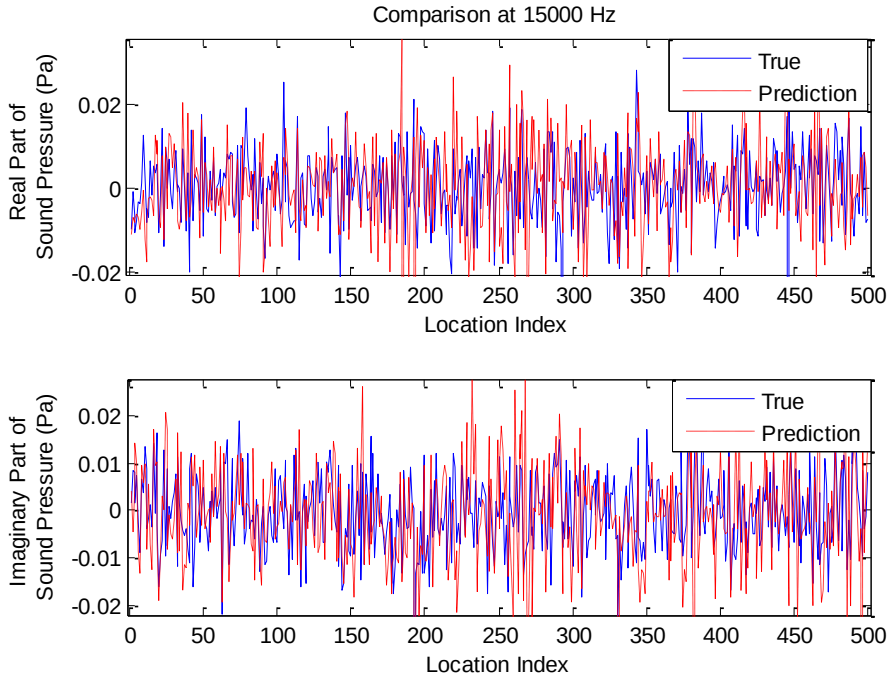

Figure 5.13. Comparison of the true and the predicted sound pressure at the sphere with radius of 3 m at 15000 Hz.

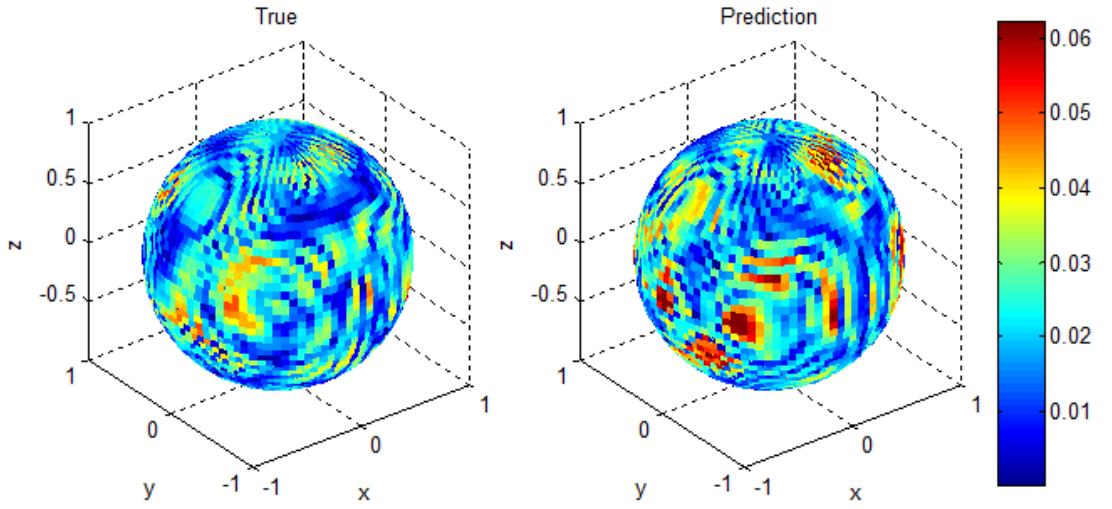

(a)

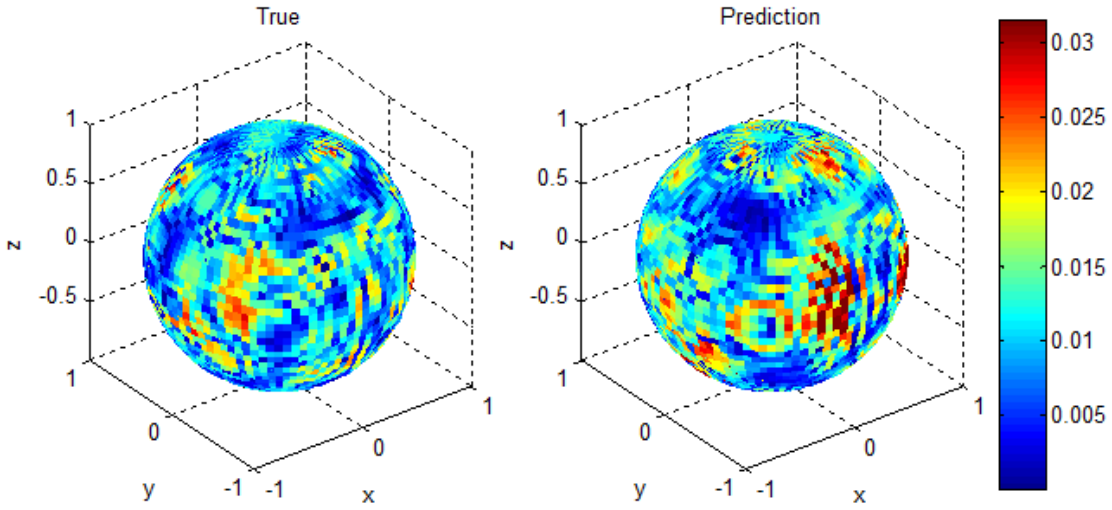

(b)

Figure 5.14. Surface plot of the actual and the predicted sound pressure on the sphere with a radius of 3 m ((a) for 8000 Hz and (b) for 15000 Hz).

5.5 Summary

To reconstruct a sound field at high frequencies where the number of measurements in practice is usually much less than the number of terms in the series required to accurately represent the field in free-space, two methods that involve the use of a local basis was

proposed and validated in the present work. The first method is limited to situations of a single source (or all sources are distributed in a small region in space), and the second method is a generalization to multiple sources. Both methods mathematically depend on an approximated expression of the sound field under the assumption of large wavenumber (i.e., high frequency) in which the radial (in spherical coordinates) dependence of the sound field can be approximated by the form e^{jkr}/r. But the two methods have different model construction processes.

In the first method, i.e., the one for a single source, the direct use of the approximated expression allows all measurements at arbitrary locations to "projected" onto the unit sphere around the source location, yielding a number of distributed measurements, and then the sound pressure distribution on the unit sphere can be interpolated from these scattered data by using piece-wise polynomials. The interpolated sound pressure on the unit sphere can then be "projected" out to predict the sound field anywhere in free space. The results from the simulations demonstrated that, when the number of terms in the actual source is nearly the same as the number of measurement, the use of a global basis, as in traditional techniques, gives more accurate predictions than the local-basis method; however, in a typical situation for high frequencies, the number of measurements is much less than that necessary to describe the spatial variation of the sound field, in which case the traditional method is likely to fail completely; in contrast, the proposed piece-wise interpolation method can still give reasonable reconstruction results. It was also demonstrated that it is possible to reconstruct the detailed sound field in certain directional

regions, if a local basis is used, by taking measurements in that region only, and the missing information from the other regions does not affect the prediction in that region.

The second local-basis method developed in this chapter is more general compared with the first method, and extends the applicability of simulating a sound field having a single source to the case of having multiple sources. Based on the derived approximate expression for the sound field, it has been shown that, at high frequencies, the sound field component from each single source can be determined by its distribution on the unit sphere centered at the associated source location. With mesh grids generated on the unit spheres around each source and interpolation applied to each sound field component from their values at the nodes of the grids, the total sound pressure at the measurement locations can be linearly related to the nodal values on the grids. By finding the least-square solution to this linear system, the nodal values can be estimated from the measurements, and thus the total sound field can be reconstructed. Simulations were carried out, at both 8000 Hz and 15000 Hz, for a case having two sources with very complicated spatial directivities, which showed that the general spatial pattern of the sound field can be reconstructed by the proposed method (giving similar performance to the previous method that is limited to one source).

CHAPTER 6. SUMMARY AND FUTURE WORKS

6.1 Summary

Motivated, primarily, by the need of fast and efficient modeling of the sound field generated by a certain source, such as an audio device, in different environments, anechoic and the room environments, in particular, a two-step simulation approach was considered in which the free-space sound field of the source is first simulated and then this result is input into a room acoustics model that predicts the sound field in a certain room environment. Such a two-step process has the advantage of conveniently simulating different room effects for the same source.

To achieve high modeling efficiency, i.e., a fast and accurate simulation, the simulation procedures in each part of the whole process were proposed mainly based on modifications and improvements to certain acoustical holography techniques. The work presented here mainly consists of three part: (1) the proposal of a free-space sources model using a series of monopoles, dipoles, quadrupoles, etc. with undetermined source locations to represent the sound radiation from a source; (2) the development of a reduced order modeling approach for room acoustics simulation in which the Equivalent Source Method in acoustical holography has been modified for sound field predictions in interior environments; and (3) a treatment for simulating the high-frequency sound field in which

the sound field is represented by functions that only describe the sound field in a certain angular region in the spherical coordinate system. Also, as a theoretical foundation for the use of multipoles to represent a sound field, the completeness property of the multipole series was mathematically proven. The linear dependence relation (more generalized than that recognized in previous literature in the acoustics area) among different multipole orders is demonstrated. These results are given in the Appendix of this document.

In the proposed free-space sound field model described in Chapter 3, the series of monopoles, dipoles, quadrupoles, etc. are used as the equivalent sources, based on the completeness properties on the multipoles, to describe the sound field. One reason for using multipoles is that it will be simpler for the forward calculation of the sound field, after the source parameters are found by solving an inverse problem, because in the forward process each source in the series can be treated as a combination of closely located monopoles. This simplifies the calculation especially when this free-space result is used as the input to different room acoustics models and there is negligible source surface scattering of the room surface reflected sound field, because, in this circumstance, only monopole sources need to be considered in the room acoustics simulation. The locations of the equivalent sources in this free-space model are not specified in the beginning and need to be determined by a nonlinear optimization procedure; a model as such is more flexible compared with the commonly used equivalent source models with fixed source locations, and it can thus be used to simulate more complicated sound fields allowing accurate predictions over a wider frequency range than the usual acoustical holography techniques. The performance of models at three different flexibility levels was investigated in a

measurement of the free-space sound field from a loudspeaker. The three flexibility levels are: the fixed-location model (sources fixed at the center of the loudspeaker for all frequencies); the collocated model (all sources have the same but undetermined location which is estimated by optimization for each frequency component with the constraint that all sources lie inside the loudspeaker); and the non-collocated model (sources of different orders can have different (undetermined) locations inside the loudspeaker but the sources of the same order have the same location). It was shown from the experimental results that, by using a multipole series up to the order of octupoles, the collocated and the non-collocated equivalent source models can be used to predict the free-space sound field accurately for the whole audible frequency range (up to 2 kHz), whereas the fixed-location mode can only produce accurate predictions up to 3 kHz. The source locations calculated from the collocated model were found to be consistent with the design of the loudspeaker since the calculated source location were at the diaphragm location for frequencies below the designed cross-over frequency of the loudspeaker, while it moves towards the tweeter location when the frequency increases and passes the cross-over frequency. Also, the collocated model can be used to visualize the sound field on the loudspeaker surface, but with an additional constraint: the equivalent source locations need to be a certain distance away from the front face of the loudspeaker. This distance threshold is application-dependent and, in the presented experimental condition, it was found that 4 cm is enough for this threshold. The predicted sound pressure distribution over the loudspeaker surface was verified with a Boundary Element Model result with a velocity boundary condition obtained from laser vibrometer measurements.

The reduced order room acoustics model, described in Chapter 4, has extended the traditional use of equivalent source models to room acoustics applications by including sources that represent both incoming and out-going wave components. The source parameters are estimated using the impedance boundary conditions on the room surfaces. Compared with the ray models or other geometric acoustics models, the proposed method is more mathematically rigorous and can be applied to situations involving finite-size sources. It is also computationally much faster than Boundary Element Models. In the preliminary simulation investigations carried out for two-dimensional room spaces, two types of room acoustics Equivalent Source Models (ESM) were developed and compared: (1) the monopole distribution ESM using one layer of monopoles inside the source surface and one layer outside the room surface; (2) a multipole ESM with the series of monopoles, dipoles etc. placed inside the source surfaces (each source has an incoming and an out-going component). From this simulation of a two-dimensional room with circular geometry it was shown that the multipole ESM can generally give more stable results because this model structure can use Truncated Singular Value Decomposition to regularize the problem with a fixed truncation parameter for all frequencies. In contrast, in the monopole distribution ESM, the regularization parameter has to be chosen from a number of techniques such as Generalized Cross Validation, which may give inaccurate results at some frequencies. Moreover the multipole ESM usually requires fewer model parameters (i.e., is more efficient) than the monopole distributions model to achieve relatively the same overall accuracy. It was also observed that for multipole ESMs, when the source order is low, the spatially averaged error for the sound field prediction is still small, but the spatial "ringing" effect is larger compared with results from models with additional higher order

sources. For the monopole distribution ESMs, there is no such gradual transition, as the number of sources decreases, from an accurate prediction to meaningless results. This means that the use of multipole ESM is offers the flexibility to balance the computational intensity and accuracy by appropriate choice of the maximum source order included in the model. For further analysis, simulations in three-dimensional rooms were performed by using the multipole ESM only, where the room involved is an Alpha cabin with relatively absorptive surfaces and the source is of a spherical shape with a part of its surface vibrating. The 3D simulation results have validated that the multipole room acoustics ESM in 3D has similar characteristics as that demonstrated in the 2D simulations. After the simulation validations, an experimental validation was also carried out with a loudspeaker in a small rectangular room (where the surface impedances were known). Based on the experimental results, the use of multipole ESM as a reduced order modeling method in room acoustics was validated, however, only when the pressure boundary condition on the source surface is given (usually through a BEM calculation), and the direct use of a free-space ESM coupled into a room acoustics ESM was not producing plausible results. Thus, so far, the experimental results only support the use of ESM as a reduced order modeling technique after a BEM calculation.

The approach described in Chapter 5, is to simulate the complicated sound field at very high frequencies when the number of measurements is much less than the number of source terms required to describe the sound field, if the usual equivalent sources are used. It was observed that if the function basis is a global basis, i.e., it describes the sound field everywhere in the space rather than only a certain region in the space (local basis), the error

in the parameter estimation is an accumulation of mismatch errors (between the true sound field and the closest prediction the chosen basis can achieve) at all the measurement locations. Based on this observation, the proposed method uses a local basis represent the sound field on a sphere. The use of this basis relies on the fact that the sound field, when described in spherical coordinates, has an approximated form of $p(\theta, \emptyset)/(kr)$ when kr is large as for high frequencies. This approximation can be used, in different ways, to generate two different local basis models: one only predicts the sound field from a single source (or source located within a single small region in space), the other is more generalized and can deal with the case of having multiple sources. If there is only one source in that space, the sound field on the unit sphere with angular coordinates the same as the measurements can be directly calculated from the measured sound field, and then the continuous function $p(\theta, \emptyset)$, can be determined by piece-wise interpolation, thus the sound field in the whole space can be predicted. However, if multiple sources exist, the sound field components from each source are combined together to produce the total sound field which is the quantity being measured. In this case, it is not possible to directly calculate each sound pressure component on the unit spheres around each corresponding source. The second local basis method solves this problem by generating a grid mesh on each of the spheres and the shape functions and the undetermined nodal values are used to describe the distribution of each sound field component on its corresponding sphere. Then the nodal values from all the unit spheres are estimated together by a least-square match to the measured sound pressure. Numerical simulations for both methods have been used to validate the use of these local basis models. It is shown that when the sound field is very complicated, as it typically is at high frequencies, and a relatively small number of

measurements are available, the traditional global basis methods produce meaningless results. In contrast, the local basis models, although they cannot predict all the details of the sound field, they can still be used to reconstruct the general directivity pattern. An additional advantage of the second method, which deals with multiple sources, is that it is straightforward to be extended so that it can be applied to an interior environment, because some of the sources can be specified as generating incoming waves without changing the approximated expression for the sound pressure at high frequencies.

6.2 Future Works

Based on the methodologies and the results presented in this document, some suggestions of possible future works are discussed here that could further improve the results or extend the applications. In Chapter 3, the proposed free-space multipole Equivalent Source Model (ESM) was validated by an experiment using a loudspeaker which is a relatively simple source, thus the applications of the multipole ESM in reconstructing the sound fields from more complicated sources, e.g., automobile engines, could be investigated in the future, where not only the spatial distribution of the sound field is more complicated, the sound field may include contributions from multiple uncorrelated sources as well. Also the model constructions described in that chapter can be straightforwardly extended to include more than one multipole series with different source locations as the equivalent sources, which could be a better modeling alternative if there exists multiple actual sources, and this application is also of interest to look into. In processing the measurement data, the errors in measuring the spatial coordinates of each microphone can, in principle, affect the model prediction accuracy, which has not been studied in detail in the present work, so an error

analysis on the spatial locations of the microphones may help provide guidance of implementing the proposed models. Similarly, rigorously speaking, a microphone measures the sound pressure on a finite area, rather than an idealized single point as in the treatment in this document, this may result in observable errors in model predictions as well, especially at high frequencies. It is, therefore, suggested to calculate the averaged sound pressure of the microphones' measurement regions and compare these averaged quantities with the measurements. In the model construction and the sound field prediction processes, the sound field from multipoles is evaluated using symbolic differentiations which is a computationally intensive method, especially for multipoles of relatively high orders. It is desired to develop some more efficient method to calculate the sound field from multipoles. One possible direction to study this is, motivated by the close relation between the multipoles and the spherical wave functions as demonstrated in the Appendix, to try to derive recursive formulas for multipoles of different orders that are analogous to the classical recursive formulas for the spherical wave functions.

Regarding to the room acoustics modeling methods described in Chapter 4, the associated experimental results, although validated the use of the equivalent source model as a reduced order modeling process, did not support the direct use of the proposed model as a room acoustics simulation method. One possible reason might be that the sound field at around 500 Hz (the frequency band that is focused on in that chapter) include a strong modal response from the rectangular room which cannot be efficiently represented by multipoles. However, there is no further evidence to support this explanation and it needs to be further verified. If the strong contribution of the room modes were verified to be the

main cause of the errors in the multipole ESM predictions, one might consider using the functions of the room's modal shapes as the equivalent sources for low frequencies. Also the effects of the room shape and the surface impedances on the model performances could be further investigated. The performance of the developed model at higher frequencies was not well demonstrated by the presented experiment results, because the room surfaces are very absorptive at higher frequencies which results in a very small room component sound field compared with the free-space component. Thus it is suggested to perform a similar experiment in the future but with less absorptive surfaces at higher frequencies, so that the room component sound field becomes more obvious and the performance of the proposed models can possibly be demonstrated. Another direction for further investigations is that an Equivalent Source Model with un-fixed source locations (similar to the one used in Chapter 3) may be applied. In such implementations, it may be worth trying to use multipoles to represent the outgoing waves (same as the presented work), but use the spherical wave function with the spherical Bessel functions of the first kind (a solution with no singularities) to represent the incoming waves, because in this way, the source locations for the incoming waves can be allowed to move within the whole room region. This is a much larger region than the region within the source surface which is the constraint that is required if the chosen equivalent sources have singularities at the source locations, such as the multipoles. By constraining the source locations inside larger region may probably result in more accurate model predictions.

In Chapter 5, the local basis methods were validated only by numerical simulations, thus the first suggestion for the future work regarding to this is to also perform an experimental

validation. In the simulation of the local-basis method for multiple sources, the mesh grids on the unit spheres around the source locations were generated by the method of polyhedral subdivisions, which results in meshes with element sizes being relatively the same all over the spheres. However, it is possible that the projected points from the measurement locations onto the unit spheres are not uniformly distributed on the spheres, or, in even worse situations, there are some nodal values on the mesh grids that are not contributing to any measurement locations. This introduces both the issue of inefficient representation of the sound field and the issue of unnecessary ill-posedness in the inverse estimation of the nodal values. Therefore it may be desired to generate non-uniform mesh grids based on the measurement locations in this local-basis method.

LIST OF REFERENCES

LIST OF REFERENCES

Abramowitz, M., & Stegun, I. A. (Eds.). (1965). *Handbook of Mathematical Functions: With Formulas, Graphs, and Mathematical Table*s. Dover Publications, New York.

Alarcão, D. (2005). Acoustic Modelling for Virtual Spaces, Ph.D. thesis, Instituto Superior Tecnico, TULisbon, Portugal.

Alfeld, P., Neamtu, M., & Schumaker, L. L. (1996). Bernstein-Bézier polynomials on spheres and sphere-like surfaces. Computer *Aided Geometric Design*, 13(4), 333-349.

Alfeld, P., Neamtu, M., & Schumaker, L. L. (1996). Fitting scattered data on sphere-like surfaces using spherical splines. *Journal of Computational and Applied Mathematics*, 73(1), 5-43.

Allen, J. B., & Berkley, D. A. (1979). Image method for efficiently simulating small-room acoustics. *The Journal of the Acoustical Society of America*, 65(4), 943-950.

Allred, J. C., & Newhouse, A. (1958). Applications of the Monte Carlo method to architectural acoustics. *The Journal of the Acoustical Society of America*, 30(1), 1-3.

Aretz, M. (2012). Combined Wave and Ray Based Room Acoustic Simulations of Small Rooms. Ph.D. Thesis, RWTH-Achen University, Germany.

Awanou, G., Lai, M. J., & Wenston, P. (2005). The multivariate spline method for scattered data fitting and numerical solutions of partial differential equations. *Wavelets and Splines: Athens 2005*, Proceedings of International Conference on Interaction between Wavelets and Splines, Athens, GA, USA, May 16-19, 2005 (pp. 24-74).

Aydin, K., & Hizal, A. (1986). On the completeness of the spherical vector wave functions. *Journal of mathematical analysis and applications*, 117(2), 428-440.

Bai, M. R. (1995). Acoustical source characterization by using recursive Wiener filtering. *The Journal of the Acoustical Society of America*, 97(5), 2657-2663.

Bajaj, C. L. (1993). Multi-dimensional Hermite interpolation and approximation for modelling and visualization. Proceedings of the IFIP TC5/WG5.2/WG5.10 CSI International Conference on Computer Graphics: Graphics Design and Visualization, Bombay, India, February 24-26, 1993 (pp. 335-348).

Beauvilain, T. A., Bolton, J. S., & Gardner, B. K. (2000). Sound cancellation by the use of secondary multipoles: Experiments. *The Journal of the Acoustical Society of America*, 107(3), 1189-1202.

Bi, C. X., & Bolton, J. S. (2012). An equivalent source technique for recovering the free sound field in a noisy environment. *The Journal of the Acoustical Society of America*, 131(2), 1260-1270.

Biot, M. A. (1968). Generalized boundary condition for multiple scatter in acoustic reflection. *The Journal of the Acoustical Society of America*, 44(6), 1616-1622.

Biot, M. A., & Tolstoy, I. (1957). Formulation of wave propagation in infinite media by normal coordinates with an application to diffraction. *The Journal of the Acoustical Society of America*, 29(3), 381-391.

Bobrovnitskii, Y. I., Mal'tsev, K. I., Ostapishin, N. M., & Panov, S. N. (1991). Acoustical model of a machine. *Soviet physics. Acoustics*, 37(6), 570-574.

Borgiotti, G. V., Sarkissian, A., Williams, E. G., & Schuetz, L. (1990). Conformal generalized near-field acoustic holography for axisymmetric geometries. *The Journal of the Acoustical Society of America*, 88(1), 199-209.

Borish, J. (1984). Extension of the image model to arbitrary polyhedra. *The Journal of the Acoustical Society of America*, 75(6), 1827-1836.

Brooks, T. F., & Humphreys, W. M. (2006). A deconvolution approach for the mapping of acoustic sources (DAMAS) determined from phased microphone arrays. *Journal of Sound and Vibration*, 294(4), 856-879.

Carslaw, H. S. (1899). Some multiform solutions of the partial differential equations of physical mathematics and their applications. Proceedings of the London Mathematical Society (vol. 30, pp. 121-163).

Chandak, A., Lauterbach, C., Taylor, M., Ren, Z., & Manocha, D. (2008). Ad-frustum: Adaptive frustum tracing for interactive sound propagation. *IEEE Transactions on Visualization and Computer Graphics*, 14(6), 1707-1722.

Chappuis, A. (1993). Small size devices for accurate acoustical measurements of materials and parts used in automobiles (No. 931266). SAE Technical Paper.

Chen, L. H., & Schweikert, D. G. (1963). Sound radiation from an arbitrary body. *The Journal of the Acoustical Society of America*, 35(10), 1626-1632.

Cho, Y. T., Bolton, J. S., & Hald, J. (2005). Source visualization by using statistically optimized near-field acoustical holography in cylindrical coordinates. *The Journal of the Acoustical Society of America*, 118(4), 2355-2364.

Christensen, C. L., & Rindel, J. H. (2005). A new scattering method that combines roughness and diffraction effects. In Forum Acousticum, Budapest, Hungary, May 2005.

Coleman, T. F., & Li, Y. (1996). An interior trust region approach for nonlinear minimization subject to bounds. *SIAM Journal on optimization*, 6(2), 418-445.

Colton, D., & Kress, R. (2013). *Inverse Acoustic and Electromagnetic Scattering Theory* (Applied Mathematical Sciences, Vol. 93), 3rd Edition, Springer, New York, Heidelberg, Dordrecht, London.

Copley, L. G. (1968). Fundamental results concerning integral representations in acoustic radiation. *The journal of the acoustical society of America*, 44(1), 28-32.

Cox, T. J., Dalenback, B. I., D'Antonio, P., Embrechts, J. J., Jeon, J. Y., Mommertz, E., & Vorländer, M. (2006). A tutorial on scattering and diffusion coefficients for room acoustic surfaces. *Acta Acustica united with Acustica*, 92(1), 1-15.

Dalenbäck, B. I. L. (1996). Room acoustic prediction based on a unified treatment of diffuse and specular reflection. *The Journal of the Acoustical Society of America*, 100(2), 899-909.

Doicu A., Eremin Y. & Wriedt T (2000). *Acoustic & Electromagnetic Scattering Analysis Using Discrete Sources*. Academic Press, San Diego, San Francisco, New York, Boston, London, Sydney, Tokyo.

Duraiswami, R., Zotkin, D. N., & Gumerov, N. A. (2007). Fast evaluation of the room transfer function using multipole expansion. *IEEE Transactions on Audio, Speech, and Language Processing*, 15(2), 565-576.

Fahnline, J. B., & Koopmann, G. H. (1991). A numerical solution for the general radiation problem based on the combined methods of superposition and singular-value decomposition. *The Journal of the Acoustical Society of America*, 90(5), 2808-2819.

Fekete, G. (1990, October). Rendering and managing spherical data with sphere quadtrees. Proceedings of the 1st conference on Visualization'90, San Francisco, CA, 1990 (pp. 176-186).

Filippi, P. J. T. (1977). Layer potentials and acoustic diffraction. *Journal of Sound and Vibration*, 54(4), 473-500.

Fish, J., & Belytschko, T. (2007). *A First Course in Finite Elements*. John Wiley & Sons.

Funkhouser, T., Tsingos, N., Carlbom, I., Elko, G., Sondhi, M., West, J. E., ... & Ngan, A. (2004). A beam tracing method for interactive architectural acoustics. *The Journal of the Acoustical Society of America*, 115(2), 739-756.

Gibbs, B. M., & Jones, D. K. (1972). A simple image method for calculating the distribution of sound pressure levels within an enclosure. *Acta Acustica united with Acustica*, 26(1), 24-32.

Gilbert, E. N. (1981). An iterative calculation of auditorium reverberation. *The Journal of the Acoustical Society of America*, 69(1), 178-184.

Golub, G. H., Heath, M., & Wahba, G. (1979). Generalized cross-validation as a method for choosing a good ridge parameter. *Technometrics*, 21(2), 215-223.

Gomes, J., & Hansen, P. C. (2008). A study on regularization parameter choice in near-field acoustical holography. *The Journal of the Acoustical Society of America*, 123(5), 3385-3385.

Hald, J. (1989). STSF–a unique technique for scan-based Near-field Acoustic Holography without restrictions on coherence. Brüel & Kjaer Technical Review, 1, 1-50.

Hald, J. (2003). Patch nearfield acoustical holography using a new statistically optimal method. Proceedings of INTER-NOISE Conference 2003, Seogwipo, Korea, August 25-28, 2003, (pp. 2203-2210). Institute of Noise Control Engineering.

Hald, J. (2005). Surface microphone, NAH and Beamforming using the same array, SONAH. Brüel & Kjaer Technical Review, 1, 40-50.

Hald, J. (2009). Basic theory and properties of statistically optimized near-field acoustical holography. *The Journal of the Acoustical Society of America*, 125(4), 2105-2120.

Hald, J. (2014). Wideband acoustical holography. Proceedings of IINTER-NOISE Conference 2014, Melbourne, Australia, November 16-19, 2014 (pp. 308-320). Institute of Noise Control Engineering.

Hald, J., & Gomes, J. (2006, December). A comparison of two patch NAH methods. Proceedings of IINTER-NOISE Conference 2006, Honolulu, Hawaii, December 3-6, 2006 (pp. 1455-1464). Institute of Noise Control Engineering.

Hansen, P. C. (1988). Computation of the singular value expansion. *Computing*, 40(3), 185-199.

Hansen, P. C. (1992). Analysis of discrete ill-posed problems by means of the L-curve. *SIAM Review*, 34(4), 561-580.

Hansen, P. C. (1998). *Rank-Deficient and Discrete Ill-Posed Problems: Numerical Aspects of Linear Inversion*. SIAM Monographs on Mathematical Modeling and Computation, Philadelphia, PA.

Hansen, P. C., Kilmer, M. E., & Kjeldsen, R. H. (2006). Exploiting residual information in the parameter choice for discrete ill-posed problems. *BIT Numerical Mathematics*, 46(1), 41-59.

Hansen, P. C., & O'Leary, D. P. (1993). The use of the L-curve in the regularization of discrete ill-posed problems. *SIAM Journal on Scientific Computing*, 14(6), 1487-1503.

Hanson, R. J. (1971). A numerical method for solving Fredholm integral equations of the first kind using singular values. *SIAM Journal on Numerical Analysis*, 8(3), 616-622.

Haviland, J. K., & Thanedar, B. D. (1973). Monte Carlo applications to acoustical field solutions. *The Journal of the Acoustical Society of America*, 54(6), 1442-1448.

Heckbert, P. S., & Hanrahan, P. (1984). Beam tracing polygonal objects. Proceedings of the 11th Conference of Computer Graphics and Interactive Techniques, New York, January, 1984, (pp. 119–127).

Henriquez, V. C., & Juhl, P. M. (2010). OpenBEM-An open source boundary element method software in acoustics. Proceedings of IINTER-NOISE Conference 2010, Lisbon, Portugal, June 13-16, 2010 (pp. 5873-5882). Institute of Noise Control Engineering.

Jeans, R., & Mathews, I. C. (1992). The wave superposition method as a robust technique for computing acoustic fields. *The Journal of the Acoustical Society of America,* 92(2), 1156-1166.

Johnson. D. H. & Dudgeon D. E. (1993). Array Signal Processing: Concepts and Techniques. PTR Prentice Hall, Englewood Cliffs, NJ.

Keller, J. B. (1962). Geometrical theory of diffraction. *Journal of the Optical Society of America*, 52(2), 116-130.

Kim, Y. J., Bolton, J. S., & Kwon, H. S. (2004). Partial sound field decomposition in multireference near-field acoustical holography by using optimally located virtual references. *The Journal of the Acoustical Society of America*, 115(4), 1641-1652.

Kim, B. K., & Ih, J. G. (1996). On the reconstruction of the vibro-acoustic field over the surface enclosing an interior space using the boundary element method. *The Journal of the Acoustical Society of America*, 100(5), 3003-3016.

Kim, G. T., & Lee, B. H. (1990). 3-D sound source reconstruction and field reprediction using the Helmholtz integral equation. *Journal of Sound and Vibration*, 136(2), 245-261.

Koopmann, G. H., Song, L., & Fahnline, J. B. (1989). A method for computing acoustic fields based on the principle of wave superposition. *The Journal of the Acoustical Society of America*, 86(6), 2433-2438.

Koutsouris, G. I., Brunskog, J., Jeong, C. H., & Jacobsen, F. (2013). Combination of acoustical radiosity and the image source method. *The Journal of the Acoustical Society of America*, 133(6), 3963-3974.

Kouyoumjian, R. G., & Pathak, P. H. (1974). A uniform geometrical theory of diffraction for an edge in a perfectly conducting surface. Proceedings of the IEEE, 62(11), 1448-1461.

Krokstad, A., Strom, S., & Sørsdal, S. (1968). Calculating the acoustical room response by the use of a ray tracing technique. *Journal of Sound and Vibration*, 8(1), 118-125.

Kuttruff, H. (1995). A simple iteration scheme for the computation of decay constants in enclosures with diffusely reflecting boundaries. *The Journal of the Acoustical Society of America*, 98(1), 288-293.

Kuttruff, H. (1997). Energetic sound propagation in rooms. *Acta Acustica united with Acustica*, 83(4), 622-628.

Kuttruff, H. (2000). *Room Acoustics*. 5th Edition Taylor & Francis, New York.

Kwon, H. S., & Kim, Y. H. (1995). Minimization of bias error due to windows in planar acoustic holography using a minimum error window. *The Journal of the Acoustical Society of America*, 98(4), 2104-2111.

Lai, M. J. (2007). Multivariate splines for data fitting and approximation. Proceedings of Approximation Theory XII, San Antonio, TX, March, 4-8, 2007 (pp. 210-228).

Langrenne, C., Melon, M., & Garcia, A. (2007). Boundary element method for the acoustic characterization of a machine in bounded noisy environment. *The Journal of the Acoustical Society of America*, 121(5), 2750-2757.

Le Bot, A., & Bocquillet, A. (2000). Comparison of an integral equation on energy and the ray-tracing technique in room acoustics. *The Journal of the Acoustical Society of America*, 108(4), 1732-1740.

Lee, M., & Bolton, J. S. (2005). Patch near-field acoustical holography in cylindrical geometry. *The Journal of the Acoustical Society of America*, 118(6), 3721-3732.

Lee, M., & Bolton, J. S. (2006). Scan-based near-field acoustical holography and partial field decomposition in the presence of noise and source level variation. *The Journal of the Acoustical Society of America,* 119(1), 382-393.

Lee, D. T., & Schachter, B. J. (1980). Two algorithms for constructing a Delaunay triangulation. *International Journal of Computer & Information Sciences*, 9(3), 219-242.

Lehmann, E. A., & Johansson, A. M. (2008). Prediction of energy decay in room impulse responses simulated with an image-source model. *The Journal of the Acoustical Society of America,* 124(1), 269-277.

Lehnert, H. (1993). Systematic errors of the ray-tracing algorithm. *Applied Acoustics*, 38(2), 207-221.

Leopardi, P. (2006). A partition of the unit sphere into regions of equal area and small diameter. *Electronic Transactions on Numerical Analysis*, 25(12), 309-327.

Lewers, T. (1993). A combined beam tracing and radiant exchange computer model of room acoustics. *Applied Acoustics,* 38(2), 161-178.

Liu, Y. (2011). Sound Field Reconstruction and its Application in Loudspeaker Sound Radiation Prediction. Master of Science in Mechanical Engineering Thesis, Purdue University, West Lafayette, IN, USA.

Loyau, T., Pascal, J. C., & Gaillard, P. (1988). Broadband acoustic holography reconstruction from acoustic intensity measurements. I: Principle of the method. *The Journal of the Acoustical Society of America,* 84(5), 1744-1750.

Lylloff, O., Fernández-Grande, E., Agerkvist, F., Hald, J., Roig, E. T., & Andersen, M. S. (2015). Improving the efficiency of deconvolution algorithms for sound source localization. *The Journal of the Acoustical Society of America,* 138(1), 172-180.

Martin, P. A. (1982). Acoustic scattering and radiation problems, and the null-field method. *Wave Motion,* 4(4), 391-408.

Martin, V., & Guignard, T. (2006). Image-source method and truncation of a series expansion of the integral solution—Case of an angular sector in two dimensions. *The Journal of the Acoustical Society of America,* 120(2), 597-610.

Maynard, J. D., Williams, E. G., & Lee, Y. (1985). Nearfield acoustic holography: I. Theory of generalized holography and the development of NAH. *The Journal of the Acoustical Society of America,* 78(4), 1395-1413.

McGovern, S. G. (2009). Fast image method for impulse response calculations of box-shaped rooms. *Applied Acoustics,* 70(1), 182-189.

Mechel, F. P. (2002). Improved mirror source method in room acoustics. *Journal of Sound and Vibration,* 256(5), 873-940.

Mehta, M. L., & Mulholland, K. A. (1976). Effect of non-uniform distribution of absorption on reverberation time. *Journal of Sound and Vibration,* 46(2), 209-224.

Millar, R. F. (1983). On the completeness of sets of solutions to the Helmholtz equation. *IMA Journal of Applied Mathematics*, 30(1), 27-37.

Mintzer, D. (1950). Transient sounds in rooms. *The Journal of the Acoustical Society of America*, 22(3), 341-352.

Moore, G. R. (1984). An Approach to the Analysis of Sound in Auditoria: Model Design and Computer Implementation. Ph.D. Thesis, University of Cambridge.

Morse, P. M., & Feshbach, H. (1953). *Methods of theoretical Physics Part II*. McGraw-Hill, New York, Tronoto, London.

Morse, P. M., & Ingard, K. U. (1968). *Theoretical Acoustics.* Princeton University Press, Princeton, NJ.

Navarro, J. M., Jacobsen, F., Escolano, J., & López, J. J. (2010). A theoretical approach to room acoustic simulations based on a radiative transfer model. *Acta Acustica united with Acustica*, 96(6), 1078-1089.

Nicodemus, F. E. (1965). Directional reflectance and emissivity of an opaque surface. *Applied optics*, 4(7), 767-775.

Nelson, P. A., & Yoon, S. H. (2000). Estimation of acoustic source strength by inverse methods: Part I, conditioning of the inverse problem. *Journal of Sound and Vibration*, 233(4), 639-664.

Nosal, E. M., Hodgson, M., & Ashdown, I. (2004). Improved algorithms and methods for room sound-field prediction by acoustical radiosity in arbitrary polyhedral rooms. *The Journal of the Acoustical Society of America*, 116(2), 970-980.

Ochmann, M. (1992). Calculation of sound radiation from complex structures using the multipole radiator synthesis with optimized source locations. Proceedings of the Second International Congress on Recent Developments in Air-and Structure-Borne Sound and Vibration, Auburn, AL, USA, March 4-6, 1992 (pp. 1187-1194).

Ochmann, M. (1995). The source simulation technique for acoustic radiation problems. *Acta Acustica united with Acustica,* 81(6), 512-527.

Ochmann, M. (1999). The full-field equations for acoustic radiation and scattering. *The Journal of the Acoustical Society of America,* 105(5), 2574-2584.

Phillips, D. L. (1962). A technique for the numerical solution of certain integral equations of the first kind. *Journal of the ACM*, 9(1), 84-97.

Pierce, A. D. (1974). Diffraction of sound around corners and over wide barriers. *The Journal of the Acoustical Society of America,* 55(5), 941-955.

Pierce, A. D. (1989). *Acoustics: an Introduction to its Physical Principles and Applications.* Acoustical Society of America through the American Institute of Physics, Melville, NY.

Raveendra, S. T., Vlahopoulos, N., & Glaves, A. (1998). An indirect boundary element formulation for multi-valued impedance simulation in structural acoustics. *Applied Mathematical Modelling,* 22(6), 379-393.

Rayess, N., & Wu, S. F. (2000). Experimental validations of the HELS method for reconstructing acoustic radiation from a complex vibrating structure. *The Journal of the Acoustical Society of America*, 107(6), 2955-2964.

Rayleigh, J. W. S. (1945). *The Theory of Sound, Volume II.* Dove Publications, New York.

Renka, R. J. (1984). Interpolation of data on the surface of a sphere. *ACM Transactions on Mathematical Software (TOMS)*, 10(4), 417-436.

Rindel, J. H. (1986). Attenuation of sound reflections due to diffraction. Proceedings of Nordic Acoustical Meeting, NAM ’86, Aalborg, Denmark, August 20-22, 1986 (pp. 257-260).

Rindel, J. H. (2000). The use of computer modeling in room acoustics. *Journal of Vibroengineering*, 3(4), 41-72.

Rowell, M. A., & Oldham, D. J. (1995). Determination of the directivity of a planar noise source by means of near field acoustical holography, 1: theoretical background. *Journal of sound and vibration,* 180(1), 99-118.

Saijyou, K., & Uchida, H. (2004). Data extrapolation method for boundary element method-based near-field acoustical holography. *The Journal of the Acoustical Society of America*, 115, 785.

Sakurai, Y., & Nagata, K. (1981). Sound reflections of a rigid plane panel and of the" live end" composed by those panels. *Journal of the Acoustical Society of Japan* (E), 2(1), 5-14.

Sarkissian, A. (1991). Acoustic radiation from finite structures. *The Journal of the Acoustical Society of America*, 90(1), 574-578.

Sarkissian, A. (2005). Method of superposition applied to patch near-field acoustic holography. *The Journal of the Acoustical Society of America*, 118(2), 671-678.

Sayhi, M. N., Ousset, Y., & Verchery, G. (1981). Solution of radiation problems by collocation of integral formulations in terms of single and double layer potentials. *Journal of Sound and vibration*, 74(2), 187-204.

Schenck, H. A. (1968). Improved integral formulation for acoustic radiation problems. *The Journal of the Acoustical Society of America,* 44(1), 41-58.

Schroeder, M. R. (1970). Digital simulation of sound transmission in reverberant spaces. *The Journal of the Acoustical Society of America*, 47(2A), 424-431.

Shames, I. H., & Dym, C. L. (1995). *Energy and Finite Element Methods in Structural Mechanics.* SI Units Edition, New Age International Publishers, New Delhi, India.

Siltanen, S., Lokki, T., Kiminki, S., & Savioja, L. (2007). The room acoustic rendering equation. *The Journal of the Acoustical Society of America*, 122(3), 1624-1635.

Siltanen, S., Lokki, T., & Savioja, L. (2009). Frequency domain acoustic radiance transfer for real-time auralization. *Acta Acustica united with Acustica,* 95(1), 106-117.

Standard, I. S. O. (1998) Determination of sound absorption coefficient and impedance in impedance tubes, Part 1: Transfer-function method. ISO 10534-2, International Standardization Organization, 1998, pp. 11-15.

Stephenson, U. M. (1996). Quantized pyramidal beam tracing-a new algorithm for room acoustics and noise immission prognosis. *Acta Acustica united with Acustica,* 82(3), 517-525.

Stephenson, U. M. (2006). Analytical derivation of a formula for the reduction of computation time by the voxel crossing technique used in room acoustical simulation. *Applied Acoustics*, 67(10), 959-981.

Svensson, U. P., Fred, R. I., & Vanderkooy, J. (1999). An analytic secondary source model of edge diffraction impulse responses. *The Journal of the Acoustical Society of America*, 106(5), 2331-2344.

Tenenbaum, R. A., Camilo, T. S., Torres, J. C. B., & Gerges, S. N. (2007). Hybrid method for numerical simulation of room acoustics with auralization: part 1-theoretical and numerical aspects. *Journal of the Brazilian Society of Mechanical Sciences and Engineering*, 29(2), 211-221.

Tikhonov, A. (1963). Solution of incorrectly formulated problems and the regularization method. *Soviet Math. Dokl*, 4, 1035-1038.

Toltoy, I. (1973), *Wave Propagation*, McGraw-Hill.

Torres, R. R., Svensson, U. P., & Kleiner, M. (2001). Computation of edge diffraction for more accurate room acoustics auralization. *The Journal of the Acoustical Society of America*, 109(2), 600-610.

Tsingos, N., Funkhouser, T., Ngan, A., & Carlbom, I. (2001). Modeling acoustics in virtual environments using the uniform theory of diffraction. Proceedings of the 28th Annual

Conference on Computer Graphics and Interactive Techniques, Los Angeles, CA, USA, August 12-17, 2001 (pp. 545-552).

Tsingos, N., & Gascuel, J. D. (1998). Fast rendering of sound occlusion and diffraction effects for virtual acoustic environments. Proceedings of the Audio Engineering Society 104th Convention, Amsterdam, the Netherlands, May16-19, 1998 (pp. 4-7).

Twersky, V. (1957). On scattering and reflection of sound by rough surfaces. *The Journal of the Acoustical Society of America*, 29(2), 209-225.

Valdivia, N., & Williams, E. G. (2004). Implicit methods of solution to integral formulations in boundary element method based nearfield acoustic holography. *The Journal of the Acoustical Society of America*, 116(3), 1559-1572.

Van Genechten, B., Pluymers, B., Vandepitte, D., & Desmet, W. (2009). A hybrid wave based-modally reduced finite element method for the efficient analysis of low-and mid-frequency car cavity acoustics. *SAE International Journal of Passenger Cars-Mechanical Systems*, 2(1), 1494-1504.

Van Hal, B., Desmet, W., Vandepitte, D., & Sas, P. (2003). A coupled finite element–wave based approach for the steady-state dynamic analysis of acoustic systems. *Journal of Computational Acoustics*, 11(02), 285-303.

Van Maercke, D. (1986). Simulation of sound fields in time and frequency domain using a geometrical model. Proceeding of the 12th International Congress of Acoustics. (ICA 1986), Toronto, Canada, July 24-31, 1986.

Varah, J. M. (1973). On the numerical solution of ill-conditioned linear systems with applications to ill-posed problems. *SIAM Journal on Numerical Analysis*, 10(2), 257-267.

Veronesi, W. A., & Maynard, J. D. (1989). Digital holographic reconstruction of sources with arbitrarily shaped surfaces. *The Journal of the Acoustical Society of America*, 85(2), 588-598.

von Estorff, O. (Ed.). (2000). *Boundary Elements in Acoustics: Advances and Applications*. Wit Press, Southampton.

Vorländer, M. (1989). Simulation of the transient and steady-state sound propagation in rooms using a new combined ray-tracing/image-source algorithm. *The Journal of the Acoustical Society of America*, 86(1), 172-178.

Vorländer, M. (2008). *Auralization: Fundamentals of Acoustics, Modelling, Simulation, Algorithms and Acoustic Virtual Reality* 1st Edition, Springer.

Vorländer, M., & Mommertz, E. (2000). Definition and measurement of random-incidence scattering coefficients. *Applied Acoustics*, 60(2), 187-199.

Wahba, G. (1977). Practical approximate solutions to linear operator equations when the data are noisy. *SIAM Journal on Numerical Analysis*, 14(4), 651-667.

Walsh, J. P. (1980). The design of Godot: A system for computer-aided room acoustics modeling and simulation. Proceeding of the 10th International Congress of Acoustics. (ICA 1980), Sydney, Australia, July 9-16, 1980.

Wang, Z., & Wu, S. F. (1997). Helmholtz equation–least-squares method for reconstructing the acoustic pressure field. *The Journal of the Acoustical Society of America*, 102(4), 2020-2032.

Welch, P. (1967). The use of fast Fourier transform for the estimation of power spectra: a method based on time averaging over short, modified periodograms. *Audio and Electroacoustics, IEEE Transactions*, 15(2), 70-73.

Williams, E. G. (1999). Fourier Acoustics: Sound Radiation and Nearfield Acoustical Holography. Academic Press.

Williams, E. G. (2001). Regularization methods for near-field acoustical holography. *The Journal of the Acoustical Society of America*, 110(4), 1976-1988.

Williams, E. G., Dardy, H. D., & Washburn, K. B. (1987). Generalized nearfield acoustical holography for cylindrical geometry: theory and experiment. *The Journal of the Acoustical Society of America*, 81(2), 389-407.

Williams, E. G., Houston, B. H., & Bucaro, J. A. (1989). Broadband nearfield acoustical holography for vibrating cylinders. *The Journal of the Acoustical Society of America*, 86(2), 674-679.

Williams, E. G., Houston, B. H., & Herdic, P. C. (2003). Fast Fourier transform and singular value decomposition formulations for patch nearfield acoustical holography. *The Journal of the Acoustical Society of America*, 114(3), 1322-1333.

Williams, E. G., & Maynard, J. D. (1982). Numerical evaluation of the Rayleigh integral for planar radiators using the FFT. *The Journal of the Acoustical Society of America*, 72(6), 2020-2030.

Williams, E. G., Maynard, J. D., & Skudrzyk, E. (1980). Sound source reconstructions using a microphone array. *The Journal of the Acoustical Society of America*, 68(1), 340-344.

Wu, S. F. (2008). Methods for reconstructing acoustic quantities based on acoustic pressure measurements. *The Journal of the Acoustical Society of America*, 124(5), 2680-2697.

Wu, S. F., & Yu, J. (1998). Reconstructing interior acoustic pressure fields via Helmholtz equation least-squares method. *The Journal of the Acoustical Society of America*, 104(4), 2054-2060.

Yoon, S. H., & Nelson, P. A. (2000). Estimation of acoustic source strength by inverse methods: Part II, experimental investigation of methods for choosing regularization parameters. *Journal of sound and vibration*, 233(4), 665-701.

APPENDIX

APPENDIX

COMPLETENESS AND LINEAR DEPENDENCE OF MULTIPOLES

A.1 The Definition of (Cartesian) Multipoles

The "multipole" terminology has been used to refer to different source series in the literature; some authors use it to indicate spherical wave series (i.e. the spherical Hankel functions times spherical harmonics), whereas it sometimes refers to the series of monopole, dipoles, quadrupoles, etc. Here, the latter meaning is adopted, as in most acoustics texts, and in order to avoid misinterpretation, the terminology Cartesian multipole is used. Note that each term in the spherical wave series is a product of solutions to equations of the Sturm-Liouville type, which are themselves generated by applying separation of variables to the Helmholtz equation, and they are thus known to be a complete and orthogonal basis for representing solutions of the Helmholtz equation. However, Cartesian multipoles, although closely related to the spherical waves, are not generated from Sturm-Liouville equations, and their completeness property has not been proven so far, which was the main objective in the present work. Mathematically, the (Cartesian) multipole of order n, is defined as the nth order partial derivative of the Green's function of the Helmholtz equation. Thus a nth order multipole, Ψ_n, can be expressed as: $\frac{\partial^n}{\partial x^{i_1} y^{i_2} z^{i_3}} G$, with

$i_1 + i_2 + i_3 = n$, where G satisfies $\nabla^2 G + k^2 G = \delta(\vec{x})$, and k is the wavenumber. In 2D cases, no differentiation in the z-direction is involved, i.e., $i_3 = 0$. .

The determination of the number of multipoles in each order is a standard combination-with-repetition problem: i.e., the function G is differentiated n times, and each time one direction is chosen from three different directions (i.e., the x, y or z directions) and the order in which the differentiation is performed does not matter. In 2D cases, there are only two directions to choose from. Thus the number of multipoles in each order can be calculated as:

$$N(n,d) = \begin{cases} 1 \quad , & n = 0 \\ C_{n+d-1}^{n} , & n > 0 \end{cases} \tag{1}$$

where C_a^b denotes the combination number resulting from choosing b out of a, n is the source order and d = 2 or 3 for the 2D and 3D cases, respectively.

A.2 The Proof of the Completeness of the Cartesian Multipole Series

The proof of the completeness of the Cartesian multipole series is based on the classic result that the spherical wave (cylindrical wave for 2D cases) series is complete in representing a solution to the Helmholtz equation. More specifically, it is known that there exists a spherical (or cylindrical) wave that converges to any solution of the Helmholtz equation in the L^2 sense, for a C^2 boundary surface (Doicu, et al., 2000) (Millar, 1983) or, more generally, for Lyapunov surfaces (Ochmann, 1995). It is generally agreed in the field

of acoustics that the Cartesian multipole series and the spherical wave (or cylindrical wave) series span the same space, and thus the multipole series is complete. However, no rigorous mathematical proof has been presented for this statement: instead, this equivalence is usually illustrated by explicitly working out the expressions for monopole, dipoles and quadrupoles, and comparing them with the expressions for spherical waves to show that the statement holds true for these three source orders, and then it is claimed that it holds for any arbitrary source order (Morse and Ingard, 1986). In other areas, the mathematical proof of the completeness of the multipole series representing a solution of the Laplace equation has been demonstrated (Morse and Feshbach, 1953), but the procedures used in that proof cannot be easily extended to the treatment of the multipole series solution for the Helmholtz equation, which is the subject here. Therefore the focus of the present work is to show that, for the Helmholtz equation, the Cartesian multipole series spans the same vector space as the spherical wave series in 3D and the cylindrical wave series in 2D. Note that only the solution for outgoing waves is considered here, since the incoming wave solutions can be treated in an identical way.

The key result in the present work, which leads directly to the completeness of the multipole series, is the following statement: let φ_n be an nth order spherical wave for 3D cases (or a cylindrical wave in 2D cases), and ψ_n be an nth order multipole; then each φ_n can be expressed as a linear combination of multipoles ψ_i with $i \leq n$. This means that the multipoles and the spherical waves (or cylindrical waves) span the same space and thus the completeness of spherical and cylindrical waves infers the completeness of the multipole series. The 2D and 3D cases are treated separately in proving this statement.

A.2.1 2D Multipoles

In 2D cases, a statement that is stronger than the one given above holds: each φ_n, which denotes cylindrical waves here, can be expressed as a linear combination of multipoles of the same order (i.e., ψ_i with $i = n$). The proof of this statement can be conducted by induction. It is first noted that the when $n = 0$, the cylindrical wave and the multipole are the same: i.e., both comprise a single outgoing field, which is expressed as

$$\psi_0 = \varphi_0 = H_0^{(1)}(kr), \tag{2}$$

when the time dependence is assumed to be $e^{-j\omega t}$, and where $H_0^{(1)}(\cdot)$ is the zeroth order Hankel function of the first kind. Thus the validity of the statement is confirmed for $n = 0$, and then when it is assumed that the statement holds for an arbitrary n, the same statement only needs to be deduced for $n + 1$. Since, from the definition of a multipole, each $n + 1^{\text{st}}$ order multipole, ψ_{n+1}, can be expressed as $\frac{\partial}{\partial x}\psi_n$ or $\frac{\partial}{\partial y}\psi_n$ for a corresponding nth order multipole, ψ_n, and since, based on the assumed validity of the statement that, for an arbitrary n, each cylindrical wave $\varphi_n$is a linear combination of the ψ_n's, the statement for $n + 1$ (i.e., each φ_{n+1} is a linear combination of the ψ_{n+1}'s) can be deduced once it is shown that each φ_{n+1} is a linear combination of the $\frac{\partial}{\partial x}\varphi_n$'s and $\frac{\partial}{\partial y}\varphi_n$'s: i.e., each $n + 1^{\text{st}}$ order cylindrical wave is a linear combination of the x and y derivatives of the nth order cylindrical waves.

At this point, the steps left to complete the proof for 2D cases are not complicated; however, in 3D cases the remaining process is more involved, and so that proof will be presented

separately in the next subsection. To complete the proof for 2D cases, it is first noted that the expression of the cylindrical wave of order n in polar coordinates is written as:

$$\varphi_n(r,\theta) = H_n^{(1)}(kr)e^{\pm jn\theta}, \tag{3}$$

where $H_n^{(1)}(\cdot)$ is the nth order Hankel function of the first kind. Note that only the waves with the term $e^{jn\theta}$ need to be considered in the proof, since for the case of $e^{-jn\theta}$, the treatment is identical if n is replaced by $-n$. To proceed with the proof, the above definition is then combined with the derivative relation of the Hankel function and the differentiation relation between polar and Cartesian coordinates: i.e.,

$$\frac{d}{dt}H_n^{(1)}(t) = \frac{nH_n^{(1)}(t)}{t} - H_{n+1}^{(1)}(t), \tag{4}$$

$$\frac{\partial}{\partial x} = \cos\theta\frac{\partial}{\partial r} - \frac{1}{r}\sin\theta\frac{\partial}{\partial\theta}, \qquad \frac{\partial}{\partial y} = \sin\theta\frac{\partial}{\partial r} + \frac{1}{r}\cos\theta\frac{\partial}{\partial\theta}, \tag{5}$$

where t in Eq. (4) is an arbitrary independent variable. It is then straightforward to derive the results:

$$\begin{cases} \dfrac{\partial}{\partial x}\ \varphi_n = (\cos\theta - j\sin\theta)\dfrac{nH_n^{(1)}(kr)}{r}e^{jn\theta} - kH_{n+1}^{(1)}(kr)\cos\theta e^{jn\theta} \\ \dfrac{\partial}{\partial y}\ \varphi_n = (\sin\theta + j\cos\theta)\dfrac{nH_n^{(1)}(kr)}{r}e^{jn\theta} - kH_{n+1}^{(1)}(kr)\sin\theta e^{jn\theta}. \end{cases} \tag{6}$$

From Eqs. (3) and (6), it can be shown that

$$\varphi_{n+1} = H_{n+1}^{(1)}(kr)e^{j(n+1)\theta} = -\frac{1}{k}(\frac{\partial}{\partial x}\varphi_n + j\frac{\partial}{\partial y}\varphi_n), \tag{7}$$

which proves the statement that each φ_{n+1} is a linear combination of $\frac{\partial}{\partial x}\varphi_n$ and $\frac{\partial}{\partial y}\varphi_n$. This last step finishes the induction process and thus completes the proof of the completeness of the 2D multipoles series.

A.2.2 3D Multipoles

As for the 2D cases, the focus here is on proving the statement that each spherical wave, φ_n, can be expressed as a linear combination of Cartesian multipoles ψ_i with $i \leq n$. It is noted first that in 3D cases the condition $i \leq n$ is required, whereas only $i = n$ is needed in 2D cases. According to the same induction logic as used in the 2D proof, after checking the validity for $n = 0$, it is then only necessary to show that each φ_{n+1} is a linear combination of the $\frac{\partial}{\partial x}\varphi_n$'s, $\frac{\partial}{\partial y}\varphi_n$'s, $\frac{\partial}{\partial z}\varphi_n$'s and φ_i's with $i \leq n$: this last statement differs slightly from the 2D cases because of the condition $i \leq n$ and the inclusion of the φ_i's.

It is easy to check the validity of the statement for $n = 0$, since the zeroth order multipole is the Green's function which is a constant times the zeroth order spherical Hankel's function: i.e., the zeroth order spherical wave. However, to prove the linear combination relation of φ_{n+1}, it is difficult to use direct differentiation and simple algebra to derive a relation similar to Eq. (7): instead a more delicate procedure is required.

There are $2n+1$ spherical wave functions for order n (still only considering the outgoing waves for the $e^{-j\omega t}$ time dependence), which can be expressed, in spherical coordinates, as:

$$\varphi_n = h_n^{(1)}(kr)Y_n^m(\theta,\phi) \tag{8}$$

where $h_n^{(1)}(\cdot)$ is the nth order spherical Hankel function of the first kind, and $Y_n^m(\cdot)$ is an nth order spherical harmonic with $-n \le m \le n$. To proceed with the proof in the present work, the following properties of spherical harmonics need to be used: (1) with x_1, x_2, x_3 being used to replace x, y, z for convenience, the function,

$$P_n^{(m)}(x_1,x_2,x_3) = r^n Y_n^m(\theta,\phi), \tag{9}$$

is a homogeneous harmonic polynomial of degree n (Colton and Kress, 2012), i.e., $P_n^{(m)} = \sum b_{i,j,k} x_1^i x_2^j x_3^k$ with $i+j+k=n$, and it satisfies the Laplace equation ($\nabla^2 P_n^{(m)} = 0$); (2) in addition, it can be shown that for each order n, there exist exactly $2n+1$ independent homogeneous harmonic polynomial (Colton and Kress, 2012). For the convenience of listing those independent functions, $P_n^{(m)}$ is expressed as:

$$P_n^{(m)}(x_1,x_2,x_3) = \sum_{k=0}^{n} a_{n-k}(x_1,x_2)x_3^k, \tag{10}$$

where $a_{n-k}(x_1,x_2)$ is a homogeneous polynomial of degree $n-k$. Since it is harmonic, $P_n^{(m)}$ is determined if a_n and a_{n-1} are determined with the relation, $a_{n-k} = \frac{\nabla^2 a_{n-k+2}}{k(k-1)}$, so

that the $2n+1$ independent $P_n^{(m)}$'s can be written, by specifying their a_n's and a_{n-1}'s, as (Colton and Kress, 2012):

$$\begin{aligned} a_n = x_1^{n-j}x_2^j \quad a_{n-1} = 0 \qquad & j = 0,1,...n \\ a_n = 0 \quad a_{n-1} = x_1^{n-1-j}x_2^j \qquad & j = 0,1,...n-1. \end{aligned} \tag{11}$$

From these two properties, it is seen that the Y_n^m's in Eq. (8) and the $\frac{P_n^{(m)}}{r^n}$'s with $P_n^{(m)}$ specified in Eq. (11) are two bases of the same space. Thus in proving the linear combination property of φ_n, it is equivalent, but more convenient, to define the spherical waves, φ_n, as:

$$\varphi_n = \frac{h_n^{(1)}(kr)}{r^n} P_n^{(m)}(x_1, x_2, x_3), \tag{12}$$

where, again, the $P_n^{(m)}$'s are specified in Eq. (11).

Recall that the goal here is to prove that each φ_{n+1} can be expressed as a linear combination of $\frac{\partial}{\partial x_i}\varphi_n$'s ($i = 1,2\ or\ 3$) and φ_j ($j \le n$). By following the definition in Eq. (12), and using the differentiation relation and the recursive relation of the spherical Hankel's functions, i.e.,

$$\frac{d}{dt}\left(\frac{h_n^{(1)}(t)}{t^n}\right) = -\frac{h_{n+1}^{(1)}(t)}{t^n}, \tag{13}$$

$$\frac{h_n^{(1)}(t)}{t} = \frac{1}{2n+1}\left[h_{n+1}^{(1)}(t) + h_{n-1}^{(1)}(t)\right], \tag{14}$$

the derivatives of φ_n can be expressed as:

$$\frac{\partial}{\partial x_i}\varphi_n = \frac{k}{2n+1}\frac{h_{n+1}^{(1)}(kr)}{r^{n+1}} q_{n+1}^{i}(x_1, x_2, x_3) + \frac{k}{2n+1}\frac{h_{n-1}^{(1)}(kr)}{r^{n-1}}\frac{\partial}{\partial x_i} P_n^{(m)}(x_1, x_2, x_3), \tag{15}$$

with

$$q_{n+1}^{i}(x_1, x_2, x_3) = -(2n+1)x_i P_n^{(m)}(x_1, x_2, x_3) + r^2 \frac{\partial}{\partial x_i} P_n^{(m)}(x_1, x_2, x_3). \tag{16}$$

To proceed further, it is, first, necessary to show that the first and the second terms on the right hand side of Eq. (15) belong to the space of the $n+1^{\text{st}}$ order spherical wave and $n-1^{\text{st}}$ order spherical wave, respectively, which means that, by differentiating a nth order spherical wave, spherical waves of order $n+1$ and $n-1$ are produced. To prove that statement, it needs to be shown that $\frac{\partial}{\partial x_i} P_n^{(m)}$ is a homogeneous harmonic polynomial of degree $n-1$ and that q_{n+1}^{i} is a homogeneous harmonic polynomial of degree $n+1$. It is straightforward to check that these two terms are homogeneous polynomials of the desired degrees, and it also not difficult to show that $\frac{\partial}{\partial x_i} P_n^{(m)}$ is harmonic: i.e., $\nabla^2\left(\frac{\partial}{\partial x_i} P_n^{(m)}\right) = 0$ (since $\nabla^2 P_n^{(m)} = 0$). It still remains to be shown that q_{n+1}^{i} is harmonic. That result can be obtained by direct calculation or by noticing that both $\frac{\partial}{\partial x_i}\varphi_n$ and $\frac{h_{n-1}^{(1)}(kr)}{r^{n-1}}\frac{\partial}{\partial x_i} P_n^{(m)}$ satisfy

the Helmholtz equation, so that $\frac{h_{n+1}^{(1)}(kr)}{r^{n+1}} q_{n+1}^{i}$ satisfies the Helmholtz equation, and, so therefore, q_{n+1}^{i} is harmonic.

To finish the proof that all φ_{n+1}'s can be constructed from linear combinations of $\frac{\partial}{\partial x_i}\varphi_n$'s ($i = 1,2\ or\ 3$) and φ_j's ($j \leq n$), it is further noted that the term $\frac{h_{n-1}^{(1)}(kr)}{r^{n-1}} \frac{\partial}{\partial x_i} P_n^{(m)}$, from the previous steps, belongs to the set $\{\varphi_j\ , j \leq n\}$, so the proof is completed if it can be shown that all φ_{n+1} 's can be written as a linear combination of the $\frac{h_{n+1}^{(1)}(kr)}{r^{n+1}} q_{n+1}^{i}$'s , which were already shown to be spherical waves of order $n+1$. The latter is equivalent to saying that each of the independent $P_{n+1}^{(m)}$'s (listed in Eq. (11), with n replaced by $n+1$), can be expressed as linear combinations of the q_{n+1}^{i}'s (defined in Eq. (16)) with the independent $P_n^{(m)}$'s listed in Eq. (11) and with $i = 1$, 2 and 3. This is a relatively simple step, since, if all independent $P_n^{(m)}$'s listed in Eq. (11) and $i = 1$, 2 and 3 are enumerated, the first term in the expression of q_{n+1}^{i} in Eq. (16), i.e., $x_i P_n^{(m)}$, already includes the a_{n+1}'s and a_n's in Eq. (11) after replacing n with $n+1$. The last step of the proof is to show that the second term in Eq. (16)), $r^2 \frac{\partial}{\partial x_i} P_n^{(m)}$, does not cancel the first term, $-(2n+1)x_i P_n^{(m)}$, for any of the a_{n+1}'s and a_n's. Such a no-cancellation property is ensured by the different constant coefficient in front of each term, as long as $n \neq 0$, which is the case since the validity of the case $n = 0$ was checked at the beginning of the proof. At this point, the proof of the completeness of the 3D multipoles series is finished.

In the case of incoming waves, the same conclusion holds, i.e., each incoming spherical wave (cylindrical wave for 2D) can be expressed as a finite linear combination of a number of incoming Cartesian multipoles, where the incoming multipoles are defined as the complex conjugate of the outgoing multipoles, and the incoming spherical (or cylindrical for 2D) waves are defined by replacing the spherical Hankel function of the first kind in Eq. (3) (or the Hankel function of the first kind in Eq. (8) for 2D) with their counterparts of the second kind. The proof of this statement for incoming waves can be achieved either by following the same process as in the outgoing wave case, or simply by taking the complex conjugate of the outgoing wave conclusion, i.e., the complex conjugate of Eq. (3) (or Eq. (8) for 2D) can be expressed as a finite linear combination of incoming multipoles, and then noticing that the complex conjugate of the outgoing spherical (or cylindrical) waves have a one-to-one correspondence to the incoming spherical (or cylindrical) waves. Therefore the completeness of the incoming Cartesian multipole series is also proven.

A.3 The Linear Dependence Among the Multipoles

After proving the completeness of the multipoles series, the linear dependence relations among different orders of multipoles can, with some effort, be clearly observed. A classic specific case of this linear dependence relation is that a longitudinal quadrupole contains a monopole component. Here, a more general conclusion can be drawn for multipoles of arbitrary orders. Only the 3D multipoles are discussed here, since the 2D multipole case is a simplification of the 3D case.

One obvious linear dependence relation for the multipoles follows from the fact that each multipole satisfies the Helmholtz equation, i.e.,

$$\frac{\partial^2}{\partial x^2}\psi_n + \frac{\partial^2}{\partial y^2}\psi_n + \frac{\partial^2}{\partial z^2}\psi_n + k^2\psi_n = 0, \tag{17}$$

in which, based on the definition of multipoles, each of the first three terms on the left hand side represents a multipole of order $n+2$, while the last term is a multipole of order n. For the special case of $n = 0$, it represents the well-known monopole-quadrupole coupling: since the first three terms in Eq.(17), with $n = 0$, represent the three longitudinal quadrupoles and the last term represents a monopole, it is then clear that a monopole sound field can be expressed as the sum of the three longitudinal quadrupoles multiplied by $-1/k^2$. Thus, in general, this equation can be interpreted as meaning that any multipole of order n can be expressed as a linear combination of three multipoles of order $n+2$. This observation also suggests that in the space spanned by the multipoles up to order M, span$\{\psi_n, n \le M\}$, all ψ_n's with $n \le M-2$ are linearly dependent on the ψ_{M-1}'s and ψ_M's. A more interesting conclusion that can be drawn, based on the proof in the previous section, is that the ψ_{M-1}'s and ψ_M's are linearly independent, which then means that if a basis is to be extracted from a multipole series, one only needs to include the multipoles in the highest two orders: that is all the other lower order sources can be eliminated.

To prove that the ψ_{M-1}'s and ψ_M's are linearly independent, one only needs to show that the total number of multipoles included in orders M and $M-1$ is the same as the total number of spherical waves included in orders from 0 to M, since, from the proof in the

previous section, it is known that the space spanned by the multipoles up to order M is the same as the space spanned by the spherical waves up to the same source order and that all of the spherical waves, defined in Eq. (8), are known to be linearly independent (in fact, orthogonal). This can be checked easily with the help of Eq. (1) and the knowledge of the fact that there are $2n+1$ independent spherical waves for order n: i.e., one can find: $N(M,3)+N(M-1,3)=\sum_{n=0}^{M}2n+1$. Therefore it is concluded that in the sequence of multipoles, the multipoles in the two highest orders form a basis of the space spanned by all the elements in the sequence, and the lower order multipoles can be obtained by linear combination of multipoles in the two highest orders through the Helmholtz equation.

VITA

VITA

Yangfan Liu

Education

PhD, Mechanical Engineering, **Purdue University,** West Lafayette, Indiana. Aug. 2016
Master, Mechanical Engineering, **Purdue University,** West Lafayette, Indiana. Dec 2011
Bachelor, Mechanical Engineering, **East China University of Science and Technology**, China. Jun 2009

Research Experience

PhD thesis: Efficient Modeling of Sound Source Radiation in Free-space and Room Environments
Jan. 2012 – Aug. 2016

- Developed a non-collocated Multipole equivalent sources model for efficient free-space sound field simulations which is validated with Boundary Element Model simulations and results from sound pressure and laser vibrometer measurements. The developed model requires fewer model parameters and has a much wider frequency range than traditional acoustical holography methods.
- Modified and extended the use of Equivalent Source Models to the room acoustics in both 2D and 3D applications, which significantly reduces the computational load, compared with Boundary Element Methods, and can be applied to more complex sources than Ray Tracing models.
- Proposed local basis methods for sound field simulations at very high frequencies which further extended the feasible frequency range of the simulation when combined with the equivalent source models developed earlier.

Project on spatial localization of combustion and mechanical noise sources in a diesel engine, Apr. 2015 – Aug. 2016 (sponsored by Cummins)

- Developed different types of acoustical holography methods to reconstruct the near field sound field of a diesel engine based on far field array measurements, and investigated the performances of these methods in a diesel engine application.
- Applied the partial field decomposition technique to extract the contribution of each individual spatially separated noise source.

Project on the modeling of a new electrostatically-actuated loudspeaker design, Jun. – Sep. 2014 (sponsored by Google)

- Collaborated with a dynamics and a control groups at Purdue to construct an integrated simulation model for a new loudspeaker design which generates sound by an S-shaped, electrostatically driven membrane oscillating in a thin channel.
- Built simulation tools for acoustical wave propagations in a thin channel considering the fluid viscosity and heat conduction effects based on Kirchhoff's theory and for sound radiation from small openings.

Master thesis: Sound Field Reconstruction and its Application in Loudspeaker Sound Radiation Prediction
Sep. 2009 – Dec. 2011 (sponsored by Sony)

- Proposed a simulation technique for loudspeaker sound field at the anechoic environment with a new Multipole source representation (more efficient and more convenient for further processing).
- Extended the Image Source Model from point source input to Multipole sources in room acoustics.

Teaching and Presenting Experience

Lecturer of ME 270 (Basic Mechanics I) at Purdue University
Lecturer of an undergraduate level class of Basic Mechanics (Fall semester in 2015) under a graduate teaching fellowship. Responsibilities are the same as a full-time lecturer, including teaching lectures for a full semester, providing office hours for students and preparing homework, quiz and exam problems for the class.

Teaching Assistant for ME 513 (Engineering Acoustics) and ME 579 (Signal Processing) at Purdue
TA for graduate level classes of Engineering Acoustics (Fall semesters in 2010, 2012 and 2013) and Signal Processing (Spring semester in 2015 and 2016). Duties include homework grading, answering students' questions, organizing the course website and giving lectures when the professor is out of town.

Tutor for undergraduate student athletes on MA 161 (Calculus I) and PHYS 202 (General Physics II)
Tutor of undergraduate student athletes (Fall 2009) on freshmen calculus and physics. Meet each student twice a week explaining the concepts covered in class, helping with the homework and exams preparations.

Conference presentations: Inter-Noise (Aug. 2012, New York); Noise-Con (Aug. 2013, Denver), Noise-Con (Sep. 2014, Fort Lauderdale), Inter-Noise (Aug. 2015, San Francisco).

Publications

- Liu, Y., & Bolton J. S. (2016). On the completeness and the linear dependence of the Cartesian multipole series in representing the solution to the Helmholtz equation. The Journal of the

Acoustical Society of America, 140(2).

- Liu, Y., & Bolton, J. S. (2016, August). Experimental investigation of the use of equivalent sources model in room acoustics simulations. In *INTER-NOISE and NOISE-CON Congress and Conference Proceedings*. Institute of Noise Control Engineering.
- Liu, J., Liu, Y., & Bolton, J. S. (2016, June). Noise source identification based on an inverse radiation mode procedure. In *INTER-NOISE and NOISE-CON Congress and Conference Proceedings*. Institute of Noise Control Engineering.
- Shi, T., Liu, Y., & Bolton, J. S. (2016, June). The use of wideband acoustical holography for noise source visualization. In *INTER-NOISE and NOISE-CON Congress and Conference Proceedings*. Institute of Noise Control Engineering.
- Liu, Y., & Bolton, J. S. (2015, August).Simulation of sound fields radiated by finite-size sources in room environments by using equivalent source models: three-dimensional validation. In *INTER-NOISE and NOISE-CON Congress and Conference Proceedings*. (Vol. 250, No. 3, pp. 4246-4259). Institute of Noise Control Engineering.
- Liu Y., & Bolton J.S, (2014, September) High frequency sound field simulation for multiple sources using local basis representations In *INTER-NOISE and NOISE-CON Congress and Conference Proceedings* (Vol. 248, No. 1, pp. 586-594). Institute of Noise Control Engineering.
- Liu, Y., & Bolton, J. S. (2013, August). Sound field reconstruction at high frequencies by using a piece-wise interpolation method. In *INTER-NOISE and NOISE-CON Congress and Conference Proceedings* (Vol. 246, No. 1, pp. 662-671). Institute of Noise Control Engineering.
- Liu, Y., & Bolton, J. S. (2013, June). The use of equivalent source models for reduced order simulation in room acoustics. In *Proceedings of Meetings on Acoustics* (Vol. 19, No. 1, p. 015130). Acoustical Society of America.
- Liu, Y., & Bolton, J. S. (2012, August). The use of non-collocated higher order sources in the equivalent source method. In *INTER-NOISE and NOISE-CON Congress and Conference Proceedings* (Vol. 2012, No. 4, pp. 7326-7337). Institute of Noise Control Engineering.

Awards

- Teaching Academy Graduate Teaching Award, 2016, Purdue University. (1 or 2 recipients per year for each school).
- Ward A. Lambert Graduate Teaching Fellowship, 2015, School of Mechanical Engineering, Purdue University.
- Classic Papers in Noise Control Engineering Presentation Competition in Inter-Noise Conference 2015.
- Michiko So Finegold Award, 2015, Institute of Noise Control Engineering of the USA, student activities.
- Student Paper Prize Competition in Noise-Con 2014.
- Hallberg Fundation Award, 2014, Institute of Noise Control Engineering of the USA, student activities.